# Nano-Micro Letters

REVIEW

Check for updates

Boosting Lean Electrolyte Lithium–Sulfur Battery Performance with Transition Metals: A Comprehensive Review

Hui Pan[1], Zhibin Cheng[2] ✉, Zhenyu Zhou[3], Sijie Xie[3], Wei Zhang[3], Ning Han[3], Wei Guo[3], Jan Fransaer[3] ✉, Jiangshui Luo[4] ✉, Andreu Cabot[5] ✉, Michael Wübbenhorst[1] ✉

HIGHLIGHTS

- This review systematically analyzes the effect of the electrolyte-to-sulfur ratios on battery energy density and the challenges for sulfur reduction reactions under lean electrolyte conditions.

- The strengths and limitations of different transition metal compounds are systematically presented and discussed from a fundamental perspective.

- Three promising strategies for sulfur hosts that act as anchors and catalysts are proposed to boost lean electrolyte Li–S battery performance.

ABSTRACT Lithium–sulfur (Li–S) batteries have received widespread attention, and lean electrolyte Li–S batteries have attracted additional interest because of their higher energy densities. This review systematically analyzes the effect of the electrolyte-to-sulfur (E/S) ratios on battery energy density and the challenges for sulfur reduction reactions (SRR) under lean electrolyte conditions. Accordingly, we review the use of various polar transition metal sulfur hosts as corresponding solutions to facilitate SRR kinetics at low E/S ratios (< 10 μL mg^{-1}), and the strengths and limitations of different transition metal compounds are presented and discussed from a fundamental perspective. Subsequently, three promising strategies for sulfur hosts that act as anchors and catalysts are proposed to boost lean electrolyte Li–S battery performance. Finally, an outlook is provided to guide future research on high energy density Li–S batteries.
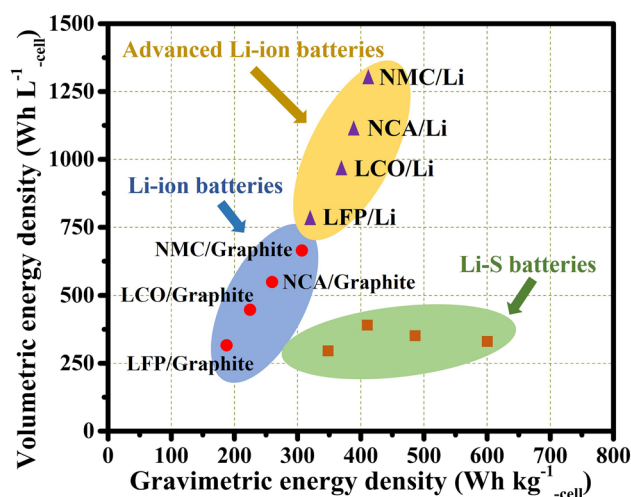
KEYWORDS Transition metals; Lean electrolyte; Sulfur reduction reactions; Li–S batteries

✉ Zhibin Cheng, chengzhibin@fjnu.edu.cn; Jan Fransaer, jan.fransaer@kuleuven.be; Jiangshui Luo, jiangshui.luo@scu.edu.cn; Andreu Cabot, acabot@irec.cat; Michael Wübbenhorst, michael.wubbenhorst@kuleuven.be

1   Laboratory for Soft Matter and Biophysics, Faculty of Science, KU Leuven, 3001 Leuven, Belgium
2   Fujian Key Laboratory of Polymer Materials, College of Chemistry and Materials Science, Fujian Normal University, Fuzhou 350007, People's Republic of China
3   Department of Materials Engineering, Faculty of Science Engineering, KU Leuven, 3001 Leuven, Belgium
4   Lab of Electrolytes and Phase Change Materials, College of Materials Science and Engineering, Sichuan University, Chengdu 610065, People's Republic of China
5   Advanced Materials Department, Catalonia Institute for Energy Research (IREC), Sant Adria del Besos, 08930 Barcelona, Spain

SHANGHAI JIAO TONG UNIVERSITY PRESS

⚡ Springer

1 Introduction

The lithium-sulfur (Li–S) battery is based on a conversion-type cathode where the electrochemical redox reaction between active sulfur (S_8) and lithium sulfide ($S_8 + 16Li^+ + 16e^- \rightleftharpoons 8Li_2S$) takes place [1–3]. While sulfur is very abundant and inexpensive, sulfur cathodes provide much higher theoretical specific capacities (1675 mAh g^{-1}) than those of intercalation-type lithium-ion (Li-ion) batteries (e.g., LiFePO$_4$-170 mAh g^{-1}; LiCoO$_2$-274 mAh g^{-1}; LiMn$_2$O$_4$-148 mAh g^{-1}) [4–7]. Thus, Li–S batteries are particularly appealing next-generation rechargeable energy storage devices owing to their potential for low cost and high theoretical energy density (2600 Wh kg^{-1}) [4, 8–10].

Li–S batteries emerged in 1962 when Herbert and Ulam first proposed the concept of employing sulfur as a cathode [11–15]. Looking back over the past 60 years, the development process of Li–S batteries can be divided into three stages (Fig. 1). The first phase focused on how to make rechargeable Li–S batteries (1962–2008). During this development process, conventional organic electrolytes (e.g., propylene carbonate, ethylene carbonate, dimethyl carbonate, dimethyl sulfoxide) [16–18], dioxolane-based organic electrolytes (e.g., 1.3-dioxolane) [19] and polymer electrolytes (e.g., polyethylene oxide) [20, 21] were studied. In 2002, Wang et al. first proposed a sulfur/conductive polymer (sulfur@polyaniline) composite as cathode material for rechargeable batteries with high performance [22]. In 2008, Mikhaylik found that lithium nitrate (LiNO$_3$) was an effective electrolyte additive to inhibit the shuttle effect and boost the Coulombic efficiency of Li–S cells [23]. However, at the end of this first phase, the reversibility of the Li–S batteries was still very low. The second phase primarily focused on improving the performance of Li–S coin cells (2009–2013). In 2009, Nazar's group achieved more than 20 stable cycles of Li–S cells by using polymer-modified mesoporous carbon (CMK-3) as a sulfur host [24], which sparked a renaissance of the Li–S battery. Following that, various porous carbon and polar materials were developed to mitigate the dissolution of lithium polysulfides (LiPS) through physical confinement or chemical adsorption [1, 25]. In 2013, Xiao et al. explored the effect of the electrolyte/sulfur (E/S) ratio on Li–S batteries [26] evidencing the great challenge that is moving toward high-density lean electrolyte Li–S batteries [27, 28]. In this second phase, multiple strategies such

as advanced sulfur hosts [24, 29], anode protection [30, 31] and electrolyte optimization [32, 33], were employed to develop Li–S coin cells reaching lifespans over 1000 cycles [34]. However, to demonstrate practical energy densities above 400 Wh kg^{-1}, Li–S pouch cells with practical parameters had to be developed. The third phase (2014–now) focuses on improving the performance of Li–S pouch cells under practical operating conditions (high sulfur loading, low E/S ratio, low negative/positive ratio) and developing high energy density Li–S batteries. In 2014, Hagen and colleagues published the first study on Li–S pouch cells, where they examined ideal E/S ratios to realize high energy density pouch cells [27]. Since then, advanced Li–S pouch cells have been studied extensively and significant progress has been made [35, 36]. Cui's group first proposed the concept of catalysis for Li–S batteries in 2017 [37]. They found that metal sulfides as activation catalysts could catalyze the oxidation of Li$_2$S to S. Electrocatalysts have the potential to address the issues of severe LiPS shuttle effect and sluggish sulfur redox kinetics in Li–S batteries. Consequently, electrocatalyst design has attracted a great deal of attention [11–13, 38–49]. After 60 years of continuous development, now, looking ahead to the future, considerable efforts are still required to bring Li–S batteries to the market, such as sulfur loading > 8 mg cm^{-2}, electrolyte to sulfur ratio < 3 µL mg^{-1}, negative to positive ratio < 4, carbon content < 5 wt%, lifespans > 500 cycles.

Li–S battery system is regarded as one of the most promising candidates for next-generation rechargeable batteries because of its low cost ($\approx$ 0.1 \$ kg^{-1} for sulfur), high theoretical specific capacity (1675 mAh g^{-1}) and high theoretical energy density ($\approx$ 2600 Wh kg^{-1}) [52–54]. The mechanism of Li–S batteries is based on chemical transformations rather than intercalation chemistry in Li-ion batteries [55, 56]. For Li–S batteries, the widely accepted reaction mechanism is that during the discharging process, sulfur exists as polysulfides or sulfide of the general formula, Li$_2$S$_x$, where $x = 8$, 6, 4, 2 or 1 (Fig. 2) [57]. In the very first discharge process, solid S_8 dissolves in the electrolyte to form a liquid state ($S_8(s) \rightarrow S_8(l), > 2.3$ V). Then, the bonds of liquid S_8 molecules are broken to combine with Li$^+$ to produce long-chain polysulfides as the reaction proceeds ($S_8(l) + 2Li^+ + 2e^- \rightarrow Li_2S_8(l), > 2.3$ V). The reaction from $S_8(l)$ to Li$_2$S$_8$(l) is spontaneous reaction. Subsequently, in the voltage range of 2.3 to 2.1 V, the highest order polysulfide
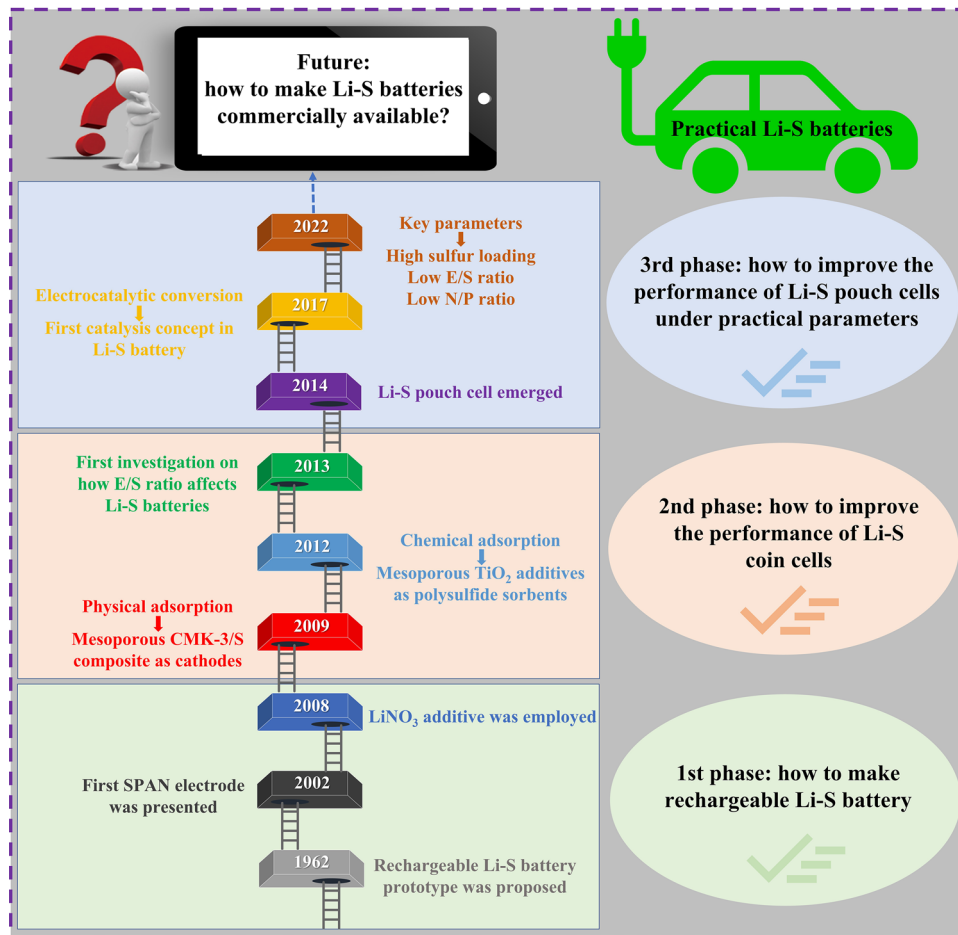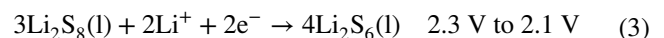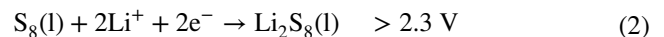
Fig. 1 A brief timeline and representative events in the development of Li–S batteries. The development process can be divided into four stages, mainly covering (i) 1962–2008: how to make Li–S battery cycle; (ii) 2009–2013: how to improve the performance of Li–S coin cells; and (iii) 2014-present: how to improve the performance of Li–S pouch cells under practical parameters; (iv) future: how to make Li–S batteries commercially available. Inserted represented works: 1962 [50], 2002 [22]. Copyright 2002, Wiley-VCH. 2008 [23], 2009 [24]. Copyright 2009, Springer Nature. 2012 [51]. Copyright 2012, American Chemical Society. 2013 [26], 2014 [27]. Copyright 2014, Elsevier. 2017 [37]. Copyright 2017, National Academy of Sciences. 2022 [48]. Copyright 2022, Wiley-VCH

$Li_2S_8(l)$ is reduced to a lower-order polysulfide $Li_2S_6(l)$ $(3Li_2S_8(l) + 2Li^+ + 2e^- \rightarrow 4Li_2S_6(l))$; then, the polysulfide $Li_2S_6(l)$ is reduced further to soluble products $Li_2S_4(l)$ $(2Li_2S_6(l) + 2Li^+ + 2e^- \rightarrow 3Li_2S_4(l))$. The conversion from Li_2S_8 to Li_2S_6/Li_2S_4 is nearly thermodynamical equilibrium. Above is the first discharge voltage plateau corresponding to the conversion of S_8 to soluble long-chain polysulfides, which provides the theoretical capacity of 419 mAh g^{-1} (25% of the overall specific capacity).
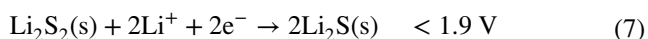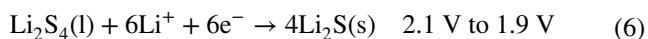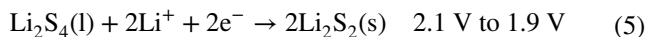
The electrochemical reactions in this phase are shown in Eqs. (1–4):

$$S_8(s) \rightarrow S_8(l) \quad > 2.3 \text{ V} \tag{1}$$

$$S_8(l) + 2Li^+ + 2e^- \rightarrow Li_2S_8(l) \quad > 2.3 \text{ V} \tag{2}$$

$$3Li_2S_8(l) + 2Li^+ + 2e^- \rightarrow 4Li_2S_6(l) \quad 2.3 \text{ to } 2.1 \text{ V} \tag{3}$$

$$2Li_2S_6(l) + 2Li^+ + 2e^- \rightarrow 3Li_2S_4(l) \quad 2.3 \text{ to } 2.1 \text{ V} \tag{4}$$

In the voltage range of 1.9 to 2.1 V, the further reduction of the long-chain soluble polysulfides to short chain insoluble products, $Li_2S_4(l) + 2Li^+ + 2e^- \rightarrow 2Li_2S_2(s)$, $Li_2S_4(l) + 6Li^+ + 6e^- \rightarrow 4Li_2S(s)$. At voltages more negative to 1.9 V, insoluble lithium polysulfide $Li_2S_2(s)$ is converted increasingly to insoluble lithium sulfide $Li_2S(s)$, $Li_2S_2(s) + 2Li^+ + 2e^- \rightarrow 2Li_2S(s)$. The reduction reaction

of Li_2S_2(s) to Li_2S(s) is the rate-limiting step, and the slow kinetics of the reaction is attributed to the low conductivity of Li_2S_2/Li_2S. Above is the second plateau, contributing a theoretical capacity of 1256 mAh g^{-1} at 2.1–1.7 V (75% of the overall specific capacity).

The electrochemical reactions in this phase are shown in Eqs. (5–7):

$$Li_2S_4(l) + 2Li^+ + 2e^- \rightarrow 2Li_2S_2(s) \quad 2.1\ V\ to\ 1.9\ V \quad (5)$$

$$Li_2S_4(l) + 6Li^+ + 6e^- \rightarrow 4Li_2S(s) \quad 2.1\ V\ to\ 1.9\ V \quad (6)$$

$$Li_2S_2(s) + 2Li^+ + 2e^- \rightarrow 2Li_2S(s) \quad < 1.9\ V \quad (7)$$

Li-ion batteries are the dominant energy storage technology to power portable electronics and electric vehicles. Therefore, it is essential to compare the energy density, cost, etc., of commercial Li-ion batteries with those of Li–S batteries, which are still under development. The cost of energy storage in batteries varies depending on various factors such as the size of the battery, the manufacturing process and the specific application [58, 59]. Generally speaking, the energy storage cost of Li–S batteries is higher than that of Li-ion batteries. One of the reasons Li–S batteries are more expensive than Li-ion batteries is the use of sulfur as the cathode material. Although sulfur is abundant and cheap, it has low electrical conductivity and is not very stable. To overcome these challenges, Li–S batteries require more complex cell designs and electrolyte compositions, which can increase the manufacturing cost. According to a report by the International Renewable Energy Agency (IRENA) in 2020, the current estimated cost of energy storage for Li–S batteries is around \$250–\$400 per kilowatt-hour (kWh). In comparison, the cost of energy storage for Li-ion batteries ranges from \$80 to \$250 per kWh (Left of Fig. 3). However, it is important to note that the cost of Li–S batteries is expected to decline over time as technology continues to improve and production processes become more efficient.

Self-discharge is the loss of battery capacity over time when the battery is not in use. This is due to the internal chemistry of the battery, which slowly discharges even when no load is connected. Li-ion batteries have a relatively low self-discharge rate, typically losing only 1%–5% of their capacity per month when stored at room temperature [5]. This makes Li-ion batteries a good choice for applications that require long-term storage, such as backup power systems and portable electronic devices. In contrast, Li–S batteries have a higher self-discharge rate because of the loss of capacity and self-discharge when sulfur dissolves and LiPS shuttles between cathode, which is mainly concentration-driven. As a result, Li–S batteries can lose up to 20% of their capacity per day when stored at room temperature (right of Fig. 3). This makes Li–S batteries less suitable for applications that require long-term storage, but they can still be used in applications that require frequent charging and discharging cycles, such as electric vehicles and grid-scale energy storage. The self-discharge rate is highly dependent on the depth of discharge and E/S ratio. As the E/S ratio decreases, making LiPS concentration gradient higher, which inevitably results in more severe shuttle and greater self-discharge [60]. Many researchers have proposed employing catalytic host materials to suppress the shuttle effect and thus reduce the self-discharge rate of Li–S batteries [39, 61–63]. However, the investigation of self-discharge behavior at various E/S ratios in Li–S batteries has received less attention compared to the extensive research conducted on the dynamic cycling efficiency and stability of these batteries.
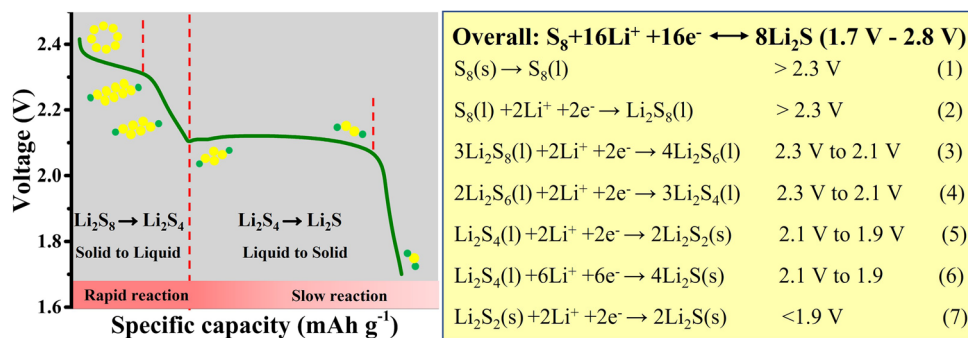

Fig. 2 Schematic of the electrochemistry for Li–S batteries

Comparison of the energy densities of Li-ion and Li–S batteries is represented by the Lagoon diagram (Fig. 4). Current commercial Li-ion batteries provide a driving range of 300 to 600 km with cell-level gravimetric energy densities of 150–265 Wh kg^{-1} for electric vehicles (e.g., Li-ion batteries used in Tesla electric cars have an energy density of about 265 Wh kg^{-1}), which is insufficient to realize a drive distance of 500-mile per charge at a reasonable battery pack size to alleviate mileage anxiety [64]. Recent literature has reported that Li-ion batteries with nickel-rich layered oxide cathodes and graphite anodes have energy densities over 300 Wh kg^{-1} [4]. High nickel lithium-ion batteries offer advantages in power output and energy density, but their high cost and limited availability of raw materials may hinder their widespread use in electric vehicles. Due to the multi-electron sulfur redox reaction, Li–S cells can provide a high theoretical energy density of 2600 Wh kg^{-1} and a full cell-level energy density of ≥ 600 Wh kg^{-1}. The primary advantage of Li–S batteries over Li-ion is their gravimetric energy density values of 720 Wh kg^{-1} (in the more ideal case) and ~ 400 Wh kg^{-1} (in most reported) [65, 66]. While cycle stability still struggles at 100 cycles, the gravimetric energy density of Li–S pouch cells has greatly improved to support applications where weight is more crucial than lifespan. For example, the Li–S cell manufacturers such as Sion Power and Oxis Energy announced a new target of 500 Wh kg^{-1} soon after achieving 400 Wh kg^{-1}for electric bus, truck and boat applications [64, 67]. Thanks to these fantastic benefits,

Li–S battery has the potential to compete with commercial Li-ion batteries in certain applications where high gravimetric energy density is a primary consideration.

Volumetric energy density is another key for practical applications. Higher volumetric energy density means that more energy can be stored in a smaller space, which is particularly important in applications where space is limited [53]. Therefore, it is quite urgent and worthwhile to assess the latest research on Li-ion and Li–S batteries to gain a greater understanding of the volumetric energy density of Li–S batteries [69]. As we can see from Fig. 4, despite their attractive high gravimetric energy density, Li–S batteries are dwarfed by the volumetric energy density of Li-ion batteries. Commercial Li-ion batteries can provide volumetric energy density of 250–750 Wh L^{-1} with graphite anodes, and the values can even surpass 1000 Wh L^{-1} when paired with Li anodes. For Li–S batteries, it is possible to achieve volumetric energy density values up to 1017 Wh L^{-1} under relatively ideal conditions [65]. However, the volumetric
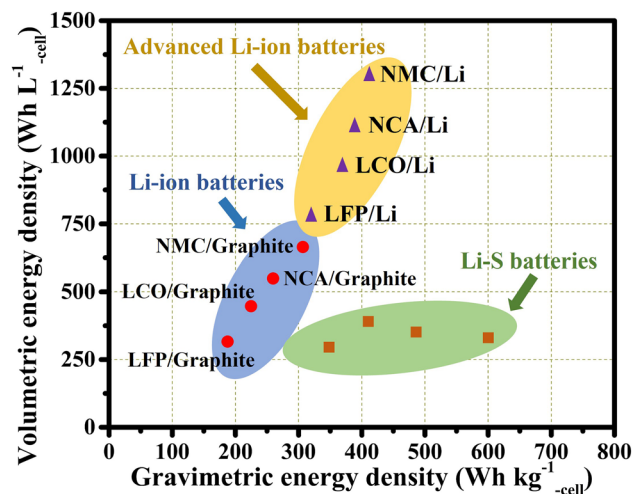
Fig. 4 Comparison of gravimetric energy density and volumetric energy density of Li–S batteries, Li-ion batteries and advanced Li-ion batteries. Advanced lithium-ion batteries are those that pair high-capacity lithium transition metal oxide cathodes with silicon and lithium metal, rather than just with graphite anode materials. The data (circles) of LiFePO$_4$ (LFP), LiCoO$_2$ (LCO), LiNi$_{0.8}$Co$_{0.15}$Al$_{0.05}$O$_2$ (NCA) and LiNi$_x$Co$_y$Mn$_{1-x-y}$O$_2$ (NCM) are from commercial Li-ion batteries of CATL, Panasonic, LG and BYD companies, respectively [53]. [4, 68][58] Copyright 2021, Wiley-VCH. The data (triangles) of advanced Li-ion batteries are obtained from Sion Power, with nickel-rich metal oxide as cathode material [67]. For Li–S battery, the data (squares) are collected from Sion Power [67], Oxis Energy, Kaskel's report [4, 68]. Copyright 2022, Springer Nature. Driving distance was calculated based on the energy density of each battery type, using the calculation method listed in Ref. [58]. Copyright 2022, Elsevier
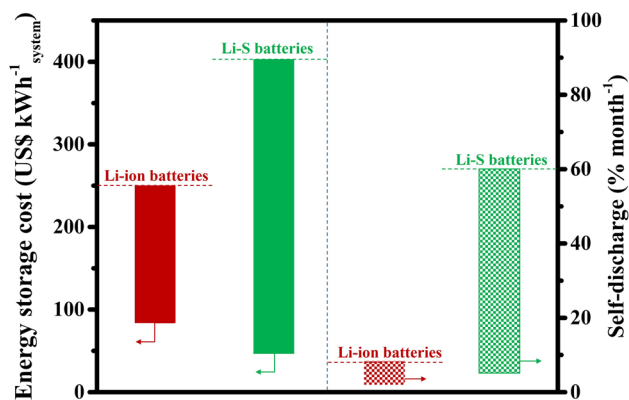

Fig. 3 Left: energy storage cost of Li-ion and Li–S batteries [5]. Copyright 2018, Springer Nature. Energy storage cost refers to the cost of the battery pack or system. Right: the upper and lower self-discharge ranges observed in commercial Li-ion and prototype Li–S batteries. Energy storage costs are calculated based on the calculation method listed in Ref. [58]. Copyright 2022, Elsevier

Table 1 Comparison of key parameters in different batteries

Battery type	Gravimetric energy density (Wh kg^{-1})	Volumetric energy density (Wh L^{-1})	Driving distance (km)	Cost range ($ kW h^{-1})
Li-ion	190–300	250–860	300–600	70–250
Advanced Li-ion	290–450	750–1300	450–940	≈ 130
Li–S	340–609	250–480	653–1136	36–400

energy density of most reported Li–S cells remains within the range of 200–400 Wh L^{-1}, which is lower than that of many commercially available Li-ion batteries. The volumetric energy density of Li–S batteries is far below than ideal due to the utilization of cathodes composed of abundant carbon materials. These carbon materials possess high specific surface areas and large pore volumes, leading to a decrease in the tap density of sulfur-based composites. Consequently, the reduced tap density limits the overall volumetric energy density in Li–S batteries. The higher tap density of metal-based compounds compared to lightweight carbon materials makes them advantageous for achieving a higher volumetric energy density in sulfur cathodes [70]. However, despite this potential, the current state of lithium-sulfur batteries still suffers from a poor volumetric energy density. As a result, their volumetric energy density was often excluded in early studies to highlight their superior gravimetric energy density. Therefore, future research works need to trade-offs to balance the gravimetric energy density and volumetric energy density of Li–S batteries. Table 1 summarizes the gravimetric energy density, volumetric energy density, corresponding driving distance and cost for Li-ion, advanced Li-ion and Li–S rechargeable battery systems.

The practical utilization of sulfur cathodes in Li–S batteries faces several significant challenges that impact the energy density and cycling stability of the batteries. These challenges include: (1) the electrically insulating character of sulfur and its solid discharge products (Li$_2$S$_2$/Li$_2$S): the low electrical conductivity of sulfur and its discharge products hinders the efficient utilization of sulfur and induces a high redox overpotential; (2) the severe volume change (≈ 79%) during cycling associated with the different densities of S and Li$_2$S, leading to mechanical stress and strain on the cathode materials, which can adversely affect their structural integrity and cycling stability; (3) the "shuttle effect" of the soluble lithium polysulfides intermediates, leading to active material loss, decreased Coulombic efficiency and reduced cycling stability of the battery (Fig. 5). In addition to the

challenges associated with the sulfur cathode, the use of Li metal anodes introduces safety concerns related to the growth of lithium dendrites. These dendrites can penetrate the separator and induce short circuits, posing safety risks and compromising the long-term performance and cycle life of the Li–S battery.

While various approaches have been used to tackle these issues, demonstrating reversibility with high sulfur loadings (> 15 mg cm^{-2}) [71, 72], high sulfur utilization (> 90%) [73–75] and long cycle lifespan (> 2000 cycles) [76, 77], most of these results have been obtained with an excess electrolyte, i.e., E/S ratios exceeding 10 μL mg^{-1}. With an E/S ratio of > 10 μL mg^{-1}, the energy density of Li–S batteries is compromised, causing them to lose their competitive edge compared to Li-ion batteries [78]. In these conditions, the electrolyte constitutes the largest weight fraction of a Li–S cell (Fig. 6a); electrolyte makes up more than 70 wt% of the overall cell. Such an excess of electrolyte inevitably results in a very low practical gravimetric energy density and a large cost increase, dispatching the two main advantages of Li–S batteries [10, 78–86]. Since high gravimetric energy density can only be achieved at a low E/S ratio, it is essential to minimize the volume of electrolyte for high gravimetric energy density Li–S batteries. As shown in Fig. 6b, the actual energy density of a Li–S cell with an E/S ratio of 10 μL mg^{-1} is below 150 Wh kg^{-1}, regardless of the areal sulfur loading. This value is far below what is needed for practical implementations. In conclusion, achieving high energy density in practical Li–S batteries requires a combination of a cathode with a relatively high sulfur loading and a low-volume electrolyte. According to our calculation, a sulfur loading above 5.0 mg cm^{-2} and an E/S ratio below 3.0 μL mg^{-1} are key indicators for Li–S systems to deliver an energy density higher than 300 Wh kg^{-1}.

The use of lean electrolyte conditions causes several major problems in Li–S batteries: (1) sluggish kinetics of the sulfur reduction reactions. As demonstrated in Fig. 7a, excessive electrolyte is necessary to ensure the utilization
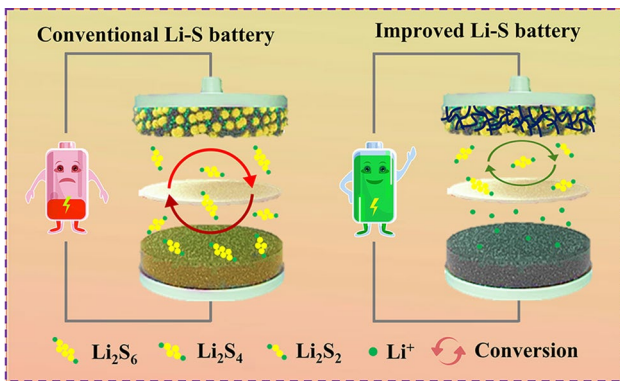
Fig. 5 Schematic of the working principles of Li–S batteries and "shuttle effect" of LiPS

of sulfur by sufficiently dissolving LiPS. Lean electrolyte conditions result in an inadequate dissolution of LiPS, which reduces kinetics of sulfur reduction reactions and hinders the utilization of sulfur. In addition, due to the insulating nature of sulfur and its discharge products, the sulfur reaction occurs only on the surface of the conductive materials. Therefore, the deposition of undissolved LiPS on the surface of conductive materials can significantly impede the subsequent sulfur reaction. (2) Incomplete wetting of the cathode surface. The electrochemistry of the Li–S cell relies on the redox of soluble LiPS, which in turn depends on rapid ion transport. Ion diffusion is favored when the liquid electrolyte wets the host materials. If the cathode surface is not completely wetted by the electrolyte, the transport of Li ions at the liquid–solid interface is hindered, which severely limits the sulfur redox reaction. As a result, the overall efficiency and performance

of the battery are compromised. (Fig. 7b). (3) High LiPS concentration and electrolyte degradation. Lean electrolyte results in an increase in the concentration of LiPS, thereby deteriorating the physical and chemical properties of the electrolyte (Fig. 7c). As the E/S ratio decreases, the ionic conductivity of the electrolyte decreases, and its viscosity increases due to the high LiPS concentration. In addition, the dissolved LiPS interacts with free solvent by solvation and forms clusters with the lithium salt further reducing the ionic conductivity of the electrolyte. The decrease in ionic conductivity leads to increased polarization and poor rate performance.

In response to the above issues, the rational design of lean electrolyte Li–S batteries focuses on: (1) building composite-based cathodes incorporating a conductive, high surface area and highly porous carbon framework. The carbon framework provides efficient pathways for electron transfer, while the high surface area and porosity promote the diffusion of Li ions and mitigate volume expansion, thus improving the sluggish kinetics of the sulfur redox reactions; (2) bringing in LiPS electrocatalysts. The addition of LiPS electrocatalysts aims to reduce the activation energy required for the sulfur redox reactions to promote the conversion of LiPS and facilitate their electrochemical reactions, leading to high sulfur utilization and accelerated redox reactions. (3) Developing host materials with hydrophilic surfaces. Hydrophilic surfaces have a strong affinity for electrolytes, improving surface wettability and electrolyte penetration into the cathode structure. This enhanced electrolyte penetration enhances the contact between sulfur species and Li ions, promoting the conversion of LiPS and improving the overall reaction
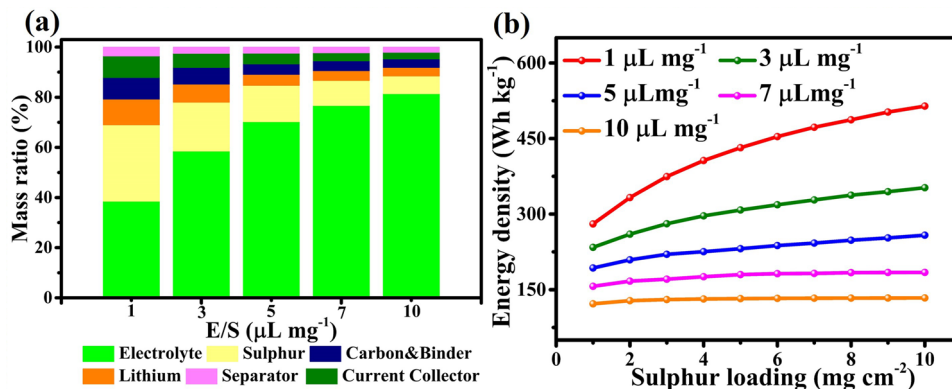

Fig. 6 **a** Weight distribution of different components at varied E/S ratios. **b** Energy density of Li–S batteries as a function of varying sulfur loading for different E/S ratios
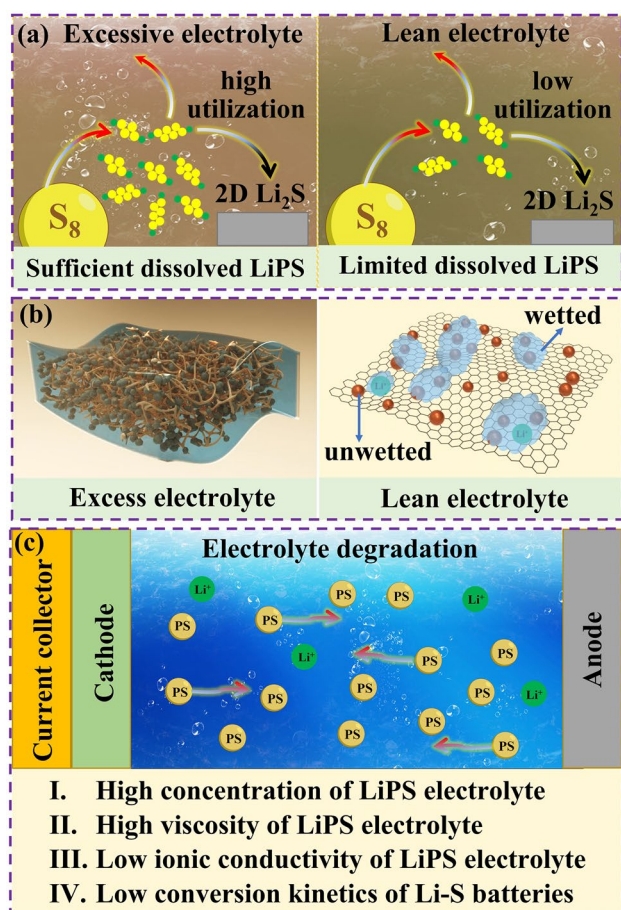
Fig. 7 Shortcomings of lean electrolyte: **a** sluggish kinetics of LiPS conversion. **b** Partially wetted surface. **c** Electrolyte degradation and high concentration of LiPS

efficiency. The extensive use of conductive carbon matrixes effectively reduces the electrode internal resistance, but the physical entrapment based on weak van der Waals forces of carbon-based materials is insufficient to suppress the shuttle effect of LiPS. Therefore, the search for materials that catalyze the conversion reaction of LiPS and have greater adsorption capacity has become a hot research topic in recent years. Polar transition metal-based compounds can form chemical bonds with LiPS, which are based on Lewis acid–base interactions and are stronger than the physical bonds that occur on carbon-based materials. Many transitions metal-based compounds have been shown to accelerate the electrochemical reactions of LiPS [15, 51, 87–92], such as metal nanoparticles (TMs), metal oxides (TMOs), metal chalcogenides (TMCls), metal phosphides (TMPs), metal nitrides (TMNs), metal carbides (TMCs) and metal–organic frameworks

(MOFs), single atoms (SAs). Considering the price, abundance, tunable properties, etc., of the elements in the periodic table, transition metal compounds as catalysts for sulfur redox reactions in Li–S batteries exhibit large advantages (Fig. 8), such as (a) Abundance: most of the transition metal compounds used in Li–S batteries are relatively abundant in the earth's crust, making them more accessible and cost-effective compared to other precious metals such as gold or platinum. This makes them an attractive option for industrial scale applications; (b) Tunable properties: the properties of transition metal compounds can be fine-tuned by varying factors such as the metal used, the ligands attached to the metal and the reaction conditions. This allows for greater control over the reaction and improves efficiency. In Li–S batteries, transition metal-based catalytic host materials have shown promising results in improving the sulfur redox reaction and facilitating LiPS conversion by reducing the activation energy. In general, a lower E/S ratio can be employed when using catalytic host materials with high catalytic activity and efficient LiPS conversion. A lower E/S ratio implies a higher concentration of LiPS in the electrolyte, and efficient catalysts can accelerate the conversion of LiPS, enabling a more rapid and efficient utilization of sulfur species.

Here, the strengths and limitations of transition metal-based compounds are systematically discussed and presented from a fundamental perspective (Fig. 9). This review is focused on recent advances in the use of transition metal-based carbon materials as sulfur hosts for Li–S batteries under lean electrolyte conditions. Firstly, the principles, structure and challenges of Li–S electrochemical conversion under lean electrolyte conditions are discussed in more detail. In addition, the influence of the E/S ratio on the energy density is systematically analyzed. Then, current strategies for cathode hosts and structure design based on transition metal–carbon compounds are addressed. Finally, perspectives on lean electrolyte Li–S cells are presented to guide future research on Li–S batteries.

2 Li–S batteries Based on Transition Metal Carbon Materials

Under lean electrolyte conditions, the concentration of dissolved LiPS becomes high, increasing the viscosity of the electrolyte, resulting in incomplete wetting of the cathode, slow ion transport and sluggish redox kinetics of LiPS

Fig. 8 Illustration of the abundance in the Earth's crust and the price fluctuations of the elements associated with catalysts in Li–S batteries (data from Wikipedia)

[93, 94]. At the same time, the high concentration of LiPS increases the LiPS shuttle effect and anode corrosion. To solve these issues, the electrochemical kinetics of LiPS need to be accelerated [78]. Several studies have shown that heterogeneous redox mediators or electrocatalysts can speed up LiPS conversion by decreasing the activation energy [82]. Such a faster adsorption-diffusion-conversion process at the electrode/electrolyte interphase can buffer the severe LiPS shuttle effect while at the same time preventing LiPS aggregation to achieve longer cycle life.

2.1 Metallic Nanoparticles

2.1.1 Elemental Metallic Nanoparticles

Transition metals catalysts are widely applied in chemical reactions, environmental restoration and energy
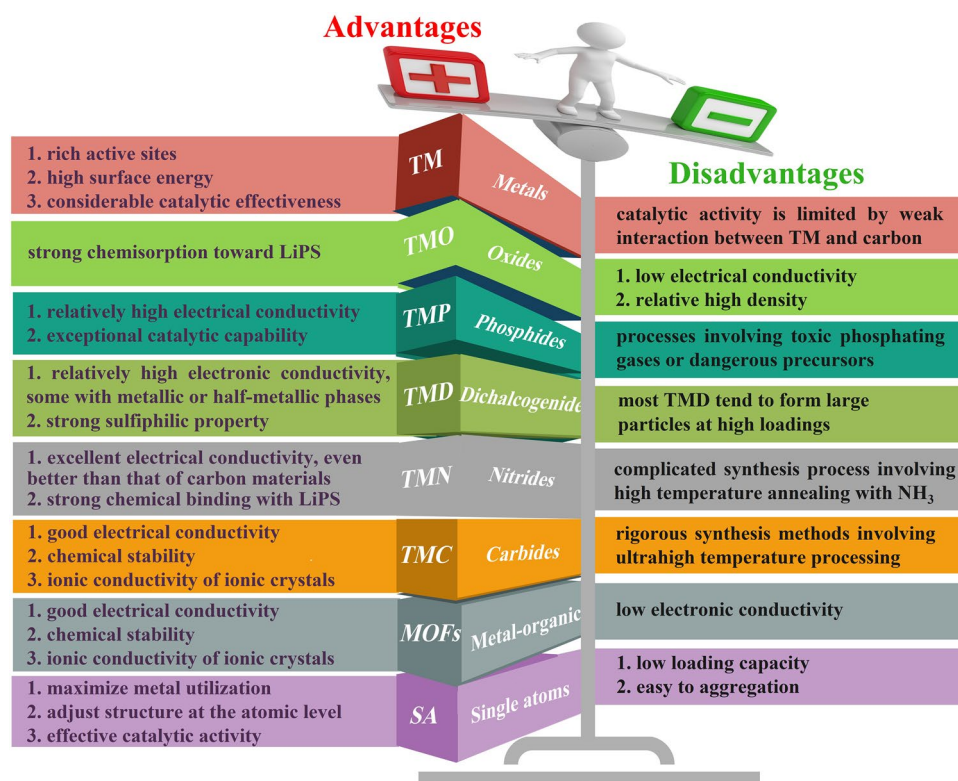
Fig. 9 Schematic representation of the advantages and disadvantages of transition metal-based compounds in Li–S batteries

transformation [95–102]. The beneficial effects of transition metal nanoparticles on the performance of Li–S cells depend mainly on the adsorption and electrocatalytic effect of LiPS [29, 103–106]. Beyond noble metal electrocatalysts, some abundant transition metals have been demonstrated to be extremely effective electrocatalysts for LiPS conversion [107–109]. Such nanoparticles are generally anchored to carbon frameworks to maximize particle dispersion and facilitate charge and ionic transport [110–123]. Table 2 summarizes the application of transition metal nanoparticles in lean electrolyte Li–S batteries. Cobalt (Co) nanoparticles embedded into carbon materials as sulfur hosts are the most widely studied for lean electrolyte Li–S batteries [93, 124–131]. Chen's team designed a stringed "cube on tube" nanohybrid with abundant nitrogen (N) and Co sites as cathode matrices for Li–S batteries under lean electrolyte conditions [132]. The fabrication process of the sulfur host is shown in Fig. 10a. ZIF67 cubes are combined with polyacrylonitrile (PAN) into electrospun nanofibers that are calcined. Then, CNTs are grown using a chemical vapor deposition (CVD) to further construct a hierarchical structure of interconnected and freestanding fibers containing Co particles (denoted as CPZC). The relative contents of N and Co in the as-developed CPZC fabric are estimated to be 7.8 and 13.1 wt%. The batteries based on S@CPZC electrodes delivered an excellent areal capacity of 14.2 mAh cm^{-2} with high sulfur loading (13.5 mg cm^{-2}) and lean electrolyte conditions (4.5 mL g^{-1}) at 0.05C, which is associated with the high conductivity, and strong physical and chemical adsorption of the hierarchical matrix. Co/N has also been investigated as dual lithiophilic-sulfiphilic sites in Li–S batteries. In this direction, Li's group designed an interlaced 2D structure including Co/N co-doping (Fig. 10c) [133]. Specifically, metal Co nanoparticles were used as sulfiphilic sites to bind the anions of LiPS (S_x^{2-}, $x = 1$–8), and N heteroatoms were utilized as lithiophilic sites to anchor LiPS by interaction with Li$^+$. The N and Co atomic ratio was around 6.95 and 0.22%, respectively. This dual adsorption sites allow the host materials to achieve uniform distribution of Li$_2$S, associated with a strong trapping ability and a fast conversion kinetics of LiPS. Furthermore, Co electrocatalyst has been shown to have a significant catalytic effect on the LiPS conversion reaction. Ye et al. employed Fe–N and Co–N co-doped carbons as stepwise electrocatalysts to selectively catalyze the conversion

of LiPS (Fig. 10d, e) [93]. The relative contents of Fe and Co were estimated to be 4.13 and 3.73 wt%. The authors applied a mixture of sulfur and Fe–N@C as an inner layer and Co–N@C as an outer layer. During the discharging process, long-chain polysulfides formed in the Fe–N@C layer migrated outward and were catalytically reduced to short-chain Li$_2$S in the Co–N@C layer. During the charging process, Li$_2$S in the Co–N@C layer was catalytically oxidized to long-chain polysulfides and migrated inward into the Fe–N@C layer for further conversion to sulfur. As a result, the batteries based on the dual-catalyst layer as sulfur hosts had high areal capacity with a low E/S ratio of 5. The specific capacity of low E/S (5 μL mg^{-1}) is lower than that of high E/S (15 μL mg^{-1}) due to lean electrolyte resulting in an insufficient dissolution of LiPS, which hinders the utilization of sulfur and thus leads to a low areal capacity (Fig. 10f). Gu's group also employed Co nanoparticles and Co-N$_x$ co-doped carbon nanotubes embedded in a carbon foam to form a 3D freestanding framework (Co-NCNT@CF) (Fig. 10g) [134]. The high-resolution Co 2$p_{3/2}$ spectrum exhibited two peaks of metallic and divalent Co, indicating a strong interaction between Co and N-doped carbon. Additionally, the C K-edge X-ray absorption near-edge structure (XANES) spectrum displayed multiple peaks for a π^* transition (284.5 eV) and σ^* transition (292.1 eV), with a weak peak (289.7 eV) presented between the π^* and σ^* transitions, indicating that Co–N–C bonds may have formed in the Co-NCNT@CF composite. These results suggested a high dispersion Co-N$_x$ species that provided strong LiPS trapping and promoted the catalytic reaction of LiPS by modifying the electron distribution.

Combining a semiconductor and a metal to form a Mott-Schottky effect may induce interfacial electronic interactions that enhance the catalytic activity [112]. However, the use of Mott-Schottky effect for LiPS catalytic conversion chemistry is rarely reported. Sun's group employed an N-doped carbon (NC) semiconductor matrix to obtain Co@NC heterostructure as Mott-Schottky catalysts and explored its performance on the LiPS redox reaction (Fig. 11a, b) [112]. As shown in Fig. 11b, in the Mott-Schottky heterojunction, electron transmission can lead to charge separation and produce an internal electric field at the interface, accelerating charge transfer and ion diffusion and lowering the activation energy barrier for catalytic conversion reactions. The authors calculated that

Table 2 Representative summary of TMs for the performance of lean electrolyte Li–S batteries

Cathode materials	S loading (mg cm^{-2})	S content (%)	Capacity (mAh g^{-1}/cm^{-2})	E/S ratio (μL mg^{-1})	Cycle Life (cycle)	References
Ni-CF/S nanoparticles	5	64	~900 mAh g^{-1} at 0.1C	5	150	[103]
Co-NCNT@CF/S nanoparticles	7	–	4.34 mA cm^{-2} at 0.1C	5	After 100	[134]
Co/CNTCNF/PS nanoparticles	5.1	75.2	3.9 mAh cm^{-2} at 0.2C	6	After 300	[132]
Co/CNTCNF/PS nanoparticles	9.2	75.2	6.5 mAh cm^{-2} at 0.2C	6	50	[132]
Mo/CNT/PS nanoparticles	7.64	–	4.75 mAh cm^{-2} at 0.2C	8	After 100	[95]
S/Co-NC@TpBDMe$_2$ nanoparticles	5.71	69.5	4.53 mAh cm^{-2} at 0.2C	6.1	After 50	[135]
WIT-Co/S nanoparticles	5.6	80	4.8 mAh cm^{-2} at 0.2C	5	After 100	[102]
Co@NC/S nanoparticles	10.73	–	6.74 mAh cm^{-2} at 0.2C	5.9	120	[112]
S/Co@N-HCMSs	5.1	90.52	5 mAh cm^{-2} at 0.1C	10	50	[136]
Cu-Mo@NPCN/6.5S nanoparticles	10.3	85	906 mAh g^{-1} at 0.2C	10	150	[137]
Fe-N/Co–N@C nanoparticles	6.8	–	1316 mAh g^{-1} at 0.5 mA cm^{-2}	4	600	[122]
Co-Bi/rGO-S nanoparticles	4.2	72	700.8 mAh g^{-1} at 0.2C	6	10	[111]
Fe-Ni/S alloy	4.1	–	1160 mAh g^{-1} at 0.1C	8	200	[138]
Fe–Ni/S alloy	6.4	86	6.1 mAh cm^{-2} at 0.1C	8	100	[138]
S/HEA-NC alloy	27	–	868.2 mAh g^{-1} at 0.45 mA cm^{-2}	3	10	[139]
S/CNC Ni-Pt/G alloy	8.8	75.6	664.9 mAh g^{-1} at 0.03C	5	40	[140]

the difference in activation energy for the rate-limiting step (the reduction of Li$_2$S$_n$ into Li$_2$S) of the Co@NC/S and NC/S cathode was 23.9 kJ mol^{-1} during the discharge process (Fig. 11c). They also calculated an activation energy difference between the Co@NC/S and NC/S cathodes of 28.6 kJ mol^{-1} in the charging process. The decrease in activation energy values revealed enhanced conversion kinetic of the sulfur species with the Co@NC Mott-Schottky catalysts during both charging and discharging. Recently, our group reported a 3D conductive nitrogen-doped honeycomb porous carbon (Co@N-HPC) with isolated Co nanoparticles as cathode material under lean electrolyte conditions to study the electrochemical performance in Li–S cells (Fig. 11d, e) [141]. The relative contents of N and Co in Co@N-HPC were estimated to be 6 and 6.1 wt%. Just like natural honeycombs, the 3D honeycomb structure contains multiple channels and cobalt

nanoparticle-embedded porous walls (carbon nanosheets), which are beneficial for fast Li$^+$ ion diffusion and electron transfer. Active sites for bonding with sulfur species are provided by the widely dispersed Co nanoparticles embedded in the N-doped carbon framework and the formation of Co–N–C coordination centers.

Apart from Co nanoparticles, carbon materials decorated with nickel (Ni) nanoparticles have also been explored as electrocatalysts for lean-electrolyte Li–S batteries [142]. Bao et al. designed a carbon flower structure decorated with Ni nanoparticles as a reliable sulfur host to inhibit the LiPS shuttle and promote the reaction kinetics under a low E/S ratio of 5 μL mg^{-1} [103]. As shown in Fig. 11f, g, Ni nanoparticles are encapsulated in porous carbon with a flower shape, resulting in a short ion transfer distance. The authors have verified that 3.76 wt% of Ni was incorporated onto the CF. This flower-shaped
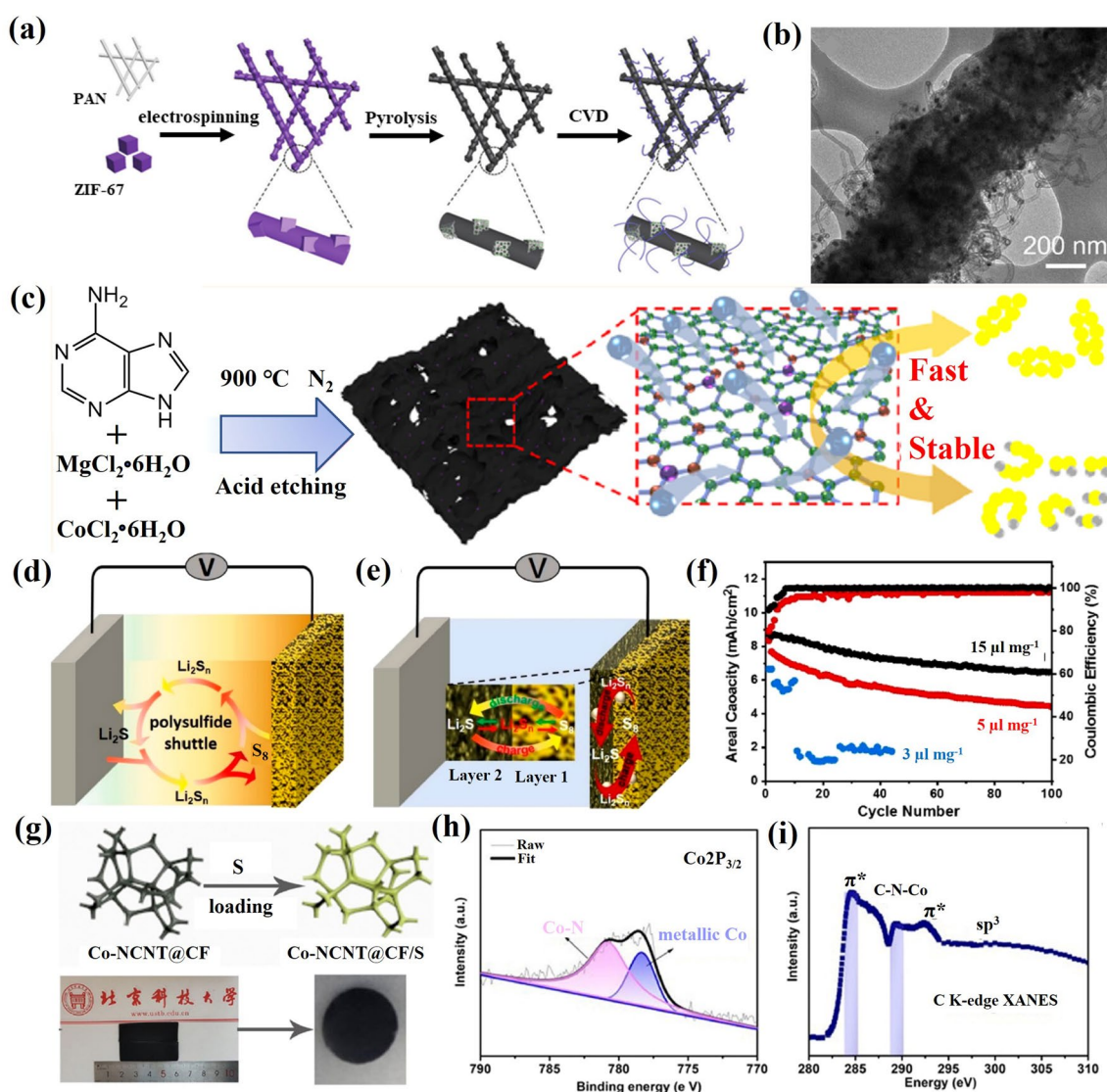
Fig. 10 **a** Schematic representation of the fabrication of CPZC fabrics. **b** TEM image of the CPZC fibers [132]. Copyright 2018, Royal Society of Chemistry. **c** Schematic illustration of the synthesis of Co-CNCs [133]. Copyright 2019, American Chemical Society. Shuttle effect of LiPS with **d** a traditional sulfur host and **e** a dual-catalyst layer sulfur host. **f** Cycling performance of the Fe/Co–N@C/S electrodes at 0.4 mA cm^{-2} [93]. Copyright 2019, American Chemical Society. **g** Digital photographs of Co-NCNT@CF/S. **h** XPS of Co 2p for Co-NCNT@CF. **i** C K-edge XANES spectra of Co-NCNT@CF [134]. Copyright 2021, Elsevier

structure has a small pore size (below 10 nm) and a high specific surface area (above 3300 m^2 g^{-1}). This particular morphology facilitates the penetration of the electrolyte and shortens the ion diffusion distance. As a result, the cycle performance shown in Fig. 11h indicates that the Ni-CF/S sulfur cathode with a high sulfur loading of 5 mg cm^{-2} and low E/S of 5 μL mg^{-1} maintains 87% of its initial capacity value after 50 cycles at 0.1C.

2.1.2 Alloy Nanoparticles

Metal alloys can enhance the catalytic ability of elemental metals through several different mechanisms [143, 144]. Within lean electrolyte Li–S batteries, transition metal alloys show a particular potential associated with their strong catalytic activity for the conversion of sulfur species [145–148]. In this regard, Manthiram's group engineered Fe–Ni alloys
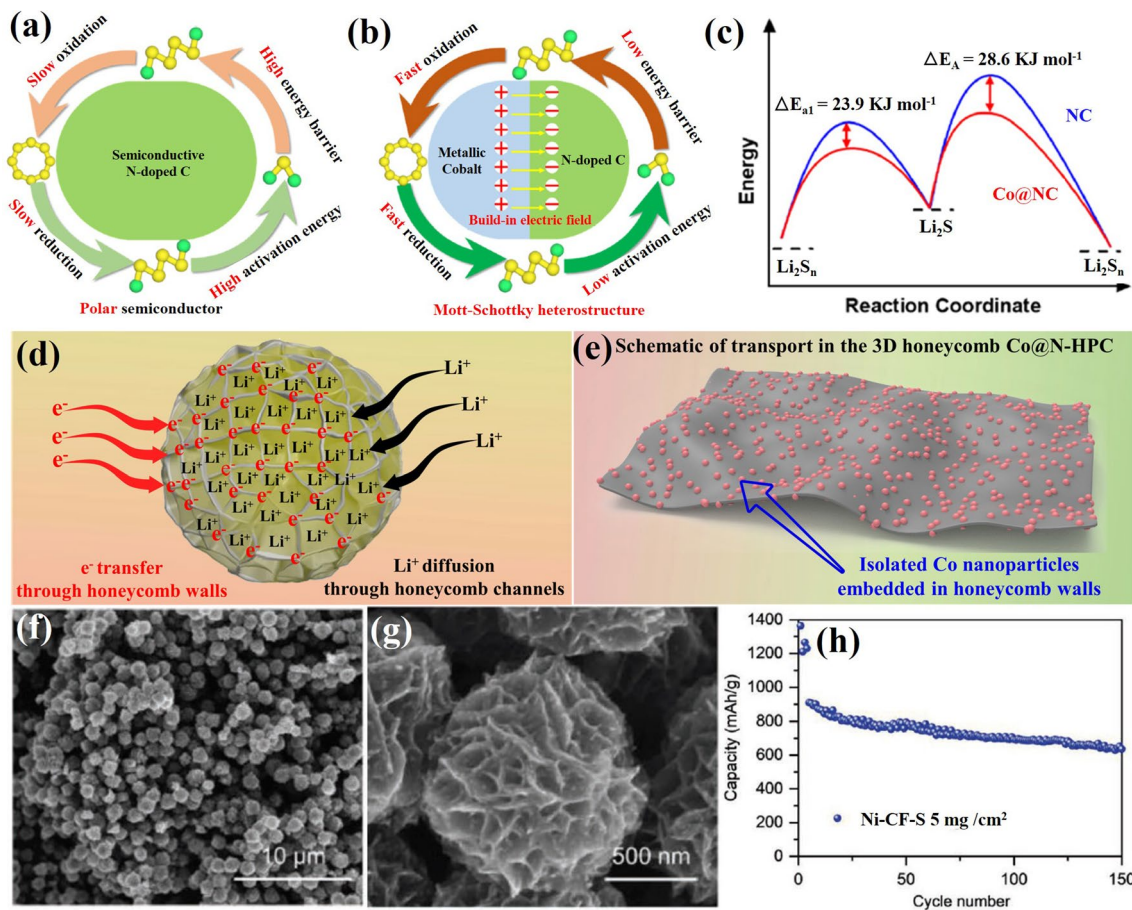
Fig. 11 Scheme of **a** an N-doped carbon (NC) semiconductor and **b** a Co@NC Mott-Schottky heterostructure. **c** The activation energies (E_a) for Li_2S formation and dissolution in NC and Co@CN [112]. Copyright 2021, American Chemical Society. **d** Illustration of electron transfer and ion diffusion in the 3D N-doped honeycomb porous carbon. **e** Schematic illustration of honeycomb walls containing evenly dispersed cobalt nanoparticles [141]. Copyright 2022, Springer Nature. **f, g** SEM images of carbon flower with Ni nanoparticles (Ni–CF). **h** The cycling performance of Ni–CF/S electrodes with a sulfur loading of 5 mg cm^{-2} and low E/S ratio of 5 μL mg^{-1}. The batteries were cycled at 40C at 0.1C after being tested initially at 0.05C [103]. Copyright 2021, Wiley-VCH

with the hexagonal close-packed (hcp) structure as catalysts through solid-state reactions to enhance the conversion reaction kinetics of LiPS (Fig. 12a, b) [138]. They demonstrated that the efficient catalytic activity of Fe–Ni alloys came from two components: (1) the pristine nanoscale Fe–Ni structure offers active sites and guarantees high catalytic ability; (2) the thin layer plated on the Fe–Ni alloy consists of various sulfurized phases of Fe/Ni sulfides formed in situ during melt-diffusion and with a long duration in the polysulfide-rich environment, which are catalytically active. In situ XRD was used to explore the evolution of the catalysts during the polysulfide conversion process (Fig. 12c, d). The prominent peak in the XRD signal at 27° in the case of Fe–Ni/S cells is caused by the Li_2S produced in these cells during discharge.

In contrast, even near the end of the discharge, the C/S cell does not exhibit Li_2S peaks. This result suggests that Fe–Ni alloy catalysts accelerate the conversion of LiPS and activate the formation of Li_2S. The intensity of the Li_2S peak gradually decreases during the charging process, showing the transformation of Li_2S into polysulfides bound to the Fe–Ni alloy surface. These results demonstrate the Fe–Ni alloy to be an effective catalyst for the LiPS conversion, providing good cycling performance for Li–S pouch cells with low electrolyte content. Nickel, one of the most used transition metal catalysts, and other Ni-based alloys have also been tested within Li–S batteries. For example, Li et al. explored the use of Ni_2Co alloys supported on flower-like graphene structures obtained by combining spray drying and
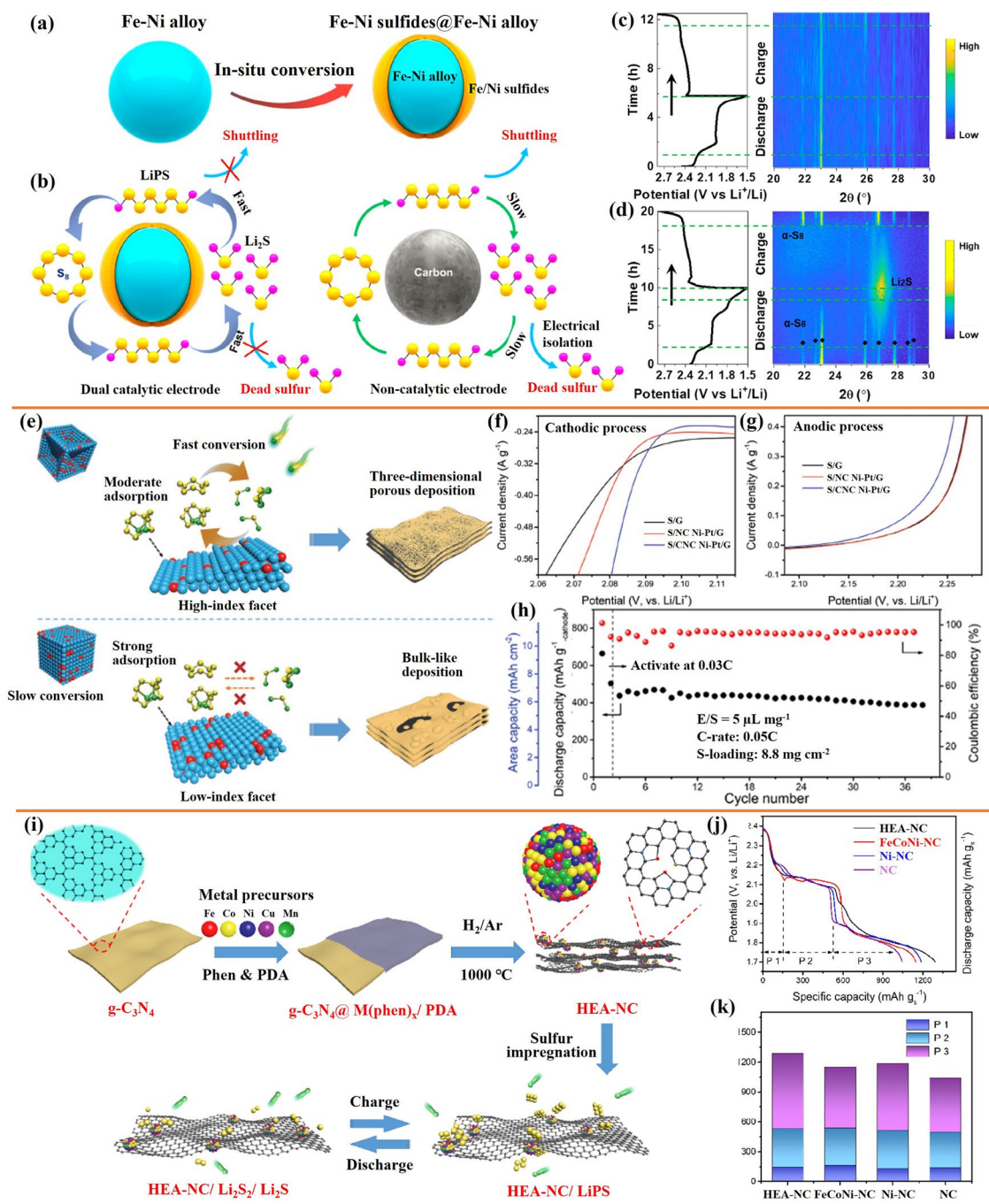
Fig. 12 **a** In situ plating of an Fe–Ni alloy with an iron/nickel sulfide layer. **b** Advantages of Fe–Ni alloys. In situ XRD plots of **c** C/S and **d** Fe–Ni/S, the discharge–charge curve is on the left, while the diffraction intensity map is on the right [138]. Copyright 2021, American Chemical Society. **e** Schematic representation of the conversion of LiPS and the precipitation of Li$_2$S on Ni–Pt alloy with different facets. **f**, **g** Partial enlargement of the cathodic and anodic processes from the CV curve. **h** Cycling performances of the S/CNC Ni–Pt/G electrodes at 0.05C [140]. Copyright 2022, Wiley-VCH. **i** Schematic representation of the synthesis process of HEA-NC and the promoted conversion reaction of LiPS on the HEA-NC sulfur host. **j**, **k** Li$_2$S$_6$ test potential curves and the distribution of specific capacity of the various catalysts, P1 (Li$_2$S$_6$ to Li$_2$S$_4$), P2 (Li$_2$S$_4$ to Li$_2$S$_2$) and P3 (Li$_2$S$_2$ to Li$_2$S) [139]. Copyright 2022, Wiley-VCH

high-temperature carbonization, as a bi-service (sulfur host and anode) matrix [149].

The catalytic ability of metal catalysts is highly influenced by the atomic arrangement on their surface and associated configuration. High-index facets (HIFs) have a high density of low-coordinated atoms and are more active than low-index facets (LIFs). Guo's group designed concave-nanocubic Ni–Pt (CNC Ni–Pt) alloys bound by exposed HIFs as efficient electrocatalysts for Li–S batteries (Fig. 12e) [140]. Compared to the traditional nanocubic Ni–Pt (NC Ni–Pt) alloys with LIFs, HIFs offer moderate adsorption of LiPS and reduce the energy barriers to LiPS conversion, significantly promoting the reaction kinetics of the sulfur species. The S/CNC Ni-Pt/G cathode exhibits the highest cathodic peak onset potential and the lowest anodic peak onset potential (Fig. 12f, g), indicating quicker electrochemical kinetics and significantly reduced polarization by CNC Ni–Pt alloy. As a result, the S/CNC Ni–Pt/G-based Li–S batteries delivered a high initial capacity (665 mAh $g^{-1}_{-cathode}$) even with a high sulfur loading of 8.8 mg cm^{-2} and a low E/S ratio of 5 μL mg^{-1} (Fig. 12h). The same group proposed the $Fe_{0.24}Co_{0.26}Ni_{0.10}Cu_{0.15}Mn_{0.25}$ high-entropy alloy (Fe–Co–Ni–Cu–Mn HEA) as a catalyst for lean electrolyte Li–S batteries [139]. The highly disordered structure of HEAs at the atomic level with strong lattice distortions often results in high catalytic activity for redox reactions. Fe–Co–Ni–Cu–Mn HEA nanocrystals on nitrogen-doped carbon (NC) substrate (denoted as HEA-NC) were prepared by a reflow process and high-temperature carbonization procedure (Fig. 12i). They demonstrated the Fe–Co–Ni–Cu–Mn HEA nanocrystals have a higher catalytic effect for LiPS conversion than ternary Fe–Co–Ni alloy, while the promoted electrochemical kinetics further leads to a rapid transfer of ions and electrons, thus accelerating the solid–solid (Li_2S_2 to Li_2S) transformation and improving the deposition capacity. Figure 12j, k shows that the HEA-NC electrode contributes the most capacity in the conversion of Li_2S_2 to Li_2S, indicating that the Fe–Co–Ni–Cu–Mn HEA nanocrystals helped to speed up the conversion of Li_2S_2 to Li_2S, achieving high sulfur utilization. Moreover, the cells delivered a discharge capacity of 868 mAh $g_{-cathode}^{-1}$ even under both ultrahigh sulfur loading (27.0 mg cm^{-2}) and low E/S ratio (3 μL mg^{-1}) conditions. This work provides a methodology for researching catalytic host materials to improve the utilization of sulfur in Li–S cells. Table 2 summarizes additional works on alloy nanoparticles for lean electrolyte Li–S batteries.

In general, transition metal nanoparticles and alloy nanoparticles coupled with carbon materials are some of the most promising electrocatalysts to realize high sulfur utilization and long cycle life under lean electrolyte conditions. The dispersion of the metal onto suitable carbon substrates allows for maximizing the surface area and the number of active sites. However, the use of these catalysts is often limited in practical applications due to their high cost, as they may involve expensive noble metals or heavy metals that are not economically feasible.

2.2 Transition Metal Oxides

Transition metal oxides (TMOs) have been used primarily to trap and block the diffusion of highly soluble LiPS at the cathode, thereby alleviating the shuttle effect of LiPS between the cathode and anode [150–161]. A summary of the metal oxide compounds used in lean electrolyte Li–S batteries and their corresponding properties is provided in Table 3.

The significantly different electronegativities of oxygen anions and metal atoms provide metal oxides with strong polarity to chemically interact with polar LiPS or form polythionate complexes that inhibit the shuttle effect of LiPS [167]. However, most TMOs are not suitable for direct service as sulfur hosts owing to their low electrical conductivity and poor catalytic capability. Besides their relatively high weight prevents the use of significant loads of TMOs at the cathode. Thus, TMOs are generally supported on carbon materials to achieve good performance under lean electrolyte conditions [154]. For example, Zhang and co-workers proved that a hyperbranched polymer-coated MOF-derived zirconium nitrogen oxides and N-doping carbon composites (Zr_2N_2O/NC-6) possessed rapid Li^+ transfer, LiPS anchoring and multiple functional sites [164]. Wang's group constructed sulfiphilic Fe_2O_3 nanocrystals restrained in lithiophilic N-doped microporous carbon (Fe_2O_3/NMC) to act as sulfur immobilizers for efficient Li–S batteries [168].

Recently, TMOs loaded on carbon materials with oxygen vacancies have been employed as catalytic hosts for Li–S batteries under low electrolyte/sulfur ratios [164, 169, 170]. Chen's group designed a 3D ordered macroporous framework of niobium oxide (Nb_2O_{5-x}) with oxygen defects as catalytic centers to facilitate the conversion of LiPS [155]. As shown in Fig. 13a, the 3D ordered open and porous

framework benefits electrolyte impregnation for rapid Li^+ diffusion and interfacial exposure to achieve more host–guest interactions. Furthermore, CNTs embedded in the oxygen-deficient Nb_2O_{5-x} backbone improve the electrical conductivity and catalytic activity. Thanks to these architectural and chemical advantages, S-Nb_2O_{5-x}/CNTs-based Li–S batteries offer good cyclability with increased sulfur loading and lean electrolyte conditions. The same group also proposed Ta_2O_{5-x} with oxygen vacancies embedded in a "ship in a bottle" nanostructure as a catalyst and adsorber for LiPS reaction and retention (Fig. 13b) [162]. The pores of carbon nanospheres restrain the Ta_2O_{5-x} nucleation to tune the crystal parameters, thus reducing the length of the Ta–O bond and strengthening the chemical affinity between Ta_2O_{5-x} and LiPS. In addition, the atomic coordination and electron band structure of Ta_2O_{5-x} are modified by the oxygen vacancies to increase the electrical conductivity and serve as a catalytic accelerator. Theoretical calculations were used to clarify the effect of oxygen defects on electrical conductivity. As shown in Fig. 13c, the defect-engineered a-Ta_2O_{5-x}/MCN exhibits a smaller band gap than the control sample a-Ta_2O_5/MCN, proving the band engineering. This work applies tantalum as a novel catalyst material at practically applicable sulfur loading and electrolyte content, extending the usage of transition metals in Li–S batteries. Quantum dots with ultra-fine particle size (< 10 nm) have their unique advantages compared to nanoparticles (> 10 nm) in Li–S batteries. They offer quantum confinement effects, high surface-to-volume ratios, and most are semiconductive. As

a result, these catalysts have demonstrated promising performance in Li–S batteries and have been extensively investigated [171]. For example, Sun's group demonstrated that oxygen-vacancy-rich Ti_nO_{2n-1} (Ti_2O_3 and Ti_3O_5) quantum dots loaded on porous carbon nanosheets can bind LiPS via strong chemisorption and facilitate the transformation of LiPS through a mechanism involving the oxygen vacancies (Fig. 13d) [163]. Owing to the efficient LiPS anchor and high electrocatalytic activity, the cathodes with high sulfur loading (4.8 mg cm^{-2}) and low E/S ratio (4.5 μL mg^{-1}) exhibited excellent rate performance, with a capacity of 580 mAh g^{-1} achieved even at a current rate of 2C. Jiang's team utilized $NiFe_2O_4$ quantum dots to build hybrid cathodes with an appropriate tap density (~ 1.32 g cm^{-3}) for high-performance Li–S cells. In 2020, the authors applied the unique properties of $NiFe_2O_4$ quantum dots, including excellent chemisorption and catalytic effects on lithium polysulfides, to contribute to the high-rate performance and cycling stability of the $NiFe_2O_4$-based battery [172]. In 2023, the authors further encapsulated $NiFe_2O_4$ quantum dots into nitrogen-rich carbon shells to make microsphere cathodes with high-tap-density (maximum 2.12 g cm^{-3}). Such cathodes demonstrated high sulfur utilization and good cyclic behavior [173]. Guo's team constructed a multiple confined sulfur host by filling graphitized *Pinus sylvestris* with carbon nanotubes and defective $LaNiO_{3-x}$ (LNO-V) nanoparticles (Fig. 13e) [165]. The authors used DFT calculations and experimental results to demonstrate that the unique morphology physically confines LiPS within the microchannel

Table 3 Representative summary of TMOs for the performance of lean electrolyte Li–S batteries

Cathode materials	S loading (mg cm^{-2})	S content (%)	Capacity (mAh g^{-1}/cm^{-2})	E/S ratio (μL mg^{-1})	Cycle life (cycle)	References
a-Ta_2O_5-x/MCN/S	5.6	–	5 mAh cm^{-2} at 0.2C	3.6 mL g^{-1}	200	[162]
MnO_2@rGO/S	4	70	188 Wh L^{-1} at 1.34 mA cm^{-2}	4	100	[154]
OV-T_nQDs@PCN/S	4.8	79.1	736 mAh g^{-1} at 0.5C	4.5	500	[163]
S/Zr_2N_2O/NC-6	8.16	77.68	7.2 mAh cm^{-2} at 0.2C	7.79	80	[164]
S@Fe_3O_4-NC	3.8	52	~1000 mAh g^{-1} at 0.3 mA cm-2	4.2	300	[152]
S-Nb_2O_5-x/CNTs	6	74	4.8 mAh cm^{-2} at 0.1C	4.4	After 100	[155]
GP/CNT/LNO-V-S	6	–	~1200 mAh g^{-1} at 0.05 C	3.8	20	[165]
S/CC@$NiCo_2O_4$	3.5	56	660 mAh g^{-1} at 0.2C	–	After 200	[166]
S/Zr_2N_2O/NC-6	8.16	77.68	7.2 mAh cm^{-2} at 0.2C	7.79	80	[164]
LLTO-10/CNT/S	5.2	–	4.5 mAh cm^{-2} at 0.2 mA cm^{-2}	5	35	[151]
S/CNT-LDH/Ar	5.5	72	4.4 mAh cm^{-2} at 0.1C	6	After 100	[115]
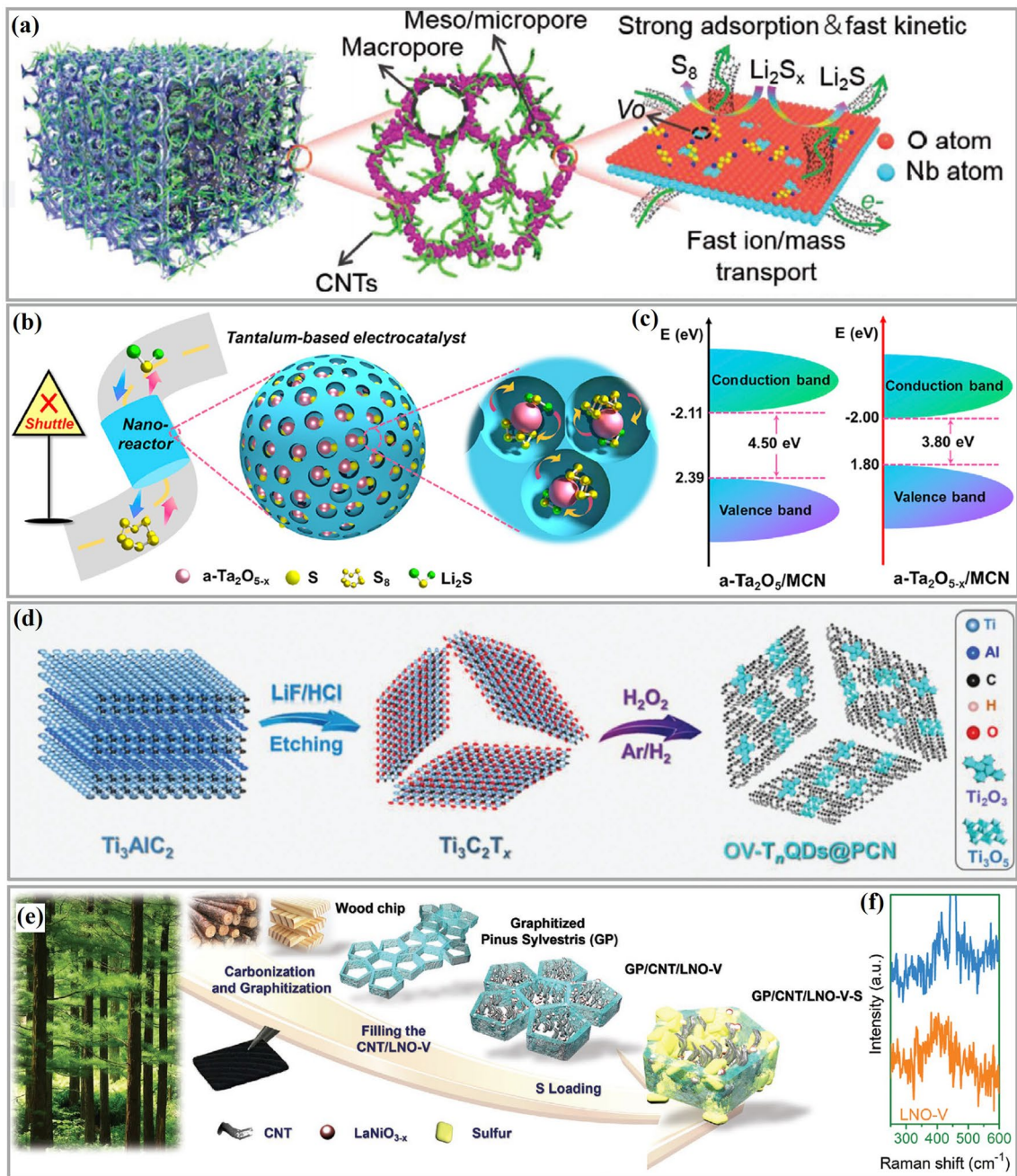
Fig. 13 **a** Schematic illustration of Nb_2O_{5-x}/CNTs [155]. Copyright 2020, Wiley-VCH. **b** Illustration of the production of a-Ta_2O_{5-x}/MCN/S. **c** Band graph of a-Ta_2O5_x/MCN and a-Ta_2O_5/MCN [162]. Copyright 2020, Cell Press. **d** Schematic illusion of the synthesis process of OV-T_nQDs@PCN cathodes [163]. Copyright 2021, Wiley-VCH. **e** Schematic representation of the preparation of GP/CNT/LNO-V-S materials. **f** Raman spectra of $LaNiO_{3-x}$ [165]. Copyright 2022, Wiley-VCH

and shows strong chemisorption and high catalytic activity for LiPS due to the spin density around the oxygen vacancies of $LaNiO_{3-x}$. Raman spectra indicated that $LaNiO_{3-x}$ nanoparticles had been successfully loaded into the GP/CNT/LNO-V-S sulfur host electrode (Fig. 13f). The GP/

CNT/LNO-V-S-based Li–S batteries showed good discharge capacity at high sulfur loadings and low electrolyte content.

In conclusion, most TMOs possess high surface polarity that facilitates the reaction with polar LiPS. Furthermore, TMOs with oxygen defects provide excellent catalytic

activity and stability for the conversion of LiPS. This, together with their simple synthesis makes them a promising sulfur host. However, TMOs need to be combined with carbon materials to increase their electrical conductivity and dispersion.

2.3 Transition Metal Phosphides

Like TMOs, transition metal phosphides (TMPs) are also characterized by notable polarity associated with the differential electronegativity between phosphorous and transition metals. P atoms with high electronegativity can gain electrons from metal atoms and serve as bases for trapping positively charged species [174–176]. In contrast to transition metal oxides, TMPs with the appropriate atomic ratio of metal to phosphide are frequently endowed with a metallic character and even superconductivity [15, 177]. Besides, TMPs can be produced using mild synthesis conditions and have easily tunable electronic configuration and excellent catalytic ability [89, 178, 179]. Thus, not surprisingly, TMPs have been investigated as LIPS adsorbers and catalysts within Li–S batteries [180–182]. A summary of TMPs and their performance in lean electrolyte Li–S batteries is presented in Table 4.

Cobalt phosphides, like typical TMPs, exhibit low overpotential for LiPS transitions, suggesting that they could

enhance the sluggish redox kinetics of LiPS and improve the rate performance of Li–S cells [188, 189]. Although most studies have concentrated on crystalline cobalt phosphide, the application of amorphous metal phosphides in lithium-sulfur batteries has also been investigated. For example, Sun et al. adopted amorphous cobalt phosphide grown on reduced graphene oxide-multiwalled carbon nanotubes (rGO-CNT-CoP(A)) as the cathode material (Fig. 14a) [183]. Compared to crystalline CoP, amorphous CoP enhances the chemisorption toward LiPS, promotes LiPS conversion and accelerates the nucleation and growth of Li_2S. In addition, DFT calculations show that amorphous CoP has higher binding energy and a lower diffusion energy barrier to LiPS. Furthermore, amorphous CoP decreases the energy gap and increases the electron concentrations of adsorbed LiPS close to the Fermi level. As a result, combining the advantages of conductive rGO-CNT and the amorphous CoP, the S/rGO-CNT-CoP(A) cathode provides a discharge capacity of 1006 mAh g^{-1} at 0.8 mA cm^{-2} under a sulfur loading of 5 mg cm^{-2} and an E/S ratio of 7 μL mg^{-1}.

Comparable to the large interest risen by oxygen vacancies in transition metal oxides and chalcogen vacancies in chalcogenides, recently the influence of phosphorus vacancies on the electrochemical performance of Li–S cells has been a topic of major relevance. As shown in Fig. 14b, CoP with phosphorus vacancies grown on CNT (CNT-CoP-Vp) was used as sulfur hosts with excellent characteristics. The

Table 4 Representative summary of TMPs for the performance of lean electrolyte Li–S batteries

Cathode materials	S loading (mg cm^{-2})	S content (%)	Capacity (mAh g^{-1}/cm^{-2})	E/S ratio (μL mg^{-1})	Cycle life (cycle)	References
S/rGO-CNT-CoP(A)	5.0	67	1006 m h g^{-1} at 0.8 mA cm^{-2}	7	100	[183]
CNT-CoP/GO-S	6	72	830 mAh g^{-1} at 0.8 mA cm^{-2}	4	50	[184]
CNTs-S@G/CTRu	6.5	80.6	698 mAh g^{-1} at 0.1C	9	After 120	[179]
CF/FeP@C@S	2.5	–	695 mAh g^{-1} at 1C	5	200	[174]
S/SnP0.94@PHCA	6.4	61.75	6.9 mAh cm^{-2} at 0.1 mA cm^{-2}	8.6	–	[175]
S/CNT-CoP-Vp	7.7	68	8.03 mAh cm^{-2} at 0.4 mA cm^{-2}	5	–	[185]
S/CNT-CoP-Vp	5.5	68	878 mAh g^{-1} at 0.8 mA cm^{-2}	7	After 30	[185]
S@Co–Fe–P	1	70	1118 mAh g^{-1} at 0.2C	–	100	[186]
MoP-CNT-10-S	4	72	886 mAh g^{-1} at 0.2C	6	100	[184]
PCPC/NiCoP/S	3.99	72	826.4 mAh g^{-1} at 1C	10	60	[182]
NCNT@Co-CoP@S	10	–	4.4 mAh cm^{-2} at 2C	7	After 100	[187]

electronic structure of CoP was modified with the introduction of phosphorus vacancies, leading to electron accumulation on Co and P atoms. The defect engineering by phosphorus vacancies enhanced the adsorption and catalytic activity toward polysulfides, resulting in promising electrochemical

properties. Thus, a high areal capacity of 8.03 mAh cm^{-2} was realized at 0.4 mA cm^{-2} under lean electrolyte (E/S = 5 μL mg^{-1}) and high sulfur loading (7.7 mg cm^{-2}) [185]. Besides, this same study revealed the mechanism of phosphorus vacancies for boosting electrochemical performance.
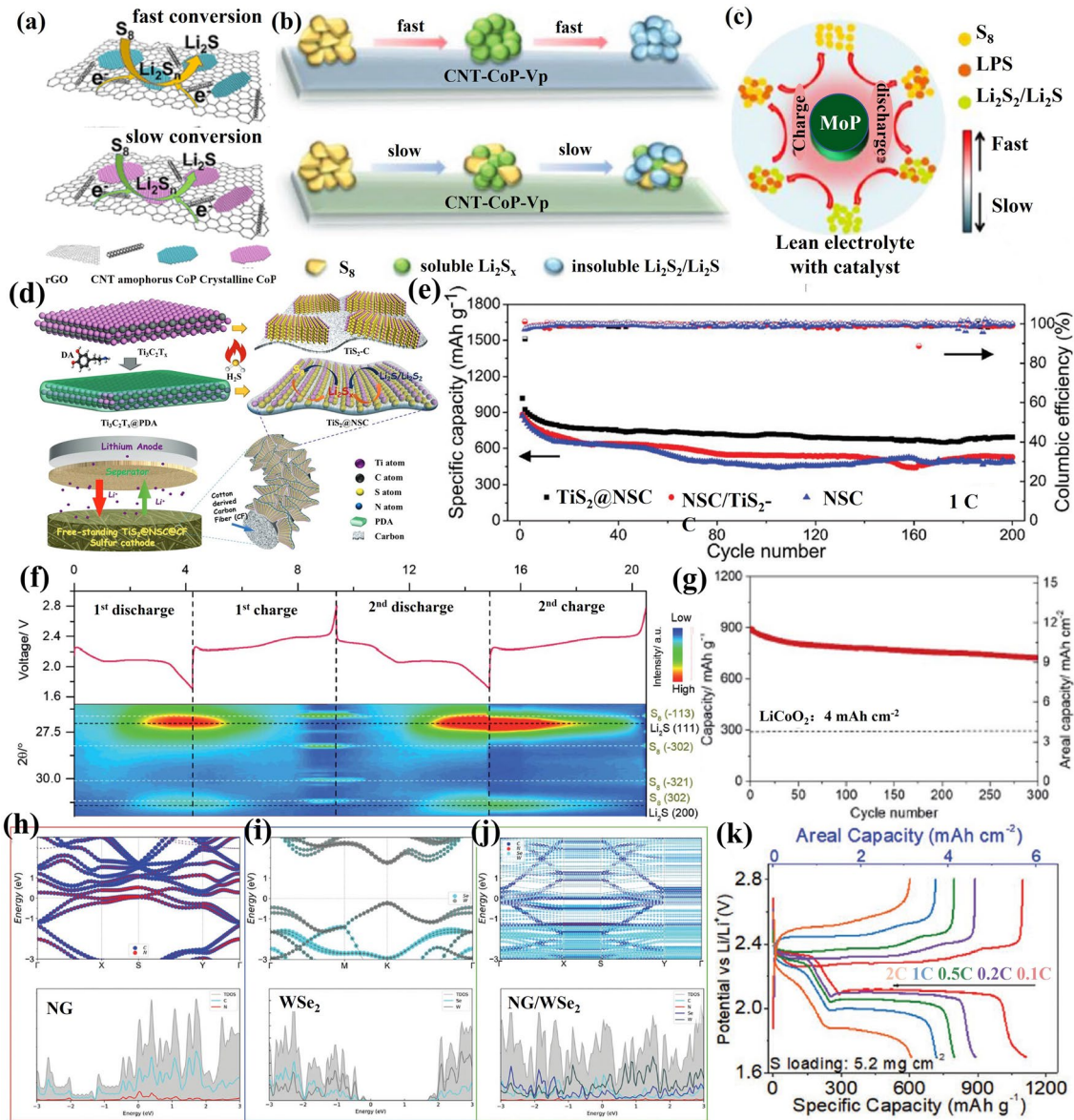

Fig. 14 **a** Schematic representation of the reduction processes of LiPS on amorphous CoP and crystalline CoP [183]. Copyright 2021, American Chemical Society. **b** Schematic diagram of the sequential catalytic reaction of LiPS on CNT-CoP and CNT-CoP-Vp [185]. Copyright 2022, Wiley-VCH. **c** Possible reaction routes are described for MoP-catalyzed sulfur cathode under lean electrolyte conditions [184]. Copyright 2018, Wiley-VCH. **d** Illustration of the synthesis of sandwich-shape, monolayer TiS$_2$ nanosheets confined within PDA derived N, S co-doped porous carbon. **e** Cycling performance of S/TiS$_2$@NSC, S/NSC/TiS$_2$-C and S/NSC cathodes at 1C with an E/S of 6 [190]. Copyright 2019, Wiley-VCH. **f** In situ XRD testing of the MoS$_2$ ND/porous carbon/Li$_2$S$_6$ electrode in the first two cycles. **g** Cyclic performance of MoS$_2$ ND/porous carbon/Li$_2$S$_6$ electrodes at a high sulfur loading of 12.9 mg cm^{-2} and a low E/S ratio of 4.6 mL mg^{-1} [191]. Copyright 2020, Royal Society of Chemistry. **h–j** HSE06 band structure and DOSs of **h** NG, **i** WSe$_2$ and **j** NG/WSe$_2$ superlattice. **k** Charge/discharge curves of S@NG/WSe$_2$ electrodes at various C-rates with a lower E/S ratio (11.6 mL g$^{-1}_{Sulfur}$) [192]. Copyright 2022, Wiley-VCH

The vast majority of cobalt phosphides investigated in Li–S batteries are CoP and Co_2P. Other valence states of cobalt phosphides still need to be further developed [193]. Molybdenum phosphide nanoparticles supported on CNTs have been also reported as electrocatalysts for stabilizing sulfur cathode under lean electrolyte conditions (Fig. 14c) [184]. Due to the excellent electrocatalytic capability of MoP, the MoP-CNT-10-S electrodes with a low E/S of 4 μL mg^{-1} achieved a capacity of 830 mAh g^{-1} (5.0 mAh cm^{-2}) at 0.8 mA cm^{-2}.

While it is agreed that the strong chemisorption and excellent electrocatalytic ability of TMPs greatly inhibit the shuttle effect of LiPS, only a few TMPs have exploded so far, and some TMPs with the same composition, but different valence states have not been studied. Furthermore, most of the work on TMPs as electrocatalysts for Li–S cells has focused on the catalytic effect under flooded-electrolyte conditions. The electrocatalytic mechanism in lean electrolyte Li–S batteries should also be further studied.

2.4 Transition Metal Chalcogenides

Transition metal chalcogenides (TMCls) also show a strong chemical affinity with LiPS associated with the electrostatic interaction between the positive metal ion and negative S_x^{2-} within the LIPS. The anchoring ability for LiPS depends strongly on the type of metal ion and to a less extent on the chalcogen, S, Se or Te. Regarding the design of sulfur hosts, TMCls combined with carbon materials have been widely studied as cathode materials in Li–S batteries [191, 194–203]. Table 5 shows an overview of TMCls and their performances in lean electrolyte Li–S batteries.

Transition metal sulfides are promising sulfur hosts in Li–S batteries due to their strong chemisorption and electrocatalytic activity for LiPS, which facilitates the redox kinetics of LiPS conversion [61, 209, 211–216]. Nanoscale transition metal sulfides frequently show favorable Li–S battery performance, like high specific capacity, long-term lifespan and low redox potential [217]. As the lightest member of transition metal chalcogenides, 2D titanium disulfide (2D TiS_2) nanosheets have recently received considerable attention. Wang et al. used TiS_2 nanosheets confined with N, S co-doped carbon (TiS_2@NSC) as sulfur hosts for high-performance Li–S batteries under lean electrolyte conditions [190]. The sandwich-like ultralight fluffy TiS_2@

NSC was prepared by in situ transformations of Ti_3C_2Tx MXene coated with polydopamine (PDA) (Fig. 14d). The introduction of PDA to MXene prevents Ti_3C_2Tx restacking and generates unique TiS_2@NSC structures. This sandwich structure of TiS_2 nanosheet immobilizes LiPS and provides high electrocatalytic activity for LiPS reduction and lithium sulfide oxidation. As a result, the freestanding S/TiS_2@NSC cathode shows very high discharge capacity and excellent cycling stability under an E/S ratio of 6 compared to S/NSC/TiS_2-C and S/NSC cathode (Fig. 14e). CoS_2 is a semi-metallic crystalline phase possessing a high electrical conductivity of 6.7 10^5 Ω^{-1} m^{-1} [218]. Li et al. designed dense graphene/CoS_2/nano-sulfur hybrid paper-like cathodes for high energy density lithium-sulfur batteries under a sulfur loading of 5.6 mg cm^{-2} and an E/S ratio of 5, highlighting their practical applications for power systems [206]. In addition, Zhao's group reported 0D NiS_2 nanoparticles on 1D carbon nanotubes (CNTs) supported on a three-dimensional carbon (3DC) framework (3DC-CNTs-NiS_2) as a sulfur host [205]. Due to the high specific surface area, good conductivity and adsorption and electrocatalysis of NiS_2 nanoparticles for LiPS, the soft package battery based on the S/3DC-CNTs-NiS_2 electrodes provided an areal capacity of 5.0 mAh cm^{-2} under an E/S ratio of 5 μL mg^{-1}.

MoS_2, a 2D layered transition metal dichalcogenide, has recently attracted particular attention [219–223]. To date, the MoS_2 crystal structures covering 1 T, 2H 3R and 1 T' (T-trigonal, H-hexagonal, R-rhombohedral and T'-distorted octahedral) have been widely acknowledged. The use of MoS_2 as a cathode material in Li–S batteries improves sulfur utilization and cell lifetime [224–227]. Xu and coworkers designed a small amount of 1 T MoS_2 nanodots (3% of the electrode) as robust electrocatalysts for lean electrolyte Li–S batteries [191]. Computational simulations indicate that the 1 T MoS_2 surface and Mo-rich edges have a stronger anchoring effect on LiPS, and a lower dissociation barrier of Li_2S, and faster diffusion of Li ions compared to the 2H phase. Electrochemical characterizations show that 1 T MoS_2 nanodots promote the trapping of LiPS and accelerate the redox reactions kinetics of LiPS. In situ XRD characterizations shown in Fig. 14f confirm the gradual appearance of Li_2S during discharge, reaching its maximum intensity at the end of lithiation. The XRD peaks of Li_2S gradually decrease in intensity during charging, until there are no discernible XRD peaks, after which peaks of monoclinic S_8 appear. All phase transitions are reversible during the 2nd discharge/

Table 5 Representative summary of TMCls for the performance of lean electrolyte Li–S batteries

Cathode materials	S loading (mg cm^{-2})	S content (%)	Capacity (mAh g^{-1}/cm^{-2})	E/S ratio (μL mg^{-1})	Cycle life (cycle)	References
S@NG/WSe$_2$	5.2	73.8	885.3 mAh g^{-1} at 0.5C	11.6 mL g^{-1}$_{Sulfur}$	350	[192]
S/WSe$_{1.51}$/CNT	9.3	72	5.6 mAh cm^{-2} at 0.1 C	5.5	After 50	[204]
S/WSe$_{1.51}$/CNT	12.7	72	7.7 mAh cm^{-2} at 0.1C	3.9	After 150	[204]
S/TiS$_2$@NSC@C	7.7	–	7.9 mAh cm^{-2} at 0.1C	8	100	[190]
S@3DC-CNTs-NiS$_2$	6.5	90	5 mAh cm^{-2} at 1.1 mA cm^{-2}	5	After 50	[205]
MoS$_2$ ND/porous carbon/Li$_2$S$_6$ cathode	12.9	81	9.3 mAh cm^{-2} at 0.05C	4.6	After 300	[191]
MoS$_2$ ND/porous carbon/Li$_2$S$_6$ cathode	9	–	6.2 mAh cm^{-2} at 0.05C	9.3	After 100	[191]
CC/MoSe$_2$@Li$_2$S$_8$	4	–	1204 mAh g^{-1} at 0.2C	6.2	After 100	[196]
MTQ@3DG/S	4.1	76.2	658.7 mA h g^{-1} at 0.1C	5.5	110	[200]
N-CoSe$_2$/S	10.2	70	9.26 mAh g^{-1} at 0.2C	4.4	70	[195]
c-(rGO-CoS$_2$)/S	5.6	68	6.67 mAh cm^{-2} at 0.05C	5	40	[206]
S@MoS$_2$@CNF	1.0–1.5	72.8	1398 mAh g^{-1} at 0.2C	6	400	[194]
VSe$_2$-VG@CC/S	1.4–1.7	70	1025 mAh g^{-1} at 0.5C	4.8	100	[207]
MoSe$_2$@C/rGO/S	4.7	73	911 mAh g^{-1} at 0.1C	10	30	[202]
CC@CS@HPP/S	5.6	72	4.1 mAh cm^{-2} at 0.1C	10	After 30	[208]
S@Co$_9$S$_8$/CNTs-Gr	7.2	75	~6 mAh cm^{-2} at 0.5C	10	After 300	[209]
FM@G/87S	–	87	905 mAh g^{-1} at 0.5C	6	120	[210]

charge process. When comparing the in situ XRD results with peer research, Xu and coworkers conclude that MoS$_2$ nanodots promote the formation of Li$_2$S crystals and the 1 T MoS$_2$ nanodots possess a high electrocatalytic capability. As a result, even at a sulfur loading of 12.9 mg cm^{-2} and an E/S ratio of 4.6, the MoS$_2$ nanodots/porous carbon/Li$_2$S$_6$ cathodes had areal capacities of 11.3 and 9.4 mAh cm^{-2} after the 1st and the 300th cycles, which is more than twice that of commercial LiCoO$_2$ cathodes (Fig. 14g).

Besides S-based chalcogenides, Se-based chalcogenides are also outstanding sulfur hosts. Cabot's group applied 2D N-doped graphene/WSe$_2$ (NG/WSe$_2$) superlattices with an adjustable bandgap to lean electrolyte Li–S batteries [192]. The authors controlled the interlayer spacing from 10.4 to 21 Å by adjusting the annealing temperature. Density functional theory (DFT) is used to identify the electronic band structure and density of states (DOS). As shown in Fig. 14h, NG displays a classic conductor structure and its DOS without a bandgap in the Fermi energy level. Compared to WSe$_2$ (Fig. 14i), NG/ WSe$_2$ superlattices have no bandgap at the Fermi level (Fig. 14j), indicating high electrical conductivity and rapid ion diffusion in NG/ WSe$_2$. As a result, S@NG/WSe$_2$ cathodes with a sulfur loading

of 5.2 mg cm^{-2} had a discharge capacity of 607 mAh g^{-1} at 2C (Fig. 14k). This work provides a simple strategy for synthesizing superlattice materials and opens up their practical applications in Li–S batteries. Se also is a good catalytic material owing to the presence of Se vacancies. Recently, Guo and co-workers designed a model of 2D WSe$_{2-x}$ with Se vacancies and edge dislocations as a host material to reveal how defects affect catalytic ability [204]. The authors quantitatively regulated the number of defects in WSe$_{2-x}$ by changing the W/Se ratio, and they found that an appropriate number of defects can enable materials with better catalytic performance. The adsorption capacity of the WSe$_{2-x}$/CNT materials with Li$_2$S$_6$ was investigated by DFT calculations (Fig. 15a): WSe$_{1.96}$ (−0.17 eV), WSe$_{1.61}$ (−0.61 eV), WSe$_{1.51}$ (−2.6 eV), WSe$_{1.33}$ (−2.91 eV). The adsorbed polysulfide presents improved charge density with sulfur in WSe$_{1.51}$/CNT compared to the co-existence of increasing and decreasing sulfur atoms in WSe$_{1.61}$/CNT and WSe$_{1.33}$/CNT, making it easier for the polysulfide on WSe$_{1.51}$/CNT to trap lithium ions from the electrolyte and complete the cathode reactions. As a result, even at sulfur loadings of 12.7 mg cm^{-2}, corresponding to an E/S ratio of 3.9 μL mg^{-1}, the areal capacity of S/WSe$_{1.51}$/CNT still

remained 7.7 mAh cm^{-2} after 150 cycles at 0.1C (Fig. 15b), indicating a moderate number of Se defects can improve the electrochemical performance of Li–S batteries. Chen's group designed CoSe with a hierarchical porous polyhedron structure (CS@HPP) as electrocatalyst for promoting the diffusion and conversion of LiPS [208]. The crystal quality and high number of active sites of CC@CS@HP accelerate the catalytic conversion of LiPS and deposition/decomposition of Li$_2$S, and batteries based on CC@CS@HPP sulfur as cathode achieve a high areal capacity under a lean electrolyte. Defective VSe$_2$ has also been studied as an electrocatalyst for lean electrolyte Li–S batteries. For example,

Liu's group built defective VSe$_2$-vertical graphene (VG) nanosheets on carbon cloth (denoted as VSe$_2$-VG@CC) as sulfur host for Li–S batteries [207]. As shown in Fig. 15c, it is a two-step conversion process. First, VG is produced on carbon cloth by plasma-enhanced chemical vapor deposition (PECVD) to get VG@CC. Then, by using VCl$_3$ and Se as precursors, VSe$_2$ nanosheets are grown on the VG@CC support to form VSe$_2$-VG heterostructures by van der Waals interactions. The SEM images of the material are shown in Fig. 15d–f. The VSe$_2$-VG@CC/S electrodes accelerate the adsorption and conversion of LiPS due to the presence of Se vacancies. Even under harsh operating conditions, such
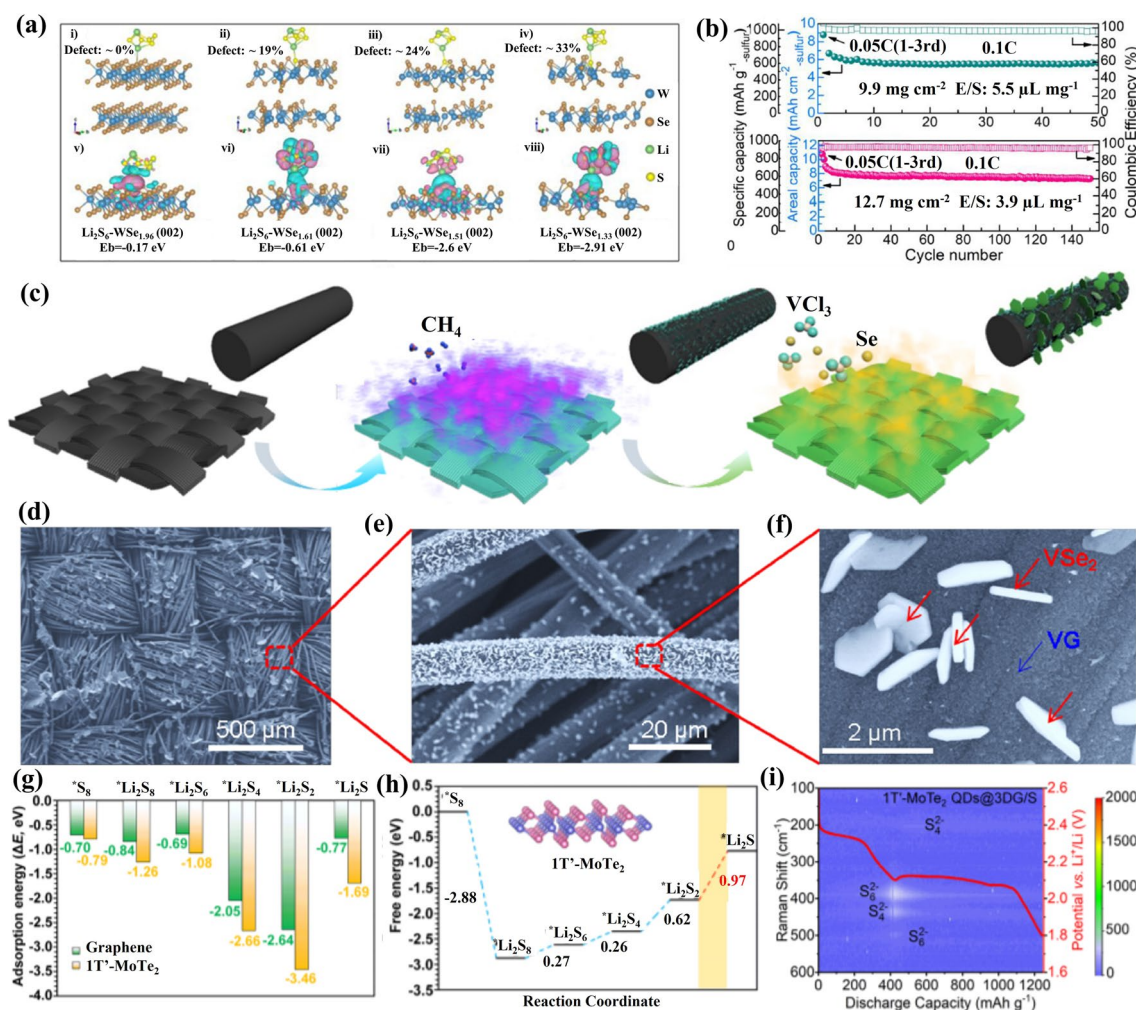

Fig. 15 **a** DFT calculations of stable configurations (i–iv) and charge transfers (v–viii), where the pink and cyan represent the spatial regions of increased and decreased charge density, respectively. **b** Cycling performance of the S/WSe$_{2-x}$/CNT cathodes with high sulfur loading and low E/S ratio [204]. Copyright 2022, Elsevier. **c** Schematic diagram of the synthetic process of VSe$_2$-VG heterostructure. **d**–**f** Successive magnified SEM images of the VSe$_2$-VG heterostructure on carbon cloth [207]. Copyright 2020, American Chemical Society. **g** Adsorption energy comparison between LiPS and 1T′-MoTe$_2$ monolayer or graphene. **h** Energy curves for the LiPS reaction on 1T′-MoTe$_2$ monolayer. **i** In situ XRD testing of the MoS$_2$ ND/porous carbon/Li$_2$S$_6$ electrode in the first two cycles [200]. Copyright 2021, American Chemical Society

as low E/S ratio (E/S = 4.8 μL mg^{-1}) and high sulfur loading (9.6 mg cm^{-2}), VSe$_2$-VG@CC/S electrodes can achieve an areal capacity of 4.9 mAh cm^{-2} at 0.2C after 40 cycles, which is significantly better than that of commercial Li-ion batteries. Recently, Chen's group systematically studied the phase transitions (2H, 1T and 1T′) of polar MoX$_2$ (X = S, Se and Te) and intrinsic mechanisms for Li–S batteries [200]. Their DFT calculations demonstrate that 1T′-MoTe$_2$ has a concentrated density of states (DOS) near the Fermi level, indicating high intrinsic conductivity. The authors also showed that 1T′-MoTe$_2$ has high stability. Based on the above analysis, 1T′-MoTe$_2$ quantum dots embedded in 3D graphene (MTQ@3DG) were used as electrocatalysts for Li–S batteries. As shown in Fig. 15g, the authors compared the adsorption energies of S$_8$ and LiPS on graphene and 1T′-MoTe$_2$, which were higher on 1T′-MoTe$_2$ than on graphene. In addition, the Gibbs free energy on graphene and 1T′-MoTe$_2$ was also evaluated (Fig. 15h). The Gibbs free energy of the rate-limiting step (Li$_2$S$_2$ to Li$_2$S) in graphene is 1.07 eV, while it is 0.97 eV in 1T′-MoTe$_2$. In situ Raman spectroscopy demonstrates that the shuttle effect of LiPS is suppressed in the MTQ@3DG/S cells due to the high electrocatalytic ability of 1T′-MoTe$_2$ (Fig. 15i). At a relatively low E/S ratio (E/S = 15), the MTQ@3DG/S cathode achieved a discharge capacity of 711.7 mAh g^{-1} after 600 cycles at 1C, with a capacity decay of 0.026% per cycle.

TMCls have been widely studied in lean electrolyte Li–S batteries due to their good electronic characteristics, band position and high number of active sites. Furthermore, metal sulfides have a strong sulfiphilic property for sulfur-containing substances, providing chemical anchoring capability for LiPS. After years of exploration, TMCls are one of the most effective anchors for suppressing the LiPS shuttle effect at low E/S ratios. However, most metal chalcogenides are less conductive than carbonaceous materials and tend to accumulate to form big particles, making it necessary to combine these two materials as cathodes. In addition, the electrocatalytic mechanism in Li–S batteries is not entirely understood. Therefore, more work should focus on the catalytic mechanism of metal sulfides in Li–S batteries.

2.5 Transition Metal Nitrides

Transition metal nitrides (TMNs) are another class of material displaying good electric conductivity, polar characteristics and chemical stability [228–231]. Nitrogen atoms are actually an excellent dopant within the carbon matrix because N contains one electron lone pair that can bond to metals to form a coordination center. In addition, the N atoms of TMNs can act as conductive Lewis bases to capture positively charged particles. Furthermore, the electronegativities of nitrogen and sulfur are almost equal enabling the formation of covalent bonds, thus reducing the shuttle effect of LiPS and improving the cycling stability of Li–S batteries [15]. A representative summary of TMN-based compounds for lean electrolyte Li–S performances is listed in Table 6. Titanium nitride (TiN) is the most used TMN in Li–S batteries. Because TiN and other TMNs agglomerate at high loads, leading to low electrochemical activity, they are generally supported on carbon-based materials [232]. For example, Mai's group designed a 3D nitrogen-doped graphene/TiN nanowires (3DNG/TiN) composite as LiPS anchor for Li–S cells at a relatively low E/S ratio [233]. The TiN nanowires were grown on graphene sheets to form a 3D interconnected network (3DNG/TiN) (Fig. 16a). The TEM image in Fig. 16b shows the rough surface of TiN nanowires with nanoscale pores. TEM elemental mapping showed the homogeneous distribution of Ti and N in a single TiN nanowire (Fig. 16c). The authors also evaluated the binding energy differences of NG, TiO$_2$ and TiN with long-chain Li$_2$S$_n$ (n = 4, 6, 8). DFT calculations demonstrate greater binding energies between LiPS and TiN, mainly due to the bonding between Li atoms of Li$_2$S$_n$ and N atoms of TiN, and S bonding of Li$_2$S$_n$ with both N and Ti atoms of TiN. Due to the high conductivity of the 3D porous graphene network and strong chemisorption LiPS on TiN nanowires, the 3DNG/TiN cathode with a high sulfur loading of 9.6 mg cm^{-2} and a relatively low E/S ratio of 10 delivered an ultrahigh areal capacity of 10 mAh cm^{-2} after 60 cycles at 0.5C.

Cobalt nitrides (Co$_4$N) have a robust binding capability to LiPS and catalytically promote the conversion of LiPS. Qiu's group fabricated Co$_4$N nanoparticles embedded in porous carbon nanosheet arrays grown onto carbon cloth (CC@Co$_4$N-PCNA) as a self-supported cathode [234]. Co content in CC@Co$_4$N-PCNA was about 7.00%. High-resolution TEM images of the CC@Co$_4$N-PCNA showed 0.207 nm lattice fringes due to the (111) plane of Co$_4$N (Fig. 16d) that displays the atomic structure of closely packed cobalt (Fig. 16e). The S/CC@Co$_4$N-PCNA electrodes showed stable cycling with a discharge capacity of 543 mAh g^{-1}

Table 6 Representative summary of TMNs for the performance of lean electrolyte Li–S batteries

| Cathode materials	S loading (mg cm^{-2})	S content (%)	Capacity (mAh g^{-1}/cm^{-2})	E/S ratio (μL mg^{-1})	Cycle life (cycle)	References
FCN111@S/GC	5.36	–	1029 mAh g^{-1} at 1.5 mA cm^{-2}	2.5	100	[119]
Co-NbN/rGO/S	5.6	72	3.92 mAh cm^{-2} at 0.1C	8	20	[228]
S/VNQD-HG	4	–	646 mAh g^{-1} at 0.2C	10	After 50	[229]
CC@Co$_4$N-PCNA	6.2	35.8	543 mAh g^{-1} at 0.5C	9	After 200	[234]
P-Fe$_4$N@NPG	5.65	73	6 mAh cm^{-2} at 0.1C	7	20	[235]
3DNG/TiN	5	–	1230 mAh g^{-1} at 0.1C	10	50	[233]
TiN-TiO$_2$/C/S	8	62–66	~4.3 mAh cm^{-2} at 0.2C	6.8	After 400	[114]
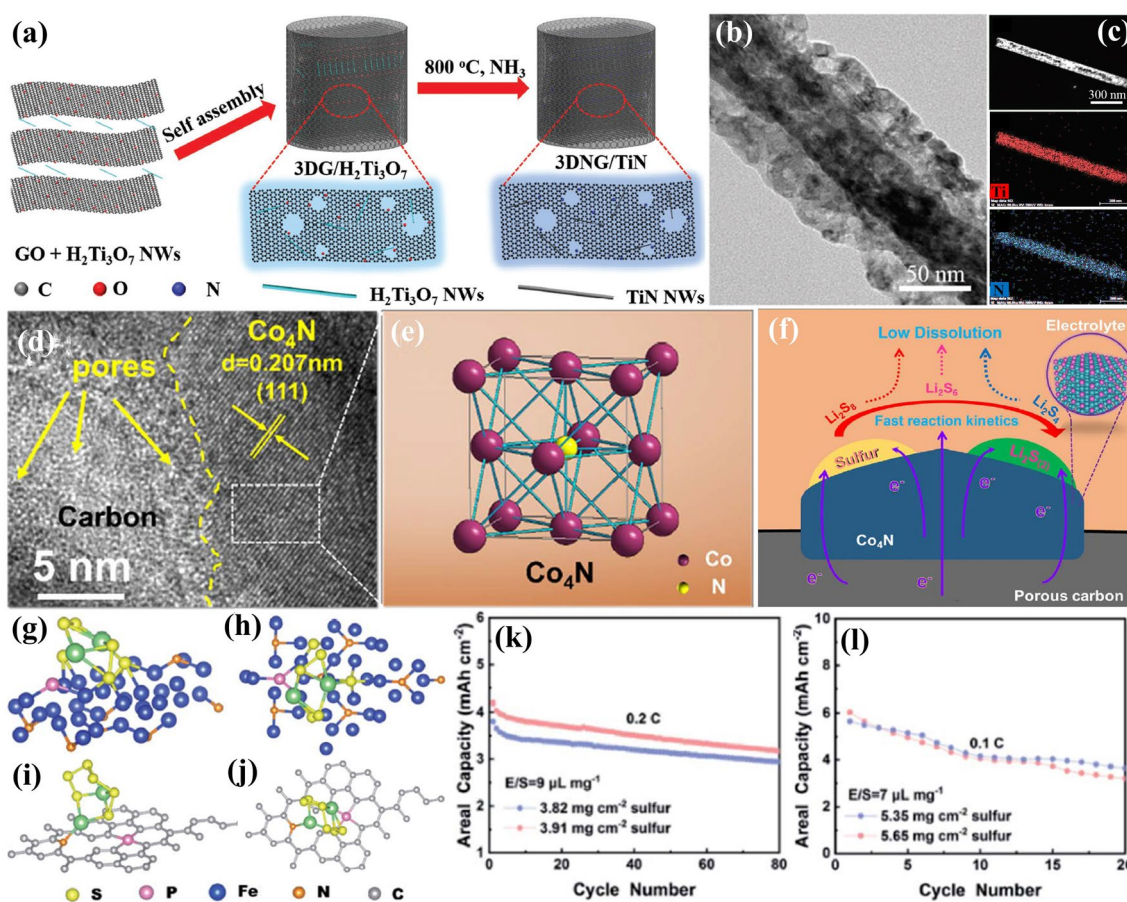
Fig. 16 a Schematic of the fabrication process of the 3DNG/TiN. **b** TEM image and **c** TEM elemental mapping image of 3DNG/TiN [233]. Copyright 2018, Wiley-VCH. **d** HR-TEM image of CC@Co$_4$N-PCNA. **e** Unit cell of Co$_4$N structures, **f** chemical absorption and catalytic effect of LiPS on the S/CC@Co$_4$N-PCNA cathode schematically [234]. Copyright 2019, Elsevier. **g**, **h** Different angles of the optimized geometry of Li$_2$S$_6$ on the Fe$_4$N (111) surface of P-Fe$_4$N. **i**, **j** Optimized geometry of Li$_2$S$_6$ on the NPG (002) surface at different angles. **k**, **l** Cycling performance of the P-Fe$_4$N@NPG/S cathode at 0.2C and 0.1C with lean electrolyte, respectively [235]. Copyright 2021, Royal Society of Chemistry

at 0.5C after 200 cycles at an E/S ratio of 9 and a sulfur loading of 6.2 mg cm^{-2}. The excellent electrochemical performance was ascribed to the following (Fig. 16f): (1) The

Co$_4$N nanoparticles embedded in porous carbon nanosheet arrays on carbon cloth favor the transport of Li$^+$ ions and electrons and help keep the structural integrity; (2) the

strongly polar Co_4N suppresses the polysulfide diffusion and reduces the shuttle effect; (3) the catalytic activity of Co_4N promotes the conversion of polysulfides. Other TMNs have also been studied. For example, Xu and co-workers designed phosphorus-modified Fe_4N supported by N, P co-doped graphene nanosheets (P-Fe_4N@NPG) as LiPS anchor [235]. DFT calculations were performed to evaluate the adsorption of LiPS on P-Fe_4N@NPG for LiPS (Fig. 16g–j). The adsorption energies of Li_2S_6 on P-Fe_4N@NPG and control sample NPG were -7.02 and -0.414 eV, respectively, suggesting that P-Fe_4N@NPG has a much stronger chemical adsorption ability toward LiPS compared to NPG. As a result, the P-Fe_4N@NPG/S cathode had an initial capacity of 4.19 mAh cm^{-2} under an E/S ratio of 9 μL mg^{-1} and a sulfur loading of 3.91 mg cm^{-2} at 0.2C (Fig. 16k). Even at a lower E/S ratio (7 μL mg^{-1}) and higher sulfur loading (5.65 mg cm^{-2}), the P-Fe_4N@NPG/S cathodes delivered an initial areal capacity of 6 mAh cm^{-2} at 0.1C, and it still maintained an areal capacity of 3.2 mAh cm^{-2} after 20 cycles (Fig. 16i). These results indicate the P-Fe_4N@NPG materials allow high sulfur utilization, inhibit the shuttle effect of LiPS and promote the redox kinetics of LiPS conversion.

Overall, although TMNs have achieved long cycle stability in Li–S batteries, most studies involving TMNs electrocatalysts in Li–S batteries have been assessed with excessive electrolyte. The electrocatalytic ability of TMNs under lean electrolyte conditions needs to be further investigated, which is essential for the design of effective electrocatalysts to improve the electrochemical performance of lean electrolyte cells.

2.6 Transition Metal Carbides and MXenes

Analogous to TMNs, transition metal carbides (TMCs) also possess high conductivity and have active sites that chemically anchor to LiPS [236]. These inherent properties make them suitable trapping materials for LiPS. Typical TMCs like Fe_3C, Co_3C and Mo_2C combined with carbon materials have been used as efficient sulfur hosts for lean electrolyte Li–S cells [237–240]. Within the family of 2D transition metal carbides and nitrides, MXenes have recently gained huge attention in numerous different fields accounting for their superior flexibility, outstanding mechanical strength, metallic conductivity, hydrophilic surfaces and large interlayer channels for ion diffusion. Table 7 summarizes recent

investigations on metal carbides and MXenes and their corresponding energy landscape in lean electrolyte Li–S batteries.

Bidirectional TMC-based electrocatalysts have been shown to facilitate the precipitation and decomposition of Li_2S. For example, Sun's team designed bidirectional Fe_3C@foam carbon/S-carbon fiber (Fe_3C@FC/S-CF) as electrocatalysts to enable the reactive Li_2S precipitation for Li–S batteries (Fig. 17a) [241]. The 3D porous framework reduces the pathways of Li^+ diffusion and electron transfer and exposes more active sites of Fe_3C nanoparticles. The bidirectional Fe_3C electrocatalysis with good catalytic properties accelerates the deposition and decomposition of Li_2S. To characterize the chemical interactions between Fe_3C@FC and sulfur species, XPS and XAFS were performed during the conversion process. Two characteristic peaks of Fe $2p_{3/2}$ located at 709.7 and 716.9 eV correspond to Fe^{2+} and Fe^{3+}. The peaks of Fe^{2+} and Fe^{3+} negative shift with increasing discharging depth owing to the electron transfer between Fe and LiPS, and this phenomenon indicates the formation of Fe-S bonds. The associated XPS shifts upward during subsequent charging, showing a reversible Fe valence change (Fig. 17b). The intensity ratio of the multiple structures of the L_3 edge of the Fe L-edge XANES spectrum is a fingerprint of Fe's different oxidation states (A_2/B_2), which decreases/increases gradually during discharge/charge, also proving the reversible reduction/oxidation of Fe in Fe_3C (Fig. 17c). Moreover, the Fe K-edge XANES spectra, as shown in Fig. 17d, further indicate valence changes of Fe. In agreement with the XPS results, this indicates that Fe_3C can trap LiPS and achieve a reversible transformation between LiPS and Li_2S. The corresponding FT-EXAFS spectra show that the Fe–C distance of Fe_3C widens and narrows from 1.5 to 1.7 Å during cycling due to the breathing behavior caused by the valence change of Fe (Fig. 17e). The reversible behavior was observed even after 50 cycles, which suggests that Fe_3C retains high catalytic activity during cycling (Fig. 17f, g). As a result, the Fe_3C@FC/S-CF cells achieved an initial areal capacity of 15.2 mAh cm^{-2} under high sulfur loading (16.1 mg cm^{-2}) and relatively low E/S ratio (8 μL mg^{-1}) and still maintained 10 mAh cm^{-2} after 70 cycles. Recently, Zhang's group also proposed a dual-directional catalyst (Co_3C@PNGr-CNT) as sulfur hosts for bidirectionally catalytic polysulfide conversion (Fig. 17h) [242]. The Co_3C@PNGr-CNT composites accelerated the deposition and decomposition of Li_2S, which can be demonstrated by

Table 7 Representative summary of TMCs and MXenes for the performance of lean electrolyte Li–S batteries

Cathode materials	S loading (mg cm^{-2})	S content (%)	Capacity (mAh g^{-1}/cm^{-2})	E/S ratio (μL mg^{-1})	Cycle life (cycle)	References
Fe$_3$C@FC/S-CF	16.1	60	15.2 mAh cm^{-2} at 0.05C	8	70	[241]
Co$_3$C@PNGr-CNT/S	15.6	81	12.33 mAh cm^{-2} at 0.05C	8	40	[242]
Mo$_2$C@PCN/S	–	72	~450 mAh g^{-1} at 0.1 A g^{-1}	10	After 15	[238]
TiC/CNFs@Li$_2$S$_6$	~4.2	66.7–70.4	889 mAh g^{-1} at 0.2C	15	110	[243]
VC@NCNTs/S	3.6	71.66	~600 mAh g^{-1} at 0.5C	7	100	[244]
Mo$_2$C/CHS	5	70	904 mAh g^{-1} at 0.5C	7	200	[236]
S/3De-Ti$_3$C$_2$-2 MXene	6.1	74.7	~5.6 mAh cm^{-2} at 0.1C	5.2	200	[245]
KB/S@Ti$_3$C$_2$T$_x$ MXene	5.6	60	810 mAh g^{-1} at 0.2C	7	100	[246]
IS-MGN@S MXene	4	–	1213 mAh g^{-1} at 0.2C	4.8	50	[247]
T@CP-S MXene	–	70.2	920 mAh g^{-1} at 0.2C	5	60	[248]
S/3De-Ti$_3$C$_2$-2 MXene	6.1	74.7	~3 mAh cm^{-2} at 0.1C	5.2	After 200	[245]

the decreased activation energy of the reduction and oxidation processes (Fig. 17i). As a result, Li–S batteries based on Co$_3$C@PNGr-CNT composites enabled a high areal capacity of 11. mAh cm^{-2} after 40 cycles, even with a high sulfur loading of 15.6 mg cm^{-2} and an E/S ratio of 5 (Fig. 17j). These bidirectional catalysts provide new perspectives for the development of high-performance Li–S batteries. Recently, nanosized Mo$_2$C electrocatalysts embedded in a porous carbon network (Mo$_2$C@PCN) were fabricated by a pyrolysis method (Fig. 17k) [249]. The high conductivity and catalytic property of Mo$_2$C@PCN/S, enabled Li–S cells with a specific discharge capacity of ~450 mAh g^{-1} at 0.1 A g^{-1} after 15 cycles under an E/S ratio of 5. Shen et al. reported a titanium carbide-modified carbon nanofibers (TiC/CNFs) electrocatalytic membrane for Li–S cells (Fig. 17l) [243]. Figure 17m shows the SEM image of TiC/CNFs, showing TiC nanoparticles on the surface of CNFs with internal cross-linking morphology, which offers fast channels for electron transfer and lithium-ion diffusion. In addition, the UV/Vis measurements reveal that the absorption ability of Li$_2$S$_6$ by TiC/CNFs is much higher compared to CNFs and TiC, suggesting that TiC/CNFs efficiently bind LiPS (Fig. 17n). The obtained TiC/CNFs electrode exhibits good cycling performances.

MXene, a new class of two-dimensional nanomaterials with hydrophilic surfaces and metallic conductivity, has received significant attention since it was first reported by Gogotsi's group [248, 250–256]. For example, Zhang and co-workers applied MXene (Ti$_3$C$_2$T$_x$) nanosheets as both cathode, interlayer and modified separator to achieve a long cycle life Li–S batteries with a long cycle life (Fig. 18a) [246]. As shown in Fig. 18b, the interwoven KB@Ti$_3$C$_2$Tx composite was constructed by self-assembly of the intrinsic negatively charged Ti$_3$C$_2$T$_x$ nanosheets and positively charged Ketjen black/sulfur (KB/S). The structure of KB/S@Ti$_3$C$_2$T$_x$ offers multiple advantages, such as allowing high sulfur content and buffering volume expansion while maintaining good structural integrity and ionic and conductive channels. As a result, the cells achieved a discharge capacity of 810 mAh g^{-1} at 0.2C under sulfur loading of 5.6 mg cm^{-2} and a relatively lean electrolyte of E/S ratio of 7 μL mg^{-1}, with a capacity of about 600 mAh g^{-1} after 100 cycles. The aggregation of sulfur causes the low utilization of active materials. Hence, Zhou's group proposed in situ growth of ultrathin sulfur microcrystals on MXene-based 3D matrices for soft-packaged flexible Li–S batteries [247]. The authors developed an advanced IS-MGN@S electrode by associating the microscale sulfur microcrystal evolution during liquid-phase synthesis and controlling
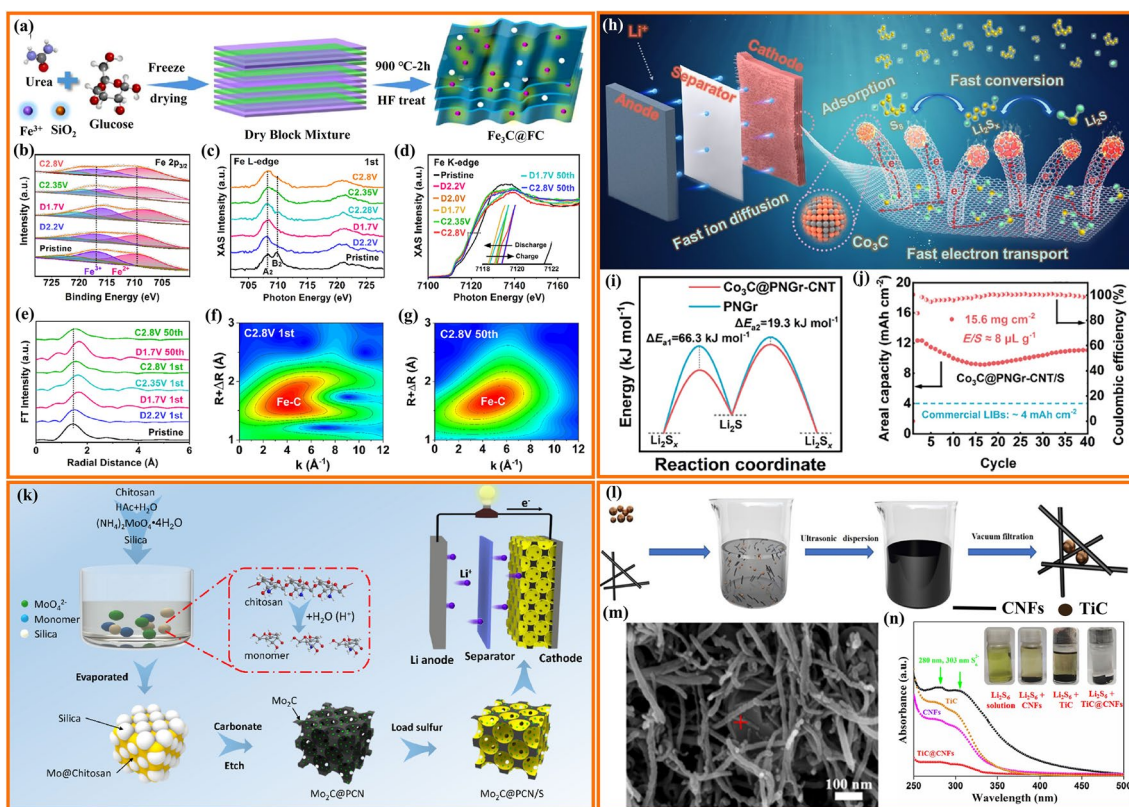
Fig. 17 a Diagram of the synthesis of Fe$_3$C@FC composites. **b** Fe 2$p_{3/2}$ XPS spectra. **c** Fe L-edge XANES spectra. **d** Fe K-edge XANES spectrum and **e** corresponding FT-EXAFS spectra of Fe$_3$C@FC/S-CF at different states of charge. WT transform contour plots of Fe K-edge after **f** 1 cycle and **g** 50 cycles [241]. Copyright 2022, Elsevier. **h** Schematic diagram of the Co$_3$C@PNGr-CNT bidirectional catalytic conversion of LiPS. **i** The activation energy (E_a) of the deposition and decomposition of Li$_2$S. **j** Cycling performance of Co$_3$C@PNGr-CNT/S cathode with a high-sulfur loading and a relatively low E/S ratio [242]. Copyright 2022, Elsevier. **k** Illustration of the fabrication of the Mo$_2$C@PCN/S [249] Copyright 2022, Elsevier. **l** Schematic illustration for the fabrication of TiC/CNFs. **m** SEM image of TiC/CNFs. **n** UV–Vis spectra and digital photographs (inset) of Li$_2$S$_6$ solution before and after adding CNFs, TiC and TiC/CNFs [243]. Copyright 2022, Springer Nature

sulfur microcrystal growth on the MXene-graphene-cellulose nanofiber (MGN) matrix (Fig. 18c). Ultrathin sulfur microcrystals consist of a few layers of sulfur atoms, so it is easier to realize improved kinetics than with bulk sulfur. The batteries based on IS-MGN@S cathodes show excellent electrochemical performance, which a capacity of 1213 mAh g^{-1} at 0.2C for a sulfur loading (~ 4 mg cm^{-2}) and lean electrolyte content (E/S ratio: 4.8 μL mg^{-1}). Chen's team applied hierarchically porous Ti$_3$C$_2$ MXene as a sulfur host with desirable properties such as: (1) interlinked backbones provide homogeneous sulfur distribution and avoid restacking of MXene sheets, (2) the high number of active sites and modulation of the d-band center of Ti atoms result in strong LiPS adsorption, (3) unsaturated coordinated Ti on edge sites effectively anchor LiPS, reduce Li$^+$ diffusion barriers and accelerate redox kinetics of LiPS [245]. As shown

in Fig. 18g, the authors synthesized the hierarchically porous Ti$_3$C$_2$ MXene with abundant edge sites using PMMA as a template. The authors controlled the number of edges by adjusting the temperature of the spray drying process with a fixed etching time. Figure 18h-j displays the sample morphological changes by changing the spray drying temperature. At a spray drying temperature of 120 °C, a limited number of pores are generated on the HF-etched nanosheets (3D e-Ti$_3$C$_2$-1). As the temperature is increased to 150 °C, more mesopores are produced, exposing a high number of active edges (3D e-Ti$_3$C$_2$-2). Multiple large pores are formed when the temperature is increased to 180 °C (3D e-Ti$_3$C$_2$-3), which disrupts the 3D Ti$_3$C$_2$ spherical morphology. The micro/mesoporous structure 3D e-Ti$_3$C$_2$-2 with a high number of edges allows for shortened ion diffusion paths and abundant surface-active sites, which accelerates electrochemical
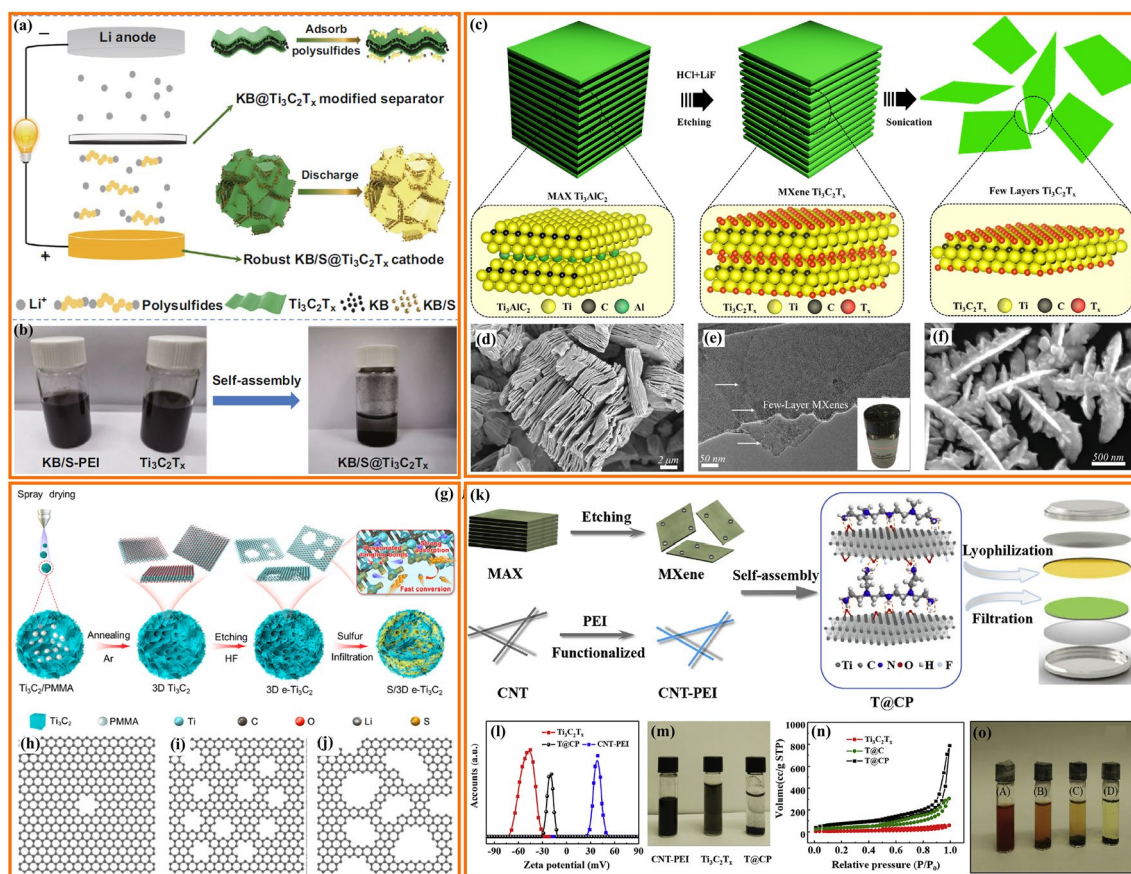
Fig. 18 a Illustration of the interaction of interwoven KB@$Ti_3C_2T_x$ with LiPS. **b** Optical images of KB/S-PEI, $Ti_3C_2T_x$ and KB/S@$Ti_3C_2T_x$ in an aqueous suspension [246]. Copyright 2020, Springer Nature. **c** Diagram of the synthesis process of the few layers $Ti_3C_2T_x$. **d** SEM image of $Ti_3C_2T_x$. **e** TEM image of $Ti_3C_2T_x$. **f** SEM image of the IS-MGN@S [247]. Copyright 2022, Wiley-VCH. **g** Synthesis schematic of S/3D e-Ti_3C_2 microspheres. Morphological evolution diagrams of **h** 3D e-Ti_3C_{2-1} (120 °C). **i** 3D e-Ti_3C_{2-2} (150 °C) and **j** 3D e-Ti_3C_{2-3} (180 °C) [245]. Copyright 2021, American Chemical Society. **k** Schematic diagram of the synthesis of T@CP nanohybrids. **l** Zeta potential of $Ti_3C_2T_x$ nanosheet, CNT-PEI and T@CP composites. **m** Optical images of CNT-PEI aqueous suspension, $Ti_3C_2T_x$ and T@CP. **n** N_2 adsorption–desorption isotherms of $Ti_3C_2T_x$, T@C and T@CP composites. **o** Optical images of the Li_2S_x solution before (A) and after adding CNT-PEI (B), $Ti_3C_2T_x$ (C) and T@CP (D) for 6 h [248]. Copyright 2019, Elsevier

kinetics. Li–S cells based on S/3D e-Ti_3C_2-2 cathode deliver a capacity of 5.6 mAh cm^{-2} at 0.1C with a sulfur loading of 6.1 mg cm^{-2} and a low E/S ratio of 5.2 μL mg^{-1}. This result demonstrates the importance of edge engineering of 2D layered materials for improving electrochemical performance. In 2019, Guo and co-workers designed an advanced strategy through electrostatic self-assembly of MXene ($Ti_3C_2T_x$) with polyethyleneimine (PEI)-functionalized CNT for dendrite-inhibited Li–S batteries [248]. Figure 18k illustrates the synthesis process of the $Ti_3C_2T_x$@CNTPEI (T@CP) composite. As displayed in Fig. 18l, the $Ti_3C_2T_x$ nanosheets are highly negatively charged with a zeta potential of −48 mV due to the presence of several functional groups (e.g., –O,

–OH and –F). As shown in Fig. 18m, $Ti_3C_2T_x$ forms stable aqueous solutions. A clear supernatant was observed after adding $Ti_3C_2T_x$ solution to the CNT-PEI solution, suggesting that CNT-PEI spontaneously adhered to the nanosheet surface and successfully self-assembled. The specific surface area of the T@CP composite was as high as 268 m^2 g^{-1} compared with $Ti_3C_2T_x$ (26 m^2 g^{-1}) and T@C (165 m^2 g^{-1}) composite (Fig. 18n). The T@CP composite shows a highly porous structure with pore sizes in the range of 10–80 nm. In contrast, the stacked $Ti_3C_2T_x$ lacks pores in this size range. These results suggest that MXene, CNT and PEI all contribute to the assembly process. To investigate the ability of these materials to absorb LiPS, CNT-PEI (B), $Ti_3C_2T_x$ (C)

and T@CP (D) were added into equal amounts of Li_2S_x solution (A). As shown in Fig. 18o, the color of Li_2S_x solution after the addition of T@CP was much lighter than CNT-PEI or bare-MXene, indicating T@CP has a strong chemisorption capacity for LiPS. The Li–S batteries based on T@CP as cathode were assembled under lean electrolyte conditions to explore its practical application. The cell achieves a capacity of 920 mAh g^{-1} at an E/S ratio of 5 mL g^{-1}.

In general, TMCs have the potential for lean electrolyte Li–S batteries due to their polarity and high electric conductivity. However, the use of TMCs as host materials is still in the early research stage due to the harsh conditions required for their synthesis. Therefore, there is still a need to develop simple synthetic approaches to prepare TMCs with tailored morphologies.

2.7 Metal–Organic Frameworks

Metal–organic frameworks (MOFs) are a relatively new class of crystalline porous materials consisting of metal ions or metal clusters coordinated by organic linkers [257–259]. MOFs are of interest for energy storage, gas separation and catalysis due to their functionalized and tailorable structures [260–269]. Recent studies have indicated that the MOFs can be used as promising cathode materials in lean electrolyte Li–S cells due to their highly porous framework, high number of functional groups and Lewis acid sites [63, 270]. A summary of MOFs compounds and their properties in the Li–S performance is depicted in Table 8.

In 2020, Knibbe's group demonstrated that Lewis acid–base interactions between MOFs and LiPS are beneficial to improving the electrochemical performance of Li–S batteries [271]. In this work, they combined dimethylammonium zinc formate (DMAZF) MOF with CNTs as a molecular sieve to mitigate LiPS migration (Fig. 19a–c). This MOF can act as a molecular sieve that inhibits the migration of LiPS while allowing the diffusion of Li$^+$ (Fig. 19d). The authors compared the different morphologies of the Li anode of DMAZF/CNTs/sulfur, Br-UIO-66/CNTs/sulfur and UIO-66/CNTs/sulfur after cycling (Fig. 19e–h). Compared with the Li anodes of Br-UIO-66 (Fig. 19g) and UIO-66 (Fig. 19h), the lithium anode of DMAZF (Fig. 19f) is still relatively smooth. This indicates that DMAZF inhibits the LiPS shuttle better than Br-66 and UIO-66. Owing to this novel nanoporous structure, the DMAZF/CNTs/

sulfur composite cathode with a sulfur loading (5 mg cm^{-2}) showed a sustainable capacity of 1007 mAh g^{-1} at 0.1C under a low E/S (6 µL mg^{-1}).

Besides the interactions between MOFs and LiPS, Huang's group investigated the effect of sulfur copolymerization with vinyl-functionalized MOF on the performance of Li–S batteries [258]. A MOF-sulfur copolymer (CNT@UiO-66-V-S) was designed as shown in Fig. 19i, in which sulfur chains were copolymerized with vinyl-functionalized MOF (UiO-66-V) at 200 ℃. For comparison, the traditional MOF/S composites (CNT@UiO-66-V/S) were obtained by heat-treating at 155 °C for 12 h. In situ Raman spectroscopy was applied to monitor the real-time transformation processes of LiPS during the first discharge cycle at 0.2C (Fig. 19j-m). A very slow conversion process was observed for the Li–S cells with the traditional UiO-66-V/S electrode (Fig. 19j, k). However, the Li–S cells with the UiO-66-V-S cathode in Fig. 19l, m show a different reaction process. During the discharge process, in situ Raman spectroscopy measurements showed the gradual intercalation process from Li_2S_8 to Li_2S_2. During charging, all the phase changes are reversible. These results indicate that UiO-66-V-S cathode facilitates the conversion of LiPS to Li_2S_2 and reduces the LiPS retention time compared to the traditional conversion pathways in UiO-66-V/S. As a result, such a copolymerization strategy can provide long-term stable cycling performance at a relatively low E/S ratio (10 µL mg^{-1}). In addition to conventional insulating MOFs, Wang and his colleagues synthesized conductive MOFs to facilitate the conversion of LiPS [272]. In this work, a conductive Ni-HHTP (HHTP = 2,3,6,7,10,11-hexahydroxytriphenylene) MOF grown on carbon paper is proposed to promote the transformation of LiPS. Ni-HHTP was prepared by the reaction of nickel acetate (Ni(OAc)$_2$) and p-conjugated 2,3,6,7,10,11-hexahydroxytriphenyl (HHTP) under solvothermal conditions (Fig. 19n). To show the superiority of conductive Ni-HHTP, the authors used insulating Ni-1,3,5-benzenetricarboxylic acid (Ni-BTC) as a control sample for comparison. Besides the superb electronic conductivity, Ni-HHTP also has strong chemical adsorption to LiPS. As shown in Fig. 19o, Ni-HHTP decolorized the LiPS solution after 6 h, while the LiPS solution with Ni-BTC still had a yellow color. Thanks to the porous structure and high conductivity, the Ni-HHTP@CP cathode exhibited excellent performance at a high sulfur loading (5.4 mg cm^{-2}) and decreased electrolyte dosage (E/S = 6.5 µL mg^{-1}). Besides

Table 8 Summary of MOFs, SAs catalysts and other transition metal compounds for the performance of lean electrolyte Li–S batteries

Cathode materials	S loading (mg cm^{-2})	S content (%)	Capacity (mAh g^{-1}/cm^{-2})	E/S ratio (μL mg^{-1})	Cycle life (cycle)	References
D-UiO-66-NH$_2$-4/G MOFs	12.2	89	13 mAh g^{-1} at 0.1C	5	65	[257]
DMAZF/CNTs/sulfur MOFs	5	70	1007 mAh g^{-1} at 0.1C	6	120	[271]
Ni-HHTP@CP MOFs	5.38	–	4.46 mAh cm^{-2} at 0.05C	6.5	25	[272]
CNT@UiO-66-V-S MOFs	5.6	71.4	4.25 mAh cm^{-2} at 0.2C	10	100	[258]
Co–N–C SAC/S single atoms	6	–	825 mAh g^{-1} at 0.1C	4	After 100	[273]
S@Fe–N/MHCS single atoms	5.4	80	6.42 mAh cm^{-2} at 0.1C	8	100	[113]
FeNC/wG single atoms	5.39	–	4.18 mAh cm^{-2} at 0.5C	7.8	50	[101]
S@Co/SA-Zn@N C/CNTs single atoms	5.1	70.7	4.5 mAh cm^{-2} at 0.2C	8	After 100	[274]
SA-Cu@NCNF single atoms	10	66.5	608.8 mAh g^{-1} at 0.2C	6	After 50	[275]
Fe-N$_3$C$_2$-C single atoms	6.6	–	6.7 mAh cm^{-2} at 0.1C	8	50	[276]
S@Mn/C-(N, O) single atoms	1.1	76	1330 mAh g^{-1} at 0.2C	–	400	[277]
NbB$_2$/NPG/S	16.5	75	1030 mAh g^{-1} at 0.1C	6	40	[278]
ZrB$_2$/NG/S	8.03	72	8.08 mAh cm^{-2} at 0.1C	8	40	[279]
ZrB$_2$/NG/S	4.8	72	1044 mAh g^{-1} at 0.1C	8	132	[279]
G-MgB$_2$	9.3	60	$\approx$ 850 mAh g^{-1} at 0.1C	6.5	100	[280]
FeF$_2$@rGO/S	12.7	–	12.3 mAh cm^{-2} at 0.1C	6	50	[281]
Nickel-foam@carbon-shell	40	–	41 mAh cm^{-2} at 0.2C	7	100	[282]

the typical MOFs discussed above, our group demonstrated that cationic MOF-based Cu-Mo bimetallic doped carbon nanofibers (Cu-Mo@NPCN) can effectively catalyze the conversion of LiPS. Since the coordination valence state of Cu and Mo improves the electrical conductivity and the catalytic activity, while the intertwined network enhances the Li$^+$ diffusion and suppresses the volume change of the electrode, the high sulfur-loaded Li–S cells based on Cu-Mo@NPCN/S cathodes exhibit high areal capacity and good cycling performance, suggesting its great potential for practical applications.

MOFs have coordinated metal ions and porous structures; they can strongly bind to LiPS. However, most of the MOFs have low electronic conductivity, which results in low utilization of sulfur species. In addition, the presence of open metal centers as Lewis acid sites and the pore size tuning of MOFs to optimize sulfur utilization are the focus of current research, but the interaction mechanism between MOFs and LiPS needs to be investigated in more detail.

2.8 Single Atoms

Recent years have seen the development of numerous single-atoms (SAs) catalysts (Fe, Co, Ni, Mo, W, Cu, etc.) that exhibit superior activity for a variety of chemical

reactions [106, 136, 277, 283–285]. These catalysts have become available through a variety of cutting-edge atomic-scale techniques, including synthetic methods, theoretical calculations and characterization tools. SA catalysts maximize the dispersion of the active metal phase. Besides maximizing metal utilization, SA catalysts with uncoordinated bonds provide strong chemisorption and excellent catalytic activity in Li–S batteries, promoting LiPS conversion and well-controlled Li$_2$S deposition sites with low E/S ratio [142, 276, 286]. Table 8 shows a summary of SAs catalyst and their properties for the performance of lean electrolyte Li–S batteries.

Han et al. applied DFT calculations to explore the catalytic activity of nine types of 3d SAs metal catalysts (Cu, Ni, Co, Fe, Mn, Cr, V, Ti, Sc) [287]. By analyzing the d-p orbital hybridization between metal atoms and S species, they discovered that single-atom-Ti (SATi) exhibits strong d-p hybridization and forms more robust bonds with LiPS, as Ti has slightly filled anti-bonding states. The more efficient d-p orbital hybridization in the SATi-S bond lowers the energy barriers of LiPS reduction/Li$_2$S oxidation. As a result, the Li–S cells based on SATi as sulfur hosts achieved a high electrochemical specific capacity. However, these electrochemical results were evaluated under flood electrolyte conditions. Chen's group prepared highly active SA
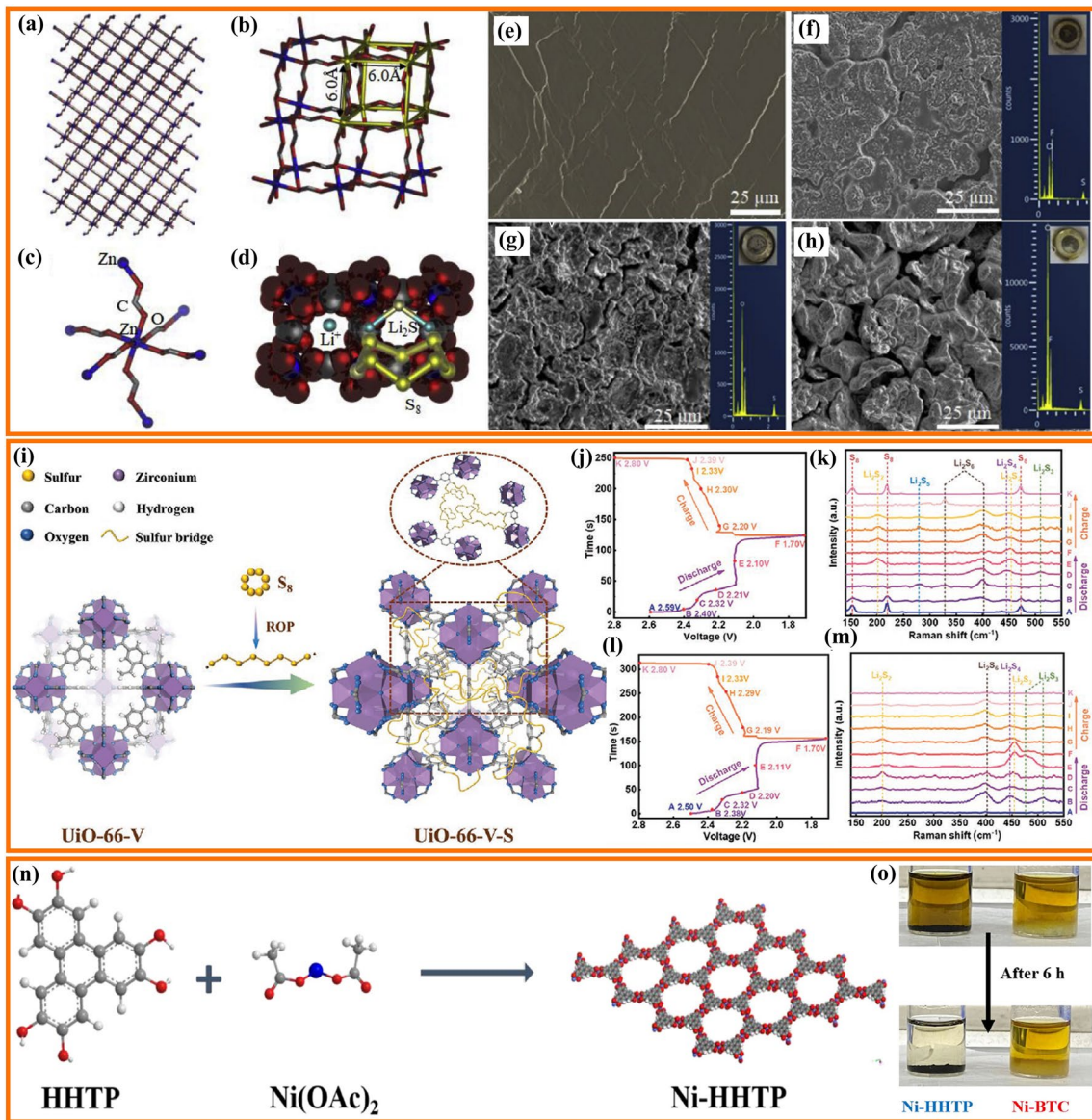
Fig. 19 Crystal structure representation of the 3D network DMAZF, where **a** crystal structure packing. **b** Size of the network window into the void space. **c** Metal node displaying the carbon and oxygen coordination to Zn. **d** Description of the LiPS mitigation process and the entry of Li ions through the nanopores. **e** Surface morphology of the uncycled anode of DMAZF/CNTs/sulfur electrode. **f** Cycled anode in the presence of DMAZF/CNTs/sulfur electrode. The surface morphology of the cycled anode **g** Br-UIO-66/CNTs/sulfur electrode and **h** UIO-66/CNTs/sulfur electrode [271]. Copyright 2020, Elsevier. **i** Schematic diagram of the preparation of UiO-66-V/S. **j** Voltage–time curves of UiO-66-V/S cathode. **k** In situ Raman spectra of UiO-66-V/S cathode. **l** Voltage–time curves of UiO-66-V-S cathode. **m** In situ Raman spectra of UiO-66-V-S cathode [258]. Copyright 2022, Wiley-VCH. **n** Schematic illustration of the fabrication of Ni-HHTP. **o** Polysulfides adsorption experiment of Ni-HHTP and Ni-BTC [272]. Copyright 2021, Elsevier

iron@graphitic carbon nitride catalytic materials (SAFe@g-C_3N_4) to find the balance between low E/S ratio and high electrochemical performance (Fig. 20a) [283]. The atomic ratio of N and Fe elements in SAFe@g-C_3N_4 was estimated to be 54.17 and 0.73%. The nitrogen sites in the g-C_3N_4 structure allow for more SAs loading and suppress the shuttle effect of LiPS during the charge–discharge process. The Li–S cells based on SAFe@g-C_3N_4 show superior cycling

stability and maintain a capacity of 90% after 200 cycles at 0.2C. Other SAs catalysts also show outstanding performance at low E/S ratio. For example, Wang et al. reported a novel template-free folic acid self-assembly strategy for the simple preparation of ultrathin N-doped carbon nanosheets confined to single-metal-atom catalysts [273]. Co–N–C single-metal-catalysts as sulfur hosts could achieve long-term stability with a low E/S ratio of 4 μL mg^{-1}and a high sulfur loading of 6 mg cm^{-2}.

Morphology also plays an important role in the electrochemical properties of SAs. Kim et al. described the morphological engineering of a graphene support to modify the local coordination structure of FeN$_4$ moieties (Fig. 20c, d) [101]. Compared to FeN$_4$ sites on planar graphene substrates

(G), FeN$_4$ active sites supported on a highly wrinkled graphene (wG) matrix (FeNC/wG) induced the modification of the local structure of Fe, thereby promoting the conversion reaction kinetics of LiPS. The relative content of Fe in FeNC/wG was estimated to be 0.78 wt%. Due to the beneficial interaction between the atomically modified FeN$_4$ active sites and the morphological engineering of graphene support, the Fe–N–C-based Li–S batteries showed excellent cycling stability with low electrolyte usage. The morphology of Li$_2$S deposition has a significant impact on the deposition capacity of Li$_2$S. Li's group proposed that nitrogen-doped carbon fibers decorated with SA Cu change the Li$_2$S deposition morphology from the traditional 2D lateral morphology to 3D spherical clusters by consecutive 3D nucleation
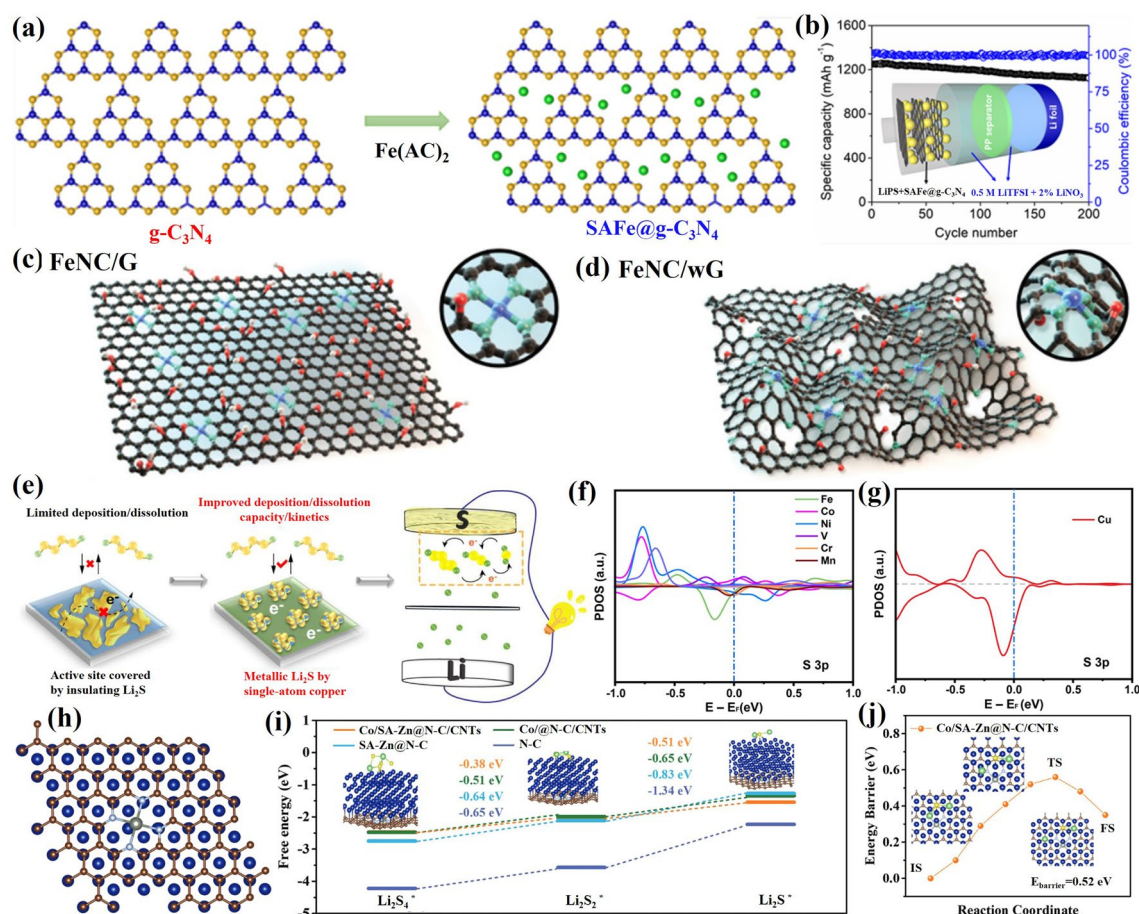

Fig. 20 a Synthesis process of SAFe@g-C$_3$N$_4$. **b** The corresponding electrochemical performance of SAFe@g-C$_3$N$_4$-based Li–S cell [283]. Copyright 2020, American Chemical Society. Schematic diagram of FeNx sites on **c** planar graphene (FeNC/G) and **d** wG (FeNC/wG [101]. Copyright 2022, Wiley-VCH. **e** Schematic representation of Li$_2$S precipitation/decomposition on SA-Cu@NCNF. PDOS of S 2*p* in **f** SATM@ NG/Li$_2$S (TM=Fe, Co, Ni, V, Cr, Mn) and **g** SA-Cu@NG/Li2S [275]. Copyright 2022, Elsevier. **h** Top view of the optimized configurations of Co/SA-Zn@N-C/CNTs. **i** Energy profiles for LiPS reduction on Co/SA-Zn@N-C/CNTs, Co@N-C/CNTs, SA-Zn@N-C and N-C. **j** Energy profile of Li$_2$S delithiation on Co/SA-Zn@N-C/CNTs [274]. Copyright 2022, Wiley-VCH

and growth (Fig. 20e) [275]. The atomic ratios of N and Cu were around 3.03 and 0.25%, respectively. The authors first performed DFT calculations to fully explore the electronic characteristics of Li_2S on several SAs catalysts with TM-N_4@C structure. Li_2S exhibits a half-metallicity (metallicity in one electron spin direction) on SA-Fe, Co, Ni, V, Cr and Mn (Fig. 20f). However, Li_2S adsorbed on SA-Cu is two-electron spin orientated and shows metallicity, with the highest electron density of states (DOS) around the Fermi energy level (E_F), thus significantly increasing the electronic conductivity of the Li_2S molecule (Fig. 20g). As a result, the precipitation capacity of Li_2S and the effectiveness of Li_2S-covered catalytic sites are enhanced. Most current work for SAs systems has focused on generating high densities of individual single metal atoms and avoiding the formation of metal-containing nanoparticles. Wang et al. embedded both Co nanoparticles and single-atom Zn into nitrogen-doped porous carbon nanosheet-grafted CNTs (denoted as Co/SA-Zn@N–C/CNTs) as electrocatalysts for Li–S batteries [274]. The Co and Zn contents in the Co/SA-Zn@N–C were around 4.32 and 0.94 wt%, respectively. In addition, N-doped carbon nanosheets (N–C), N-doped carbon nanosheets embedded with Zn single atoms (SA-Zn@N–C), and N-doped carbon/CNTs embedded with Co particles (Co@N–C/CNTs) were also prepared for comparison. DFT calculations were performed to gain insight into the catalytic mechanism of the LiPS conversion with Co/SA-Zn@N–C/CNTs. Figure 20h shows the optimized configuration of the Co/SA-Zn@N–C/CNTs. Figure 20i presents the Gibbs free energy diagrams for the conversion reactions on these four materials. The lowest Gibbs free energy for the rate-limiting step is found in the integrated Co/SA-Zn@N–C/CNTs, indicating that the co-existence of single Zn atoms and Co nanoparticles significantly lowers the energy barrier for the solid–solid Li_2S_2-Li_2S conversion reaction. The authors also investigated the dissociation ability of Li_2S on the four configurations during the charging process (Fig. 20j). The energy profiles of Li_2S dissociation also showed that the energy barrier for decomposition was lower on Co/SA-Zn@N–C/CNTs (0.52 eV) than on N–C (1.61 eV), SA-Zn@N–C (1.31 eV) and Co@N–C/CNTs (0.77 eV), indicating that the SA-Zn sites and Co sites could co-operate to speed up the delithiation of Li_2S. This work proposed coupled Co nanoparticles and SA-Zn moieties with an optimal charge redistribution to catalyze the LiPS conversion reactions.

Overall, SAs catalysts hold great potential for use in Li–S batteries due to their high atom utilization efficiency, strong catalytic activity and the ability to adjust their structure at the atomic level. Although SAs catalysts offer the above-mentioned advantages, the development of large-scale synthesis strategies which allow increased loadings is crucial for their application in lean electrolyte Li–S batteries.

2.9 Other Transition Metal Compounds

In addition to the previously mentioned transition metal-based systems, the applications of transition metal borides, transition metal fluorides and nickel foam in lean electrolyte Li–S batteries are also discussed in this section. Table 8 summarizes recent investigations on these compounds and their corresponding energy landscape in Li–S batteries.

Transition metal borides have recently been applied as sulfur hosts for lean electrolyte Li–S batteries due to their high metallic conductivity [288–290]. Unlike other polar metal compounds, boron (B) has an electronic structure with empty orbitals that can trap LiPS by forming B-S bonds. Hence, both the metal and B can chemisorb LiPS to suppress the shuttle effect [280, 288, 291]. In 2018, Xu's group first reported the use of titanium diboride (TiB_2) as a sulfur host [292]. In 2022, Xu's group designed niobium diboride (NbB_2) nanoparticles with high conductivity and catalytic activity toward LiPS conversion for Li–S cells with low-electrolyte content [278]. Figure 21a shows the mechanism of NbB_2 nanoparticles facilitating LiPS transformation and Li_2S 3D-nucleation: (1) NbB_2 nanoparticles with high electrical conductivity and a high number of catalytic active sites facilitate the reaction kinetics of LiPS; (2) nano-sized NbB_2 exposes more catalytic sites for the conversion of LiPS; (3) both metal Nb and B can chemisorb LiPS and direct Li_2S nucleation. Nitrogen-phosphorus co-doped graphene (NPG) composites were utilized as comparison samples. The authors used SEM to illustrate the effect of different host interfaces on the precipitation morphology of Li_2S to reveal the nucleation mechanism of Li_2S. As shown in Fig. 21b, d, Li_2S particles aggregated on the surface of the reference NPG. However, 3D "flower-like" Li_2S flakes are deposited on the surface of NbB_2, suggesting fast and uniform nucleation of Li_2S on the surface of NbB_2. In addition, EDS mapping also demonstrated that the coverage of Li_2S on the NbB_2 surface exceeds that of NPG (Fig. 21c, e). As a result,

the NbB$_2$/NPG/S composite showed an initial capacity of 1030 mAh g^{-1} and maintained 647 mAh g^{-1} after 40 cycles at 0.1C with a sulfur loading (16.5 mg cm^{-2}) and a low E/S ratio (6 μL mg^{-1}). Almost simultaneously, their group also proposed highly conductive zirconium boride (ZrB$_2$) nanoparticles as bidirectional catalysts for lean electrolyte Li–S batteries [279]. As shown in Fig. 21f, the partial density of states indicates that ZrB$_2$ is continuous at the Fermi level, proving its metallic nature. ZrB$_2$ is a hexagonal crystal system (Fig. 21g-j). The graphite-like structure of the B atomic layer structure and the outer electronic structure of Zr determine that ZrB$_2$ has good conductivity. Furthermore, the surface unsaturated coordination number of Zr atoms (Fig. 21k) leads to a high affinity of ZrB$_2$ for LiPS. In addition, the electron location function (ELF) indicates that the Zr atom has good metal properties (Fig. 21l), and the B atom has perfect electron localization (Fig. 21m). These indicate that ZrB$_2$ can be used as sulfur hosts for Li–S batteries.

However, it is difficult to fabricate pure phase ZrB$_2$ because it usually requires high temperatures. Here, the authors prepared ultrafine ZrB$_2$ nanoparticles by a solid-state synthesis at a relatively low temperature. The obtained ZrB$_2$/nitrogen-doped graphene/S (defined as "ZrB$_2$/NG/S") cathode delivers a low-capacity loss of 0.219% per cycle at 0.1C with a sulfur loading (4.8 mg cm^{-2}) and low-electrolyte content (E/S ratio = 8 μL mg^{-1}).

Besides transition metal borides, transition metal fluorides have recently been utilized as electrocatalysts for high-sulfur loading with lean electrolyte Li–S cells. For example, Zhang's group synthesized FeF$_2$@rGO composite via a solvothermal method (Fig. 21n) [281]. They found that FeF$_2$ converts in situ into LiF and FeS during the discharge process. LiF with a low barrier for Li$^+$ ion diffusion can enable fast Li$^+$ ion diffusion. Also, FeS exhibited high affinity to LiPS and catalytic activity for LiPS conversion. DFT calculations analyzed the binding energy between Li$_2$S$_4$ and the
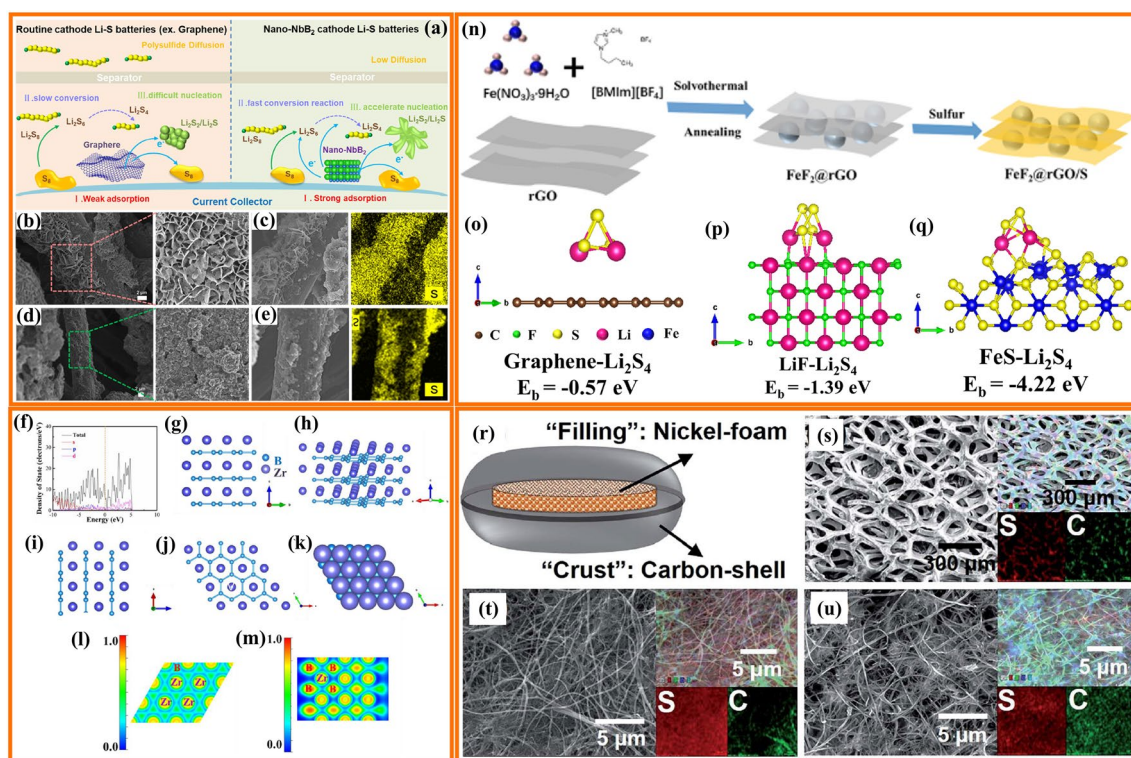

Fig. 21 **a** Illustration of NbB$_2$ promoting LiPS transformation and facilitating Li$_2$S deposition. SEM images of Li$_2$S precipitation: **b** NbB$_2$ and d NPG. Corresponding EDS mapping of S element: **c** NbB$_2$ and **e** NPG [278]. Copyright 2022, American Chemical Society. **f** Partial density of states of ZrB$_2$. **g–j** Cell structure of hexagonal ZrB$_2$. **k** Surface schematic of ZrB$_2$ (001). Electron location function (ELF) of ZrB$_2$: **l** Zr and B atoms at (001) surface, **m** Zr and B atoms at (100) surface [279]. Copyright 2022, Elsevier. **n** FeF$_2$@rGO Synthetic route diagram. Atomic configuration and corresponding binding energy after adsorption of Li$_2$S$_4$, **o** rGO, **p** LiF and **q** FeS [281]. Copyright 2022, Elsevier. **r** Illustration of a nickel-foam@carbon-shell cathode with pie-like architecture. SEM/EDX examination of s nickel-foam, t inner and u outer sides of the carbon shell removed from a cycled nickel-foam@carbon-shell cathode [282]. Copyright, Royal Society of Chemistry

different cathode components after in situ transformation. As shown in Fig. 21o-q, FeS has the most robust adsorption capacity on LiPS with a binding energy of -4.22 eV. As a result, even under high sulfur loading (12.7 mg cm^{-2}) and lean electrolyte conditions (6 µL mg^{-1}), the cells with FeF$_2$@rGO as cathode exhibit a high areal capacity of 12.3 mAh cm^{-2}.

During the past decade, the use of nickel foam as an electrode substrate in Li–S cells has been investigated. For example, Manthiram's group proposed a new pie-like electrode consisting of an electrocatalytic nickel foam and an outer carbon shell for high-energy Li–S batteries with low-electrolyte content (Fig. 21r) [282]. The nickel foam features a 3D porous structure and an uneven surface to achieve high sulfur loading and rich active sites. Meanwhile, the carbon shell consists of an interwoven network of carbon nanotubes and carbon nanofibers, which can retain polysulfides. Figure 21s-u shows the SEM images of the nickel foam and carbon shell after 100 cycles. There is no significant change in their morphology, which means they have excellent mechanical strength. This pie-like structure allows the cathode to have an ultrahigh sulfur loading of 40 mg cm^{-2} and achieve a high areal capacity of over 40 mAh cm^{-2} at 0.2C with a low E/S ratio of 7. This work provides a new strategy for developing optimized cathodes to achieve high energy density Li–S batteries.

3 Conclusions and Perspectives

This review provided a systematic summary of a range of composites of carbon with transition metal-based compounds used in lean electrolyte Li–S batteries. The first topic of discussion was the fundamentals and limitations of the electrochemical conversion of LiPS with low E/S ratios. Then, the functional mechanism and characteristics of the transition metal-based carbon compounds for lean-electrolyte Li–S cell cathode components were comprehensively reviewed. Finally, several possible improvement trends for Li–S batteries in low electrolyte environments were foreseen. Specifically, we discussed the application of carbon-based sulfur hosts containing metal elemental, alloy nanoparticles, metal oxides, phosphides, chalcogenides, nitrides, carbides, borides, fluorides, as well as metal organic frameworks and single atoms of these compounds in lean electrolyte Li–S batteries. By exploiting the inherent characteristics of hybrid nanostructure geometries and

developing their external properties, transition metal-based carbon compound engineering holds a lot of potential and provides a path for constructing high-performance Li–S systems with low electrolyte usage.

While a lot of progress has been made in the development of lean electrolyte Li–S batteries based on these cutting-edge cathode materials, the following points have not received sufficient attention:

i. Heterogeneous electrocatalysts have a limited number of specific catalytic sites; therefore, it is necessary to increase the number of redox-active sites per unit surface area to enhance catalytic activity without changing the catalyst structures. However, the understanding of how the number of active sites influences the electrochemical performance of Li–S cells is still unclear. Therefore, an in-depth study of the relationship between the catalytic site density of catalysts and electrochemical performance of Li–S batteries is required. Furthermore, the catalytic effect of catalysts can be enhanced by increasing the catalyst dosage; however, a large dosage of catalysts can greatly decrease the gravimetric energy density of Li–S cells; thus, a balance needs to be discovered between the high catalyst dosage and the high gravimetric energy density of Li–S cells.

ii. As the redox reaction proceeds, "dead sulfur" can lead to catalyst deactivation; therefore, the effectiveness protection of active sites to maintain sustainable electrocatalytic effects for long-cycle Li–S batteries deserves more attention. Emphasis should be devoted to developing catalysts with improved poisoning resistance to mitigate the negative impacts of "dead sulfur" deposition and catalytic interface poisoning. Furthermore, the exploration of liquid metal catalysts with self-healing and reversible properties holds promise for enhancing the long-term stability and durability of the catalytic system.

iii. The precipitation process and the deposition morphology of Li$_2$S on the electrolyte/electrode surface should be studied, as it significantly influences the transport of Li ions and electrons at the reactive interfaces. Optimized reaction interfaces help to regulate the redox conversion of LiPS, control the nucleation of Li$_2$S and achieve 3D growth of Li$_2$S. Exploring candidates such as stepwise and selective electrocatalysis can offer opportunities for manipulating the kinetics of Li$_2$S nucleation versus growth. In addition, the decomposition of Li$_2$S also deserves special mention. Li$_2$S is hard to be completely oxidized due to the high energy

barrier (E_b) of Li_2S delithiation during charging. In this sense, the design of bidirectional electrocatalysts holds great prospects in accelerating the transformation from insoluble Li_2S to long-chain LiPS.

iv. The balance of carbon content and electrolyte/sulfur ratio should be carefully considered. The minimization of carbon content in the cathode is very important at low E/S ratios as carbon can lead to severe electrolyte depletion due to high electrode porosity. However, recent studies have shown that the rate constant of sulfur redox in the presence of carbon is significantly increased, indicating the importance of electrical conductivity in accelerating sulfur redox reactions. Thus, the balance between carbon content and electrolyte/sulfur ratio should be studied.

v. More research efforts should be directed toward evaluating the electrochemical performance of Li–S pouch cells, especially at high areal sulfur loadings and low E/S ratios, to achieve high energy density Li–S pouch cells exceeding 400 Wh kg^{-1}. The characteristics of multilayer pouch cells and transparent calculations of their components need to be explored further, as these aspects are critical for the commercial application of Li–S batteries.

Declarations

References

1. W. Sun, Z. Song, Z. Feng, Y. Huang, Z.J. Xu et al., Carbon-nitride-based materials for advanced lithium–sulfur batteries. Nano Micro Lett. **14**(1), 222 (2022). https://doi.org/10.1007/s40820-022-00954-x

2. Y. Huang, L. Lin, Y. Zhang, L. Liu, B. Sa et al., Dual-functional lithiophilic/sulfiphilic binary-metal selenide quantum dots toward high-performance Li–S full batteries. Nano Micro Lett. **15**(1), 67 (2023). https://doi.org/10.1007/s40820-023-01037-1

3. A.M. Abraham, K. Thiel, M. Shakouri, Q. Xiao, A. Paterson et al., Ultrahigh sulfur loading tolerant cathode architecture with extended cycle life for high energy density lithium–sulfur batteries. Adv. Energy Mater. **12**(34), 2201494 (2022). https://doi.org/10.1002/aenm.202201494

4. G. Zhou, H. Chen, Y. Cui, Formulating energy density for designing practical lithium–sulfur batteries. Nat. Energy **7**(4), 312–319 (2022). https://doi.org/10.1038/s41560-022-01001-0

5. Z.P. Cano, D. Banham, S. Ye, A. Hintennach, J. Lu et al., Batteries and fuel cells for emerging electric vehicle markets. Nat. Energy **3**(4), 279–289 (2018). https://doi.org/10.1038/s41560-018-0108-1

6. R. Deng, B. Ke, Y. Xie, S. Cheng, C. Zhang et al., All-solid-state thin-film lithium-sulfur batteries. Nano Micro Lett. **15**(1), 73 (2023). https://doi.org/10.1007/s40820-023-01064-y

7. X. Zhu, L. Wang, Z. Bai, J. Lu, T. Wu, Sulfide-based all-solid-state lithium-sulfur batteries: challenges and perspectives. Nano Micro Lett. **15**(1), 75 (2023). https://doi.org/10.1007/s40820-023-01053-1

8. H. Wang, Z. Cui, S.A. He, J. Zhu, W. Luo et al., Construction of ultrathin layered MXene-TiN heterostructure enabling favorable catalytic ability for high-areal-capacity lithium–sulfur batteries. Nano Micro Lett. **14**(1), 189 (2022). https://doi.org/10.1007/s40820-022-00935-0

9. B. Jiang, D. Tian, Y. Qiu, X. Song, Y. Zhang et al., High-index faceted nanocrystals as highly efficient bifunctional electrocatalysts for high-performance lithium–sulfur batteries. Nano Micro Lett. **14**(1), 40 (2021). https://doi.org/10.1007/s40820-021-00769-2

10. Y. Zhan, A. Buffa, L. Yu, Z.J. Xu, D. Mandler, Electrodeposited sulfur and Co_xS electrocatalyst on buckypaper as high-performance cathode for Li-S batteries. Nano Micro Lett. **12**(1), 141 (2020). https://doi.org/10.1007/s40820-020-00479-1

11. J.L. Yang, D.-Q. Cai, Q. Lin, X.-Y. Wang, Z.Q. Fang et al., Regulating the Li_2S deposition by grain boundaries in metal nitrides for stable lithium–sulfur batteries. Nano Energy **91**, 106669 (2022). https://doi.org/10.1016/j.nanoen.2021.106669

12. Y. Qi, N. Li, K. Zhang, Y. Yang, Z. Ren et al., Dynamic liquid metal catalysts for boosted lithium polysulfides redox reaction. Adv. Mater. (2022). https://doi.org/10.1002/adma.202204810

13. Y. Lin, Y. Zhou, S. Huang, M. Xiao, D. Han et al., Catalytic disproportionation for suppressing polysulfide shuttle in Li–S pouch cells: beyond adsorption interactions. Adv. Energy Mater. (2022). https://doi.org/10.1002/aenm.202201912

14. S. Feng, R.K. Singh, Y. Fu, Z. Li, Y. Wang et al., Low-tortuous and dense single-particle-layer electrode for high-energy lithium–sulfur batteries. Energy Environ. Sci. **15**(9), 3842–3853 (2022). https://doi.org/10.1039/d2ee01442d

15. S.F. Ng, M.Y.L. Lau, W.J. Ong, Lithium-sulfur battery cathode design: tailoring metal-based nanostructures for robust polysulfide adsorption and catalytic conversion. Adv. Mater. **33**(50), 2008654 (2021). https://doi.org/10.1002/adma.202008654

16. R.D. Rauh, G.F. Pearson, J.K. Surprenant, S.B. Brummer, A lithium/dissolved sulfur battery with an organic electrolyte. J. Electrochem. Soc. **126**, 523–527 (1979). https://doi.org/10.1149/1.2129079/meta

17. W. Zheng, Y.W. Liu, X.G. Hu, C.F. Zhang, Novel nanosized adsorbing sulfur composite cathode materials for the advanced secondary lithium batteries. Electrochim. Acta **51**(7), 1330–1335 (2006). https://doi.org/10.1016/j.electacta.2005.06.021

18. D. Marmorstein, T.H. Yu, K.A. Striebel, F.R. McLarnon, J. Hou et al., Electrochemical performance of lithiumrsulfur cells with three different polymer electrolytes. J. Power Sources **89**, 219–226 (2000). https://doi.org/10.1016/S0378-7753(00)00432-8

19. D.R. Chang, S.H. Lee, S.W. Kim, H.T. Kim, Binary electrolyte based on tetra(ethylene glycol) dimethyl ether and 1,3-dioxolane for lithium–sulfur battery. J. Power Sources **112**, 452–460 (2002). https://doi.org/10.1016/S0378-7753(02)00418-4

20. D. Marmorstein, K.A. Striebel, F.R. McLarnon, J. Hou, E.J. Cairns, Electrochemical performance of lithiumrsulfur cells with three different polymer electrolytes. J. Power Sources **89**, 219–226 (2000). https://doi.org/10.1016/S0378-7753(00)00432-8

21. L.P. Felix, B. Dias, J.B.J. Veldhuis, Trends in polymer electrolytes for secondary lithium batteries. J. Power Sources **88**, 169–191 (2000). https://doi.org/10.1016/S0378-7753(99)00529-7

22. J. Wang, J. Yang, J. Xie, N. Xu, A novel conductive polymer sulfur composite cathode material for rechargeable lithium. Adv. Mater. **14**, 13–14 (2002). https://doi.org/10.1002/1521-4095(20020705)14:13/14%3c963::AID-ADMA963%3e3.0.CO;2-P

23. Y.V. Mikhaylik, Electrolytes for lithium sulfur cells, US Patent 7, 354, 680 (2008)

24. X. Ji, K.T. Lee, L.F. Nazar, A highly ordered nanostructured carbon–sulphur cathode for lithium–sulphur batteries. Nat. Mater. **8**(6), 500–506 (2009). https://doi.org/10.1038/nmat2460

25. R. Wang, R. Wu, C. Ding, Z. Chen, H. Xu et al., Porous carbon architecture assembled by cross-linked carbon leaves with implanted atomic cobalt for high-performance Li–S batteries. Nano Micro Lett. **13**(1), 151 (2021). https://doi.org/10.1007/s40820-021-00676-6

26. J. Zheng, D. Lv, M. Gu, C. Wang, J. Zhang et al., How to obtain reproducible results for lithium sulfur batteries? J. Electrochem. Soc. **160**(11), 2288–2292 (2013). https://doi.org/10.1149/2.106311jes]

27. M. Hagen, P. Fanz, J. Tübke, Cell energy density and electrolyte/sulfur ratio in Li–S cells. J. Power Sources **264**, 30–34 (2014). https://doi.org/10.1016/j.jpowsour.2014.04.018

28. J. Brückner, S. Thieme, H.T. Grossmann, S. Dörfler, H. Althues, S. Kaskel, Lithium–sulfur batteries: influence of C-rate, amount of electrolyte and sulfur loading on cycle performance. J. Power Sources **268**, 82–87 (2014). https://doi.org/10.1016/j.jpowsour.2014.05.143

29. S.-H. Chung, A. Manthiram, Lithium–sulfur batteries with superior cycle stability by employing porous current collectors. Electrochim. Acta **107**, 569–576 (2013). https://doi.org/10.1016/j.electacta.2013.06.034

30. S. Xiong, K. Xie, Y. Diao, X. Hong, Properties of surface film on lithium anode with $LiNO_3$ as lithium salt in electrolyte solution for lithium–sulfur batteries. Electrochim. Acta **83**, 78–86 (2012). https://doi.org/10.1016/j.electacta.2012.07.118

31. S. Xiong, K. Xie, Y. Diao, X. Hong, On the role of polysulfides for a stable solid electrolyte interphase on the lithium anode cycled in lithium–sulfur batteries. J. Power Sources **236**, 181–187 (2013). https://doi.org/10.1016/j.jpowsour.2013.02.072

32. Y. Yan, Y.-X. Yin, S. Xin, J. Su, Y.-G. Guo et al., High-safety lithium–sulfur battery with prelithiated Si/C anode and ionic liquid electrolyte. Electrochim. Acta **91**, 58–61 (2013). https://doi.org/10.1016/j.electacta.2012.12.077

33. Y.X. Yin, S. Xin, Y.G. Guo, L.J. Wan, Lithium-sulfur batteries: electrochemistry, materials, and prospects. Angew. Chem. Int. Ed. **52**(50), 13186–13200 (2013). https://doi.org/10.1002/anie.201304762

34. Z. Wei Seh, W. Li, J.J. Cha, G. Zheng, Y. Yang et al., Sulphur-TiO_2 yolk-shell nanoarchitecture with internal void space for long-cycle lithium-sulphur batteries. Nat. Commun. **4**, 1331 (2013). https://doi.org/10.1038/ncomms2327

35. S. Dörfler, H. Althues, P. Härtel, T. Abendroth, B. Schumm et al., Challenges and key parameters of lithium–sulfur batteries on pouch cell level. Joule **4**(3), 539–554 (2020). https://doi.org/10.1016/j.joule.2020.02.006

36. L. Huang, T. Guan, H. Su, Y. Zhong, F. Cao et al., Synergistic interfacial bonding in reduced graphene oxide fiber cathodes containing polypyrrole@sulfur nanospheres for flexible

energy storage. Angew. Chem. Int. Ed. (2022). https://doi.org/10.1002/anie.202212151

37. G.T. Zhou, H. Jina, Y. Tao, X. Liu, B. Zhang et al., Catalytic oxidation of Li_2S on the surface of metal sulfides for Li−S batteries. Proc. Natl. Acad. Sci. **114**, 840–845 (2017). https://doi.org/10.1073/pnas.1615837114

38. F. Shi, L. Zhai, Q. Liu, J. Yu, S.P. Lau et al., Emerging catalytic materials for practical lithium–sulfur batteries. J. Energy Chem. **76**, 127–145 (2022). https://doi.org/10.1016/j.jechem.2022.08.027

39. F. Zhan, S. Liu, Q. He, X. Zhao, H. Wang et al., Metal–organic framework-derived heteroatom-doped nanoarchitectures for electrochemical energy storage: recent advances and future perspectives. Energy Storage Mater. **52**, 685–735 (2022). https://doi.org/10.1016/j.ensm.2022.08.035

40. Z. Shen, X. Jin, J. Tian, M. Li, Y. Yuan et al., Cation-doped zns catalysts for polysulfide conversion in lithium–sulfur batteries. Nat. Catal. **5**(6), 555–563 (2022). https://doi.org/10.1038/s41929-022-00804-4

41. Y. Cao, C. Wu, W. Wang, Y. Li, J. You et al., Modification of lithium sulfur batteries by sieving effect: long term investigation of carbon molecular sieve. J. Energy Storage **54**, 105228 (2022). https://doi.org/10.1016/j.est.2022.105228

42. H. Yuan, H.-J. Peng, B.-Q. Li, J. Xie, L. Kong et al., Conductive and catalytic triple-phase interfaces enabling uniform nucleation in high-rate lithium–sulfur batteries. Adv. Energy Mater. **9**(1), 1802768 (2019). https://doi.org/10.1002/aenm.201802768

43. S. Li, X. Zhang, H. Chen, H. Hu, J. Liu et al., Electrocatalytic effect of 3D porous sulfur/gallium hybrid materials in lithium–sulfur batteries. Electrochim. Acta **364**, 137259 (2020). https://doi.org/10.1016/j.electacta.2020.137259

44. Z. Kong, Q. Liu, X. Liu, Y. Wang, C. Shen et al., Co-N_x bonds as bifunctional electrocatalytic sites to drive the reversible conversion of lithium polysulfides for long life lithium sulfur batteries. Appl. Surf. Sci. **546**, 148914 (2021). https://doi.org/10.1016/j.apsusc.2020.148914

45. S. Park, M. Her, H. Shin, W. Hwang, Y.-E. Sung, Maximizing the active site densities of single-atomic Fe–N–C electrocatalysts for high-performance anion membrane fuel cells. ACS Appl. Energy Mater. **4**(2), 1459–1466 (2021). https://doi.org/10.1021/acsaem.0c02650

46. Z. Zeng, W. Nong, Y. Li, C. Wang, Universal-descriptors-guided design of single atom catalysts toward oxidation of Li_2S in lithium–sulfur batteries. Adv. Sci. **8**(23), 2102809 (2021). https://doi.org/10.1002/Adv.s.202102809

47. C. Zhao, G.L. Xu, Z. Yu, L. Zhang, I. Hwang et al., A high-energy and long-cycling lithium–sulfur pouch cell via a macroporous catalytic cathode with double-end binding sites. Nat. Nanotechnol. **16**(2), 166–173 (2021). https://doi.org/10.1038/s41565-020-00797-w

48. Z.X. Chen, M. Zhao, L.P. Hou, X.Q. Zhang, B.Q. Li et al., Toward practical high-energy-density lithium–sulfur pouch cells: a review. Adv. Mater. **34**(35), 2201555 (2022). https://doi.org/10.1002/adma.202201555

49. S. Lang, S.H. Yu, X. Feng, M.R. Krumov, H.D. Abruna, Understanding the lithium–sulfur battery redox reactions via operando confocal Raman microscopy. Nat. Commun. **13**(1), 4811 (2022). https://doi.org/10.1038/s41467-022-32139-w

50. U.J.H. Danuta, Electric dry cells and storage batteries, US Patent 3, 043, 896, (1962)

51. S. Evers, T. Yim, L.F. Nazar, Understanding the nature of absorption/adsorption in nanoporous polysulfide sorbents for the Li–S battery. J. Phys. Chem. C **116**(37), 19653–19658 (2012). https://doi.org/10.1021/jp304380j

52. J. Lei, T. Liu, J. Chen, M. Zheng, Q. Zhang et al., Exploring and understanding the roles of Li_2S_n and the strategies to beyond present Li–S batteries. Chem. **6**(10), 2533–2557 (2020). https://doi.org/10.1016/j.chempr.2020.06.032

53. T.M. Gür, Review of electrical energy storage technologies, materials and systems: challenges and prospects for large-scale grid storage. Energy Environ. Sci. **11**(10), 2696–2767 (2018). https://doi.org/10.1039/c8ee01419a

54. Z. Li, I. Sami, J. Yang, J. Li, R.V. Kumar et al., Lithiated metallic molybdenum disulfide nanosheets for high-performance lithium–sulfur batteries. Nat. Energy **8**(1), 84–93 (2023). https://doi.org/10.1038/s41560-022-01175-7

55. F. Cheng, J. Liang, Z. Tao, J. Chen, Functional materials for rechargeable batteries. Adv. Mater. **23**(15), 1695–1715 (2011). https://doi.org/10.1002/adma.201003587

56. M. Han, Y. Mu, J. Guo, L. Wei, L. Zeng et al., Monolayer MoS_2 fabricated by in situ construction of interlayer electrostatic repulsion enables ultrafast ion transport in lithium-ion batteries. Nano Micro Lett. **15**(1), 80 (2023). https://doi.org/10.1007/s40820-023-01042-4

57. D. Moy, A. Manivannan, S.R. Narayanan, Direct measurement of polysulfide shuttle current: a window into understanding the performance of lithium-sulfur cells. J. Electrochem. Soc. **162**, A1–A7 (2015). https://doi.org/10.1149/2.0181501jes

58. C. Yang, Running battery electric vehicles with extended range: coupling cost and energy analysis. Appl. Energy **306**, 118116 (2022). https://doi.org/10.1016/j.apenergy.2021.118116

59. J. Wu, T. Ye, Y. Wang, P. Yang, Q. Wang et al., Understanding the catalytic kinetics of polysulfide redox reactions on transition metal compounds in Li–S batteries. ACS Nano **16**(10), 15734–15759 (2022). https://doi.org/10.1021/acsnano.2c08581

60. C. Shen, J. Xie, M. Zhang, P. Andrei, M. Hendrickson et al., Self-discharge behavior of lithium–sulfur batteries at different electrolyte/sulfur ratios. J. Electrochem. Soc. **166**, A5287 (2019). https://doi.org/10.1149/2.0461903jes

61. J. Zhang, G. Xu, Q. Zhang, X. Li, Y. Yang et al., Mo–O–C between MoS_2 and graphene toward accelerated polysulfide catalytic conversion for advanced lithium–sulfur batteries. Adv. Sci. **9**(22), 2201579 (2022). https://doi.org/10.1002/advs.202201579

62. Z. Ye, Y. Jiang, T. Yang, L. Li, F. Wu et al., Engineering catalytic CoSe-ZnSe heterojunctions anchored on graphene

aerogels for bidirectional sulfur conversion reactions. Adv. Sci. **9**(1), 2103456 (2022). https://doi.org/10.1002/advs.202103456

63. D. Yang, Z. Liang, P. Tang, C. Zhang, M. Tang et al., A high conductivity 1D π-d conjugated metal-organic framework with efficient polysulfide trapping-diffusion-catalysis in lithium–sulfur batteries. Adv. Mater. **34**(10), 2108835 (2022). https://doi.org/10.1002/adma.202108835

64. Y.T. Liu, S. Liu, G.R. Li, X.P. Gao, Strategy of enhancing the volumetric energy density for lithium–sulfur batteries. Adv. Mater. **33**(8), 2003955 (2021). https://doi.org/10.1002/adma.202003955

65. W. Xue, L. Miao, L. Qie, C. Wang, S. Li et al., Gravimetric and volumetric energy densities of lithium–sulfur batteries. Curr. Opin. Electrochem. **6**(1), 92–99 (2017). https://doi.org/10.1016/j.coelec.2017.10.007

66. J. Betz, G. Bieker, P. Meister, T. Placke, M. Winter et al., Theoretical versus practical energy: a plea for more transparency in the energy calculation of different rechargeable battery systems. Adv. Energy Mater. **9**(6), 1803170 (2018). https://doi.org/10.1002/aenm.201803170

67. S. Power, 650 w/hkg, 1400 wh/l rechargable batteries for new era of electrified mobility. 2018 NASA Aerospace Battery Workshop (2018).

68. S. Kaskel, Recent progress in lithium–sulfur-batteries. AABC Europe 2017 (2017)

69. H.J. Peng, J.Q. Huang, Q. Zhang, A review of flexible lithium–sulfur and analogous alkali metal-chalcogen rechargeable batteries. Chem. Soc. Rev. **46**(17), 5237–5288 (2017). https://doi.org/10.1039/c7cs00139h

70. N. Li, C. Sun, J. Zhu, S. Li, Y. Wang et al., Minimizing carbon content with three-in-one functionalized nano conductive ceramics: toward more practical and safer S cathodes of Li–S cells. Energy Environ. Mater. (2022). https://doi.org/10.1002/eem2.12354

71. S.H. Chung, C.H. Chang, A. Manthiram, A carbon-cotton cathode with ultrahigh-loading capability for statically and dynamically stable lithium–sulfur batteries. ACS Nano **10**(11), 10462–10470 (2016). https://doi.org/10.1021/acsnano.6b06369

72. C.-H. Chang, S.-H. Chung, A. Manthiram, Highly flexible, freestanding tandem sulfur cathodes for foldable Li–S batteries with a high areal capacity. Mater. Horiz. **4**(2), 249–258 (2017). https://doi.org/10.1039/c6mh00426a

73. P. Han, S.H. Chung, A. Manthiram, Pyrrolic-type nitrogen-doped hierarchical macro/mesoporous carbon as a bifunctional host for high-performance thick cathodes for lithium–sulfur batteries. Small **15**(16), 1900690 (2019). https://doi.org/10.1002/smll.201900690

74. D.R. Deng, F. Xue, Y.J. Jia, J.C. Ye, C.D. Bai et al., Co_4N nanosheet assembled mesoporous sphere as a matrix for ultrahigh sulfur content lithium–sulfur batteries. ACS Nano **11**(6), 6031–6039 (2017). https://doi.org/10.1021/acsnano.7b01945

75. D.R. Deng, F. Xue, C.D. Bai, J. Lei, R. Yuan et al., Enhanced adsorptions to polysulfides on graphene-supported bn nanosheets with excellent Li–S battery performance in a wide temperature range. ACS Nano **12**(11), 11120–11129 (2018). https://doi.org/10.1021/acsnano.8b05534

76. Z. Yuan, H.J. Peng, T.Z. Hou, J.Q. Huang, C.M. Chen et al., Powering lithium–sulfur battery performance by propelling polysulfide redox at sulfiphilic hosts. Nano Lett. **16**(1), 519–527 (2016). https://doi.org/10.1021/acs.nanolett.5b04166

77. X. Liang, C. Hart, Q. Pang, A. Garsuch, T. Weiss et al., A highly efficient polysulfide mediator for lithium-sulfur batteries. Nat. Commun. **6**, 5682 (2015). https://doi.org/10.1038/ncomms6682

78. M. Zhao, B.Q. Li, H.J. Peng, H. Yuan, J.Y. Wei et al., Lithium–sulfur batteries under lean electrolyte conditions: challenges and opportunities. Angew. Chem. Int. Ed. **59**(31), 12636–12652 (2020). https://doi.org/10.1002/anie.201909339

79. M. Zhao, B.Q. Li, X.Q. Zhang, J.Q. Huang, Q. Zhang, A perspective toward practical lithium–sulfur batteries. ACS Cent. Sci. **6**(7), 1095–1104 (2020). https://doi.org/10.1021/acscentsci.0c00449

80. Y. Jin, P.M.L. Le, P. Gao, Y. Xu, B. Xiao et al., Low-solvation electrolytes for high-voltage sodium-ion batteries. Nat. Energy **7**(8), 718–725 (2022). https://doi.org/10.1038/s41560-022-01055-0

81. Y. Jeoun, M.-S. Kim, S.-H. Lee, J. Hyun Um, Y.-E. Sung et al., Lean-electrolyte lithium-sulfur batteries: recent advances in the design of cell components. Chem. Eng. J. **450**, 138209 (2022). https://doi.org/10.1016/j.cej.2022.138209

82. J. Guo, H. Pei, Y. Dou, S. Zhao, G. Shao et al., Rational designs for lithium-sulfur batteries with low electrolyte/sulfur ratio. Adv. Funct. Mater. **31**(18), 2010499 (2021). https://doi.org/10.1002/adfm.202010499

83. M. Wild, L. O'Neill, T. Zhang, R. Purkayastha, G. Minton et al., Lithium sulfur batteries, a mechanistic review. Energy Environ. Sci. **8**(12), 3477–3494 (2015). https://doi.org/10.1039/c5ee01388g

84. H.J. Peng, J.Q. Huang, X.Y. Liu, X.B. Cheng, W.T. Xu et al., Healing high-loading sulfur electrodes with unprecedented long cycling life: spatial heterogeneity control. J. Am. Chem. Soc. **139**(25), 8458–8466 (2017). https://doi.org/10.1021/jacs.6b12358

85. X.-B. Cheng, J.-Q. Huang, H.-J. Peng, J.-Q. Nie, X.-Y. Liu et al., Polysulfide shuttle control: towards a lithium–sulfur battery with superior capacity performance up to 1000 cycles by matching the sulfur/electrolyte loading. J. Power Sources **253**, 263–268 (2014). https://doi.org/10.1016/j.jpowsour.2013.12.031

86. C. Zu, A. Manthiram, Stabilized lithium-metal surface in a polysulfide-rich environment of lithium–sulfur batteries. J. Phys. Chem. Lett. **5**(15), 2522–2527 (2014). https://doi.org/10.1021/jz501352e

87. M. Zhang, W. Chen, L. Xue, Y. Jiao, T. Lei et al., Adsorption-catalysis design in the lithium–sulfur battery. Adv.

Energy Mater. **10**(2), 1903008 (2019). https://doi.org/10.1002/aenm.201903008

88. Y. Shi, M. Li, Y. Yu, B. Zhang, Recent advances in nanostructured transition metal phosphides: synthesis and energy-related applications. Energy Environ. Sci. **13**(12), 4564–4582 (2020). https://doi.org/10.1039/d0ee02577a

89. S. Huang, E. Huixiang, Y. Yang, Y. Zhang, M. Ye et al., Transition metal phosphides: new generation cathode host/separator modifier for Li–S batteries. J. Mater. Chem. A **9**(12), 7458–7480 (2021). https://doi.org/10.1039/d0ta11919a

90. Z. Cheng, Z. Wu, J. Chen, Y. Fang, S. Lin et al., Mo_2N-ZrO_2 heterostructure engineering in freestanding carbon nanofibers for upgrading cycling stability and energy efficiency of Li-CO_2 batteries. Small **19**, 2301685 (2023). https://doi.org/10.1002/smll.202301685

91. M. Wang, Z. Bai, T. Yang, C. Nie, X. Xu et al., Advances in high sulfur loading cathodes for practical lithium–sulfur batteries. Adv. Energy Mater. **12**(39), 2201585 (2022). https://doi.org/10.1002/aenm.202201585

92. M. Cui, Z. Zheng, J. Wang, Y. Wang, X. Zhao et al., Rational design of lithium–sulfur battery cathodes based on differential atom electronegativity. Energy Storage Mater. **35**, 577–585 (2021). https://doi.org/10.1016/j.ensm.2020.11.039

93. H. Ye, J. Sun, S. Zhang, H. Lin, T. Zhang et al., Stepwise electrocatalysis as a strategy against polysulfide shuttling in Li–S batteries. ACS Nano **13**(12), 14208–14216 (2019). https://doi.org/10.1021/acsnano.9b07121

94. H. Shin, M. Baek, A. Gupta, K. Char, A. Manthiram et al., Recent progress in high donor electrolytes for lithium–sulfur batteries. Adv. Energy Mater. **10**(27), 2001456 (2020). https://doi.org/10.1002/aenm.202001456

95. Y. Li, C. Wang, W. Wang, A.Y.S. Eng, M. Wan et al., Enhanced chemical immobilization and catalytic conversion of polysulfide intermediates using metallic Mo nanoclusters for high-performance Li–S batteries. ACS Nano **14**(1), 1148–1157 (2020). https://doi.org/10.1021/acsnano.9b09135

96. Z. Yu, B. Wang, X. Liao, K. Zhao, Z. Yang et al., Boosting polysulfide redox kinetics by graphene-supported Ni nanoparticles with carbon coating. Adv. Energy Mater. **10**(25), 2000907 (2020). https://doi.org/10.1002/aenm.202000907

97. D. Guo, X. Zhang, M. Liu, Z. Yu, X.A. Chen et al., Single Mo-N_4 atomic sites anchored on N-doped carbon nanoflowers as sulfur host with multiple immobilization and catalytic effects for high-performance lithium–sulfur batteries. Adv. Funct. Mater. **32**(35), 2204458 (2020). https://doi.org/10.1002/adfm.202204458

98. K. Zhang, W. Cai, Y. Liu, G. Hu, W. Hu et al., Nitrogen-doped carbon embedded with ag nanoparticles for bidirectionally-promoted polysulfide redox electrochemistry. Chem. Eng. J. **427**, 130897 (2022). https://doi.org/10.1016/j.cej.2021.130897

99. L. Chen, X. Liu, L. Zheng, Y. Li, X. Guo et al., Insights into the role of active site density in the fuel cell performance of Co–N–C catalysts. Appl. Catal. B **256**, 117849 (2019). https://doi.org/10.1016/j.apcatb.2019.117849

100. E. Jung, S.-J. Kim, J. Kim, S. Koo, J. Lee et al., Oxygen-plasma-treated Fe–N–C catalysts with dual binding sites for enhanced electrocatalytic polysulfide conversion in lithium–sulfur batteries. ACS Energy Lett. **7**(8), 2646–2653 (2022). https://doi.org/10.1021/acsenergylett.2c01132

101. J. Kim, S.J. Kim, E. Jung, D.H. Mok, V.K. Paidi et al., Atomic structure modification of Fe–N–C catalysts via morphology engineering of graphene for enhanced conversion kinetics of lithium–sulfur batteries. Adv. Funct. Mater. **32**(19), 2110857 (2022). https://doi.org/10.1002/adfm.202110857

102. J. Luo, H. Liu, K. Guan, W. Lei, Q. Jia et al., Cobalt nanoparticles decorated "wire in tube" framework as a multifunctional sulfur reservoir. ACS Sustain. Chem. Eng. **10**(18), 6117–6127 (2022). https://doi.org/10.1021/acssuschemeng.2c01883

103. Y. Tsao, H. Gong, S. Chen, G. Chen, Y. Liu et al., A nickel-decorated carbon flower/sulfur cathode for lean-electrolyte lithium–sulfur batteries. Adv. Energy Mater. **11**(36), 2101449 (2021). https://doi.org/10.1002/aenm.202101449

104. Z. Lin, X. Li, W. Huang, X. Zhu, Y. Wang et al., Active platinum nanoparticles as a bifunctional promoter for lithium–sulfur batteries. ChemElectroChem **4**(10), 2577–2582 (2017). https://doi.org/10.1002/celc.201700533

105. P. Wang, Z. Zhang, X. Yan, M. Xu, Y. Chen et al., Pomegranate-like microclusters organized by ultrafine Co nanoparticles@nitrogen-doped carbon subunits as sulfur hosts for long-life lithium–sulfur batteries. J. Mater. Chem. A **6**(29), 14178–14187 (2018). https://doi.org/10.1039/c8ta04214d

106. L. Zhang, D. Liu, Z. Muhammad, F. Wan, W. Xie et al., Single nickel atoms on nitrogen-doped graphene enabling enhanced kinetics of lithium–sulfur batteries. Adv. Mater. **31**(40), 1903955 (2019). https://doi.org/10.1002/adma.201903955

107. W. Zang, Z. Kou, S.J. Pennycook, J. Wang, Heterogeneous single atom electrocatalysis, where "singles" are "married." Adv. Energy Mater. **10**(9), 1903181 (2020). https://doi.org/10.1002/aenm.201903181

108. X. Wang, A. Beck, J.A. van Bokhoven, D. Palagin, Thermodynamic insights into strong metal–support interaction of transition metal nanoparticles on titania: simple descriptors for complex chemistry. J. Mater. Chem. A **9**(7), 4044–4054 (2021). https://doi.org/10.1039/d0ta11650e

109. J.G. Smith, P.K. Jain, The ligand shell as an energy barrier in surface reactions on transition metal nanoparticles. J. Am. Chem. Soc. **138**(21), 6765–6773 (2016). https://doi.org/10.1021/jacs.6b00179

110. H. Gao, S. Ning, Y. Zhou, S. Men, X. Kang, Polyacrylonitrile-induced formation of core-shell carbon nanocages: enhanced redox kinetics towards polysulfides by confined catalysis in Li–S batteries. Chem. Eng. J. **408**, 127323 (2021). https://doi.org/10.1016/j.cej.2020.127323

111. C. Li, S. Qi, L. Zhu, Y. Zhao, R. Huang et al., Regulating polysulfide intermediates by ultrathin Co–Bi nanosheet electrocatalyst in lithium–sulfur batteries. Nano Today **40**, 101246 (2021). https://doi.org/10.1016/j.nantod.2021.101246

112. Y. Li, W. Wang, B. Zhang, L. Fu, M. Wan et al., Manipulating redox kinetics of sulfur species using Mott-Schottky electrocatalysts for advanced lithium–sulfur batteries. Nano Lett. **21**(15), 6656–6663 (2021). https://doi.org/10.1021/acs.nanolett.1c02161

113. Q. Shao, L. Xu, D. Guo, Y. Su, J. Chen, Atomic level design of single iron atom embedded mesoporous hollow carbon spheres as multi-effect nanoreactors for advanced lithium–sulfur batteries. J. Mater. Chem. A **8**(45), 23772–23783 (2020). https://doi.org/10.1039/d0ta07010f

114. Z.-L. Xu, S.J. Kim, D. Chang, K.-Y. Park, K.S. Dae et al., Visualization of regulated nucleation and growth of lithium sulfides for high energy lithium sulfur batteries. Energy Environ. Sci. **12**(10), 3144–3155 (2019). https://doi.org/10.1039/c9ee01338e

115. C. Li, Y. Zhao, Y. Zhang, D. Luo, J. Liu et al., A new defect-rich and ultrathin ZnCo layered double hydroxide/carbon nanotubes architecture to facilitate catalytic conversion of polysulfides for high-performance Li–S batteries. Chem. Eng. J. **417**, 129248 (2021). https://doi.org/10.1016/j.cej.2021.129248

116. H. Pan, X. Huang, C. Wang, D. Liu, D. Wang et al., Sandwich structural Ti_xO_y-Ti_3C_2/C_3N_4 material for long life and fast kinetics lithium-sulfur battery: bidirectional adsorption promoting lithium polysulfide conversion. Chem. Eng. J. **410**, 128424 (2021). https://doi.org/10.1016/j.cej.2021.128424

117. W. Wang, L. Huai, S. Wu, J. Shan, J. Zhu et al., Ultrahigh-volumetric-energy-density lithium–sulfur batteries with lean electrolyte enabled by cobalt-doped $MoSe_2$/$Ti_3C_2T_x$ mxene bifunctional catalyst. ACS Nano **15**, 11619–11633 (2021). https://doi.org/10.1021/acsnano.1c02047

118. Y. Xiao, S. Guo, Y. Ouyang, D. Li, X. Li et al., Constructing heterogeneous structure in metal-organic framework-derived hierarchical sulfur hosts for capturing polysulfides and promoting conversion kinetics. ACS Nano **15**, 18363–18373 (2021). https://doi.org/10.1021/acsnano.1c07820

119. H. Guo, J. Hu, H. Yuan, N. Wu, Y. Li et al., Ternary transition metal sulfide as high real energy cathode for lithium–sulfur pouch cell under lean electrolyte conditions. Small Methods **6**(2), 2101402 (2022). https://doi.org/10.1002/smtd.202101402

120. J. He, A. Bhargav, A. Manthiram, High-performance anode-free Li–S batteries with an integrated Li_2S–electrocatalyst cathode. ACS Energy Lett. **7**(2), 583–590 (2022). https://doi.org/10.1021/acsenergylett.1c02569

121. V.P. Nguyen, I.H. Kim, H.C. Shim, J.S. Park, J.M. Yuk et al., Porous carbon textile decorated with VC/$V_2O_{3−x}$ hybrid nanoparticles: dual-functional host for flexible Li–S full batteries. Energy Storage Mater. **46**, 542–552 (2022). https://doi.org/10.1016/j.ensm.2022.01.027

122. H. Ye, J. Sun, Y. Zhao, J.Y. Lee, An integrated approach to improve the performance of lean–electrolyte lithium–sulfur batteries. J. Energy Chem. **67**, 585–592 (2022). https://doi.org/10.1016/j.jechem.2021.11.004

123. X. Zhong, D. Wang, J. Sheng, Z. Han, C. Sun et al., Freestanding and sandwich mxene-based cathode with suppressed lithium polysulfides shuttle for flexible lithium–sulfur batteries. Nano Lett. **22**(3), 1207–1216 (2022). https://doi.org/10.1021/acs.nanolett.1c04377

124. M. Zhang, C. Yu, C. Zhao, X. Song, X. Han et al., Cobalt-embedded nitrogen-doped hollow carbon nanorods for synergistically immobilizing the discharge products in lithium–sulfur battery. Energy Storage Mater. **5**, 223–229 (2016). https://doi.org/10.1016/j.ensm.2016.04.002

125. D. Xiao, Q. Li, H. Zhang, Y. Ma, C. Lu et al., A sulfur host based on cobalt–graphitic carbon nanocages for high performance lithium–sulfur batteries. J. Mater. Chem. A **5**(47), 24901–24908 (2017). https://doi.org/10.1039/c7ta08483h

126. S. Liu, J. Li, X. Yan, Q. Su, Y. Lu et al., Superhierarchical cobalt-embedded nitrogen-doped porous carbon nanosheets as two-in-one hosts for high-performance lithium–sulfur batteries. Adv. Mater. **30**(12), 1706895 (2018). https://doi.org/10.1002/adma.201706895

127. Z. Du, X. Chen, W. Hu, C. Chuang, S. Xie et al., Cobalt in nitrogen-doped graphene as single-atom catalyst for high-sulfur content lithium–sulfur batteries. J. Am. Chem. Soc. **141**(9), 3977–3985 (2019). https://doi.org/10.1021/jacs.8b12973

128. D. Wang, G. Zheng, W. Zhang, X. Niu, J. Yan et al., A highly stable cathode for lithium–sulfur battery built of Ni-doped carbon framework linked to CNT. J. Alloys Compd. **881**, 160496 (2021). https://doi.org/10.1016/j.jallcom.2021.160496

129. L. He, D. Yang, H. Zhao, L. Wei, D. Wang et al., Bipolar $CoSe_2$ nanocrystals embedded in porous carbon nanocages as an efficient electrocatalyst for Li–S batteries. Chem. Eng. J. **440**, 135820 (2022). https://doi.org/10.1016/j.cej.2022.135820

130. B. Li, P. Wang, B. Xi, N. Song, X. An et al., In-situ embedding cote catalyst into 1D–2D nitrogen-doped carbon to didirectionally regulate lithium–sulfur batteries. Nano Res. **15**, 8972–8982 (2022). https://doi.org/10.1007/s12274-022-4537-6

131. H. Gao, S. Miao, M. Shi, X. Mao, X. Zhu, In situ-formed cobalt nanoparticles embedded nitrogen-doped hierarchical porous carbon as sulfur host for high-performance Li–S batteries. Electrochim. Acta **403**, 139717 (2022). https://doi.org/10.1016/j.electacta.2021.139717

132. G. Li, W. Lei, D. Luo, Y. Deng, Z. Deng et al., Stringed "tube on cube" nanohybrids as compact cathode matrix for high-loading and lean-electrolyte lithium–sulfur batteries. Energy Environ. Sci. **11**(9), 2372–2381 (2018). https://doi.org/10.1039/c8ee01377b

133. Q. Wu, X. Zhou, J. Xu, F. Cao, C. Li, Adenine derivative host with interlaced 2D structure and dual lithophilic-sulfiphilic sites to enable high-loading Li–S batteries. ACS Nano **13**(8), 9520–9532 (2019). https://doi.org/10.1021/acsnano.9b04519

134. D. Wang, K. Ma, J. Hao, W. Zhang, C. Wang et al., Multifunction Co-N_x species to manipulate polysulfides conversion kinetics toward highly efficient lithium–sulfur batteries. Nano

Energy **89**, 106426 (2021). https://doi.org/10.1016/j.nanoen.2021.106426

135. B. Du, Y. Luo, Y. Yang, W. Xue, G. Liu et al., COFs-confined multifunctional sulfur-host design towards high-performance lithium–sulfur batteries. Chem. Eng. J. **442**, 135823 (2022). https://doi.org/10.1016/j.cej.2022.135823

136. L. Su, J. Zhang, Y. Chen, W. Yang, J. Wang et al., Cobalt-embedded hierarchically-porous hollow carbon microspheres as multifunctional confined reactors for high-loading Li–S batteries. Nano Energy **85**, 105981 (2021). https://doi.org/10.1016/j.nanoen.2021.105981

137. Z. Cheng, H. Pan, Z. Wu, M. Wubbenhorst, Z. Zhang, Cu–Mo bimetal modulated multifunctional carbon nanofibers promoting the polysulfides conversion for high-sulfur-loading lithium–sulfur batteries. ACS Appl. Mater. Interfaces **14**(40), 45688–45696 (2022). https://doi.org/10.1021/acsami.2c13012

138. J. He, A. Bhargav, A. Manthiram, High-energy-density, long-life lithium–sulfur batteries with practically necessary parameters enabled by low-cost Fe–Ni nanoalloy catalysts. ACS Nano **15**(5), 8583–8591 (2021). https://doi.org/10.1021/acsnano.1c00446

139. Z. Wang, H. Ge, S. Liu, G. Li, X. Gao, High-entropy alloys to activate the sulfur cathode for lithium–sulfur batteries. Energy Environ. Mater (2022). https://doi.org/10.1002/eem2.12358

140. Z.Y. Wang, B. Zhang, S. Liu, G.R. Li, T. Yan et al., Nickel-platinum alloy nanocrystallites with high-index facets as highly effective core catalyst for lithium–sulfur batteries. Adv. Funct. Mater. **32**(27), 2200893 (2022). https://doi.org/10.1002/adfm.202200893

141. H. Pan, Z. Cheng, J. Fransaer, J. Luo, M. Wübbenhorst, Cobalt-embedded 3D conductive honeycomb architecture to enable high-sulphur-loading Li–S batteries under lean electrolyte conditions. Nano Res. **15**(9), 8091–8100 (2022). https://doi.org/10.1007/s12274-022-4486-0

142. H. Pei, Q. Yang, J. Yu, H. Song, S. Zhao et al., Self-supporting carbon nanofibers with Ni-single-atoms and uniformly dispersed Ni-nanoparticles as scalable multifunctional hosts for high energy density lithium–sulfur batteries. Small **18**(27), 2202037 (2022). https://doi.org/10.1002/smll.202202037

143. Y. Jin, F. Chen, J. Wang, R.L. Johnston, Tuning electronic and composition effects in ruthenium-copper alloy nanoparticles anchored on carbon nanofibers for rechargeable Li–CO₂ batteries. Chem. Eng. J. **375**, 121978 (2019). https://doi.org/10.1016/j.cej.2019.121978

144. L. Wang, H. Wang, S. Zhang, N. Ren, Y. Wu et al., Manipulating the electronic structure of nickel via alloying with iron: toward high-kinetics sulfur cathode for Na–S batteries. ACS Nano **15**(9), 15218–15228 (2021). https://doi.org/10.1021/acsnano.1c05778

145. Z.Y. Wang, H.M. Wang, S. Liu, G.R. Li, X.P. Gao, To promote the catalytic conversion of polysulfides using Ni–B alloy nanoparticles on carbon nanotube microspheres under high sulfur loading and a lean electrolyte. ACS Appl. Mater. Interfaces **13**(17), 20222–20232 (2021). https://doi.org/10.1021/acsami.1c03791

146. X. Zhou, T. Liu, G. Zhao, X. Yang, H. Guo, Cooperative catalytic interface accelerates redox kinetics of sulfur species for high-performance li–s batteries. Energy Storage Mater. **40**, 139–149 (2021). https://doi.org/10.1016/j.ensm.2021.05.009

147. X. Song, D. Tian, Y. Qiu, X. Sun, B. Jiang et al., Improving poisoning resistance of electrocatalysts via alloying strategy for high-performance lithium–sulfur batteries. Energy Storage Mater. **41**, 248–254 (2021). https://doi.org/10.1016/j.ensm.2021.05.028

148. Y. Liu, W. Kou, X. Li, C. Huang, R. Shui et al., Constructing patch-Ni-shelled Pt@Ni nanoparticles within confined nanoreactors for catalytic oxidation of insoluble polysulfides in Li–S batteries. Small **15**(34), 1902431 (2019). https://doi.org/10.1002/smll.201902431

149. G. Li, W. Qiu, W. Gao, Y. Zhu, X. Zhang et al., Finely-dispersed Ni₂Co nanoalloys on flower-like graphene microassembly empowering a bi-service matrix for superior lithium–sulfur electrochemistry. Adv. Funct. Mater. **32**(32), 2202853 (2022). https://doi.org/10.1002/adfm.202202853

150. F.Y. Fan, Y.-M. Chiang, Electrodeposition kinetics in Li–S batteries: effects of low electrolyte/sulfur ratios and deposition surface composition. J. Electrochem. Soc. **164**(4), 917–922 (2017). https://doi.org/10.1149/2.0051706jes]

151. M. Chen, C. Huang, Y. Li, S. Jiang, P. Zeng et al., Perovskite-type La₀.₅₆Li₀.₃₃TiO₃ as an effective polysulfide promoter for stable lithium–sulfur batteries in lean electrolyte conditions. J. Mater. Chem. A **7**(17), 10293–10302 (2019). https://doi.org/10.1039/c9ta01500k

152. K. Lu, Y. Liu, J. Chen, Z. Zhang, Y. Cheng, Redox catalytic and quasi-solid sulfur conversion for high-capacity lean lithium sulfur batteries. ACS Nano **13**(12), 14540–14548 (2019). https://doi.org/10.1021/acsnano.9b08516

153. J. Lee, J.H. Moon, Polyhedral TiO₂ particle-based cathode for Li–S batteries with high volumetric capacity and high performance in lean electrolyte. Chem. Eng. J. **399**, 125670 (2020). https://doi.org/10.1016/j.cej.2020.125670

154. H. Pan, Z. Cheng, X. Zhang, K. Wan, J. Fransaer et al., Manganese dioxide nanosheet functionalized reduced graphene oxide as a compacted cathode matrix for lithium–sulphur batteries with a low electrolyte/sulphur ratio. J. Mater. Chem. A **8**(41), 21824–21832 (2020). https://doi.org/10.1039/d0ta05021k

155. J. Wang, G. Li, D. Luo, Y. Zhang, Y. Zhao et al., Engineering the conductive network of metal oxide-based sulfur cathode toward efficient and longevous lithium–sulfur batteries. Adv. Energy Mater. **10**(41), 2002076 (2020). https://doi.org/10.1002/aenm.202002076

156. J. Wang, D. Luo, J. Li, Y. Zhang, Y. Zhao et al., "Soft on rigid" nanohybrid as the self-supporting multifunctional cathode electrocatalyst for high-performance lithium–polysulfide batteries. Nano Energy **78**, 105293 (2020). https://doi.org/10.1016/j.nanoen.2020.105293

157. L. Wang, Z.-Y. Wang, J.-F. Wu, G.-R. Li, S. Liu et al., To effectively drive the conversion of sulfur with electroactive niobium tungsten oxide microspheres for lithium–sulfur battery. Nano Energy **77**, 105173 (2020). https://doi.org/10.1016/j.nanoen.2020.105173

158. L. Wang, G.R. Li, S. Liu, X.P. Gao, Hollow molybdate microspheres as catalytic hosts for enhancing the electrochemical performance of sulfur cathode under high sulfur loading and lean electrolyte. Adv. Funct. Mater. **31**(18), 2010693 (2021). https://doi.org/10.1002/adfm.202010693

159. Z. He, T. Wan, Y. Luo, G. Liu, L. Wu et al., Three-dimensional structural confinement design of conductive metal oxide for efficient sulfur host in lithium–sulfur batteries. Chem. Eng. J. **448**, 137656 (2022). https://doi.org/10.1016/j.cej.2022.137656

160. J. Guo, Y. Huang, S. Zhao, Z. Li, Z. Wang et al., Array-structured double-ion cooperative adsorption sites as multifunctional sulfur hosts for lithium–sulfur batteries with low electrolyte/sulfur ratio. ACS Nano **15**(10), 16322–16334 (2021). https://doi.org/10.1021/acsnano.1c05536

161. L. Niu, T. Wu, D. Zhou, J. Qi, Z. Xiao, Polaron hopping-mediated dynamic interactive sites boost sulfur chemistry for flexible lithium–sulfur batteries. Energy Storage Mater. **45**, 840–850 (2022). https://doi.org/10.1016/j.ensm.2021.12.039

162. Z. Zhang, D. Luo, G. Li, R. Gao, M. Li et al., Tantalum-based electrocatalyst for polysulfide catalysis and retention for high-performance lithium-sulfur batteries. Matter **3**(3), 920–934 (2020). https://doi.org/10.1016/j.matt.2020.06.002

163. H. Zhang, L. Yang, P. Zhang, C. Lu, D. Sha et al., Mxene-derived Ti_nO_{2n-1} quantum dots distributed on porous carbon nanosheets for stable and long-life Li–S batteries: enhanced polysulfide mediation via defect engineering. Adv. Mater. **33**(21), 2008447 (2021). https://doi.org/10.1002/adma.202008447

164. Z. Li, J. Wu, P. Chen, Q. Zeng, X. Wen et al., A new metallic composite cathode originated from hyperbranched polymer coated mof for high-performance lithium–sulfur batteries. Chem. Eng. J. **435**, 135125 (2022). https://doi.org/10.1016/j.cej.2022.135125

165. K. Zou, T. Zhou, Y. Chen, X. Xiong, W. Jing et al., Defect engineering in a multiple confined geometry for robust lithium–sulfur batteries. Adv. Energy Mater. **12**(18), 2103981 (2022). https://doi.org/10.1002/aenm.202103981

166. S. Chen, J. Zhang, Z. Wang, L. Nie, X. Hu et al., Electrocatalytic $NiCo_2O_4$ nanofiber arrays on carbon cloth for flexible and high-loading lithium–sulfur batteries. Nano Lett. **21**(12), 5285–5292 (2021). https://doi.org/10.1021/acs.nanolett.1c01422

167. L. Wang, W. Hua, X. Wan, Z. Feng, Z. Hu et al., Design rules of a sulfur redox electrocatalyst for lithium-sulfur batteries. Adv. Mater. **34**(14), e2110279 (2022). https://doi.org/10.1002/adma.202110279

168. Y. Lu, J.L. Qin, T. Shen, Y.F. Yu, K. Chen et al., Hyper-crosslinked polymerization enabled N-doped carbon confined Fe_2O_3 facilitating Li polysulfides interface conversion for Li–S batteries. Adv. Energy Mater. **11**(42), 2101780 (2021). https://doi.org/10.1002/aenm.202101780

169. Y.T. Liu, D.D. Han, L. Wang, G.R. Li, S. Liu et al., $NiCo_2O_4$ nanofibers as carbon-free sulfur immobilizer to fabricate sulfur-based composite with high volumetric capacity for lithium–sulfur battery. Adv. Energy Mater. **9**(11), 1803477 (2019). https://doi.org/10.1002/aenm.201803477

170. W. Hou, P. Feng, X. Guo, Z. Wang, Z. Bai et al., Catalytic mechanism of oxygen vacancies in perovskite oxides for lithium–sulfur batteries. Adv. Mater. **34**(26), 2202222 (2022). https://doi.org/10.1002/adma.202202222

171. S. Dai, C. Sun, Y. Zhang, L. Zeng, Y. Peng et al., Carbon microspheres built of La_2O_3 quantum dots-implanted nanorods: superb hosts with ultra-long Li_2S_n-catalysis durability. J. Colloid Interface Sci. **640**, 320–328 (2023). https://doi.org/10.1016/j.jcis.2023.02.127

172. N. Li, T. Meng, L. Ma, H. Zhang, J. Yao et al., Curtailing carbon usage with addition of functionalized $NiFe_2O_4$ quantum dots: toward more practical S cathodes for Li–S cells. Nano Micro Lett. **12**(1), 145 (2020). https://doi.org/10.1007/s40820-020-00484-4

173. C. Sun, J. Zhu, B. Liu, M. Xu, J. Jiang et al., High-tap-density sulfur cathodes made beyond 400 °C for lithium–sulfur cells with balanced gravimetric/volumetric energy densities. ACS Energy Lett. **8**(1), 772–779 (2022). https://doi.org/10.1021/acsenergylett.2c02313

174. J. Shen, X. Xu, J. Liu, Z. Liu, F. Li et al., Mechanistic understanding of metal phosphide host for sulfur cathode in high-energy-density lithium–sulfur batteries. ACS Nano **13**(8), 8986–8996 (2019). https://doi.org/10.1021/acsnano.9b02903

175. X. Gao, Y. Huang, X. Li, H. Gao, T. Li, $SnP_{0.94}$ nanodots confined carbon aerogel with porous hollow superstructures as an exceptional polysulfide electrocatalyst and "adsorption nest" to enable enhanced lithium–sulfur batteries. Chem. Eng. J. **420**, 129724 (2021). https://doi.org/10.1016/j.cej.2021.129724

176. L. Wang, M. Zhang, B. Zhang, B. Wang, J. Dou et al., A porous polycrystalline $NiCo_2P_x$ as a highly efficient host for sulfur cathodes in Li–S batteries. J. Mater. Chem. A **9**(40), 23149–23156 (2021). https://doi.org/10.1039/d1ta06249b

177. Y. Feng, L. Zu, S. Yang, L. Chen, K. Liao et al., Ultrahigh-content Co–P cluster as a dual-atom-site electrocatalyst for accelerating polysulfides conversion in Li–S batteries. Adv. Funct. Mater. (2022). https://doi.org/10.1002/adfm.202207579

178. C. Zhang, R. Du, J.J. Biendicho, M. Yi, K. Xiao et al., Tubular CoFeP@CN as a Mott-Schottky catalyst with multiple adsorption sites for robust lithium–sulfur batteries. Adv. Energy Mater. **11**(24), 2100432 (2021). https://doi.org/10.1002/aenm.202100432

179. Y. Dong, D. Cai, T. Li, S. Yang, X. Zhou et al., Sulfur reduction catalyst design inspired by elemental periodic expansion concept for lithium–sulfur batteries. ACS Nano **16**(4), 6414–6425 (2022). https://doi.org/10.1021/acsnano.2c00515

180. Y. Ren, B. Wang, H. Liu, H. Wu, H. Bian et al., CoP nanocages intercalated MXene nanosheets as a bifunctional

mediator for suppressing polysulfide shuttling and dendritic growth in lithium–sulfur batteries. Chem. Eng. J. **450**, 138046 (2022). https://doi.org/10.1016/j.cej.2022.138046

181. J. Sun, Y. Liu, L. Liu, S. He, Z. Du et al., Expediting sulfur reduction/evolution reactions with integrated electrocatalytic network: a comprehensive kinetic map. Nano Lett. **22**(9), 3728–3736 (2022). https://doi.org/10.1021/acs.nanolett.2c00642

182. B. Zhang, L. Wang, B. Wang, Y. Zhai, S. Zeng et al., Petroleum coke derived porous carbon/nicop with efficient reviving catalytic and adsorptive activity as sulfur host for high performance lithium–sulfur batteries. Nano Res. **15**(5), 4058–4067 (2022). https://doi.org/10.1007/s12274-021-3996-5

183. R. Sun, Y. Bai, M. Luo, M. Qu, Z. Wang et al., Enhancing polysulfide confinement and electrochemical kinetics by amorphous cobalt phosphide for highly efficient lithium–sulfur batteries. ACS Nano **15**(1), 739–750 (2021). https://doi.org/10.1021/acsnano.0c07038

184. Y. Yang, Y. Zhong, Q. Shi, Z. Wang, K. Sun et al., Electrocatalysis in lithium sulfur batteries under lean electrolyte conditions. Angew. Chem. Int. Ed. **57**(47), 15549–15552 (2018). https://doi.org/10.1002/anie.201808311

185. R. Sun, Y. Bai, Z. Bai, L. Peng, M. Luo et al., Phosphorus vacancies as effective polysulfide promoter for high-energy-density lithium–sulfur batteries. Adv. Energy Mater. **12**(12), 2102739 (2022). https://doi.org/10.1002/aenm.202102739

186. Y. Chen, W. Zhang, D. Zhou, H. Tian, D. Su et al., Co-Fe mixed metal phosphide nanocubes with highly interconnected-pore architecture as an efficient polysulfide mediator for lithium–sulfur batteries. ACS Nano **13**(4), 4731–4741 (2019). https://doi.org/10.1021/acsnano.9b01079

187. J. Li, W. Xie, S. Zhang, S.-M. Xu, M. Shao, Boosting the rate performance of Li–S batteries under high mass-loading of sulfur based on a hierarchical NCNT@Co-CoP nanowire integrated electrode. J. Mater. Chem. A **9**(18), 11151–11159 (2021). https://doi.org/10.1039/d1ta00959a

188. J. Zhou, X. Liu, L. Zhu, J. Zhou, Y. Guan et al., Deciphering the modulation essence of P bands in Co-based compounds on Li–S chemistry. Joule **2**(12), 2681–2693 (2018). https://doi.org/10.1016/j.joule.2018.08.010

189. Y. Mi, W. Liu, X. Li, J. Zhuang, H. Zhou et al., High-performance Li–S battery cathode with catalyst-like carbon nanotube-MoP promoting polysulfide redox. Nano Res. **10**(11), 3698–3705 (2017). https://doi.org/10.1007/s12274-017-1581-8

190. X. Huang, J. Tang, B. Luo, R. Knibbe, T. Lin et al., Sandwich-like ultrathin TiS$_2$ nanosheets confined within N, S codoped porous carbon as an effective polysulfide promoter in lithium–sulfur batteries. Adv. Energy Mater. **9**(32), 1901872 (2019). https://doi.org/10.1002/aenm.201901872

191. Z.-L. Xu, N. Onofrio, J. Wang, Boosting the anchoring and catalytic capability of MoS$_2$ for high-loading lithium sulfur batteries. J. Mater. Chem. A **8**(34), 17646–17656 (2020). https://doi.org/10.1039/d0ta05948j

192. C. Zhang, B. Fei, D. Yang, H. Zhan, J. Wang et al., Robust lithium–sulfur batteries enabled by highly conductive WSe$_2$-based superlattices with tunable interlayer space. Adv. Funct. Mater. **32**(24), 2201322 (2022). https://doi.org/10.1002/adfm.202201322

193. Y. Zhong, L. Yin, P. He, W. Liu, Z. Wu et al., Surface chemistry in cobalt phosphide-stabilized lithium–sulfur batteries. J. Am. Chem. Soc. **140**(4), 1455–1459 (2018). https://doi.org/10.1021/jacs.7b11434

194. H. Wang, D. Wei, J. Zheng, B. Zhang, M. Ling et al., Electrospinning MoS$_2$-decorated porous carbon nanofibers for high-performance lithium–sulfur batteries. ACS Appl. Energy Mater. **3**(12), 11893–11899 (2020). https://doi.org/10.1021/acsaem.0c02015

195. M. Wang, L. Fan, X. Sun, B. Guan, B. Jiang et al., Nitrogen-doped CoSe$_2$ as a bifunctional catalyst for high areal capacity and lean electrolyte of Li–S battery. ACS Energy Lett. **5**(9), 3041–3050 (2020). https://doi.org/10.1021/acsenergylett.0c01564

196. H. Yang, Regulation polysulfide conversion by flexible carbon cloth/molybdenum selenide to improve sulfur redox kinetics in lithium–sulfur battery. Int. J. Electrochem. Sci. (2020). https://doi.org/10.20964/2020.08.72

197. Y. Li, H. Wu, D. Wu, H. Wei, Y. Guo et al., High-density oxygen doping of conductive metal sulfides for better polysulfide trapping and Li$_2$S-S$_8$ redox kinetics in high areal capacity lithium–sulfur batteries. Adv. Sci. **9**(17), 2200840 (2022). https://doi.org/10.1002/Adv.s.202200840

198. M. Wang, Z. Sun, H. Ci, Z. Shi, L. Shen et al., Identifying the evolution of selenium-vacancy-modulated MoSe$_2$ precatalyst in lithium–sulfur chemistry. Angew. Chem. Int. Ed. **60**(46), 24558–24565 (2021). https://doi.org/10.1002/anie.202109291

199. Z. Ye, Y. Jiang, L. Li, F. Wu, R. Chen, Self-assembly of 0D–2D heterostructure electrocatalyst from MOF and MXene for boosted lithium polysulfide conversion reaction. Adv. Mater. **33**(33), e2101204 (2021). https://doi.org/10.1002/adma.202101204

200. B. Yu, A. Huang, K. Srinivas, X. Zhang, F. Ma et al., Outstanding catalytic effects of 1T'-MoTe$_2$ quantum dots@3D graphene in shuttle-free Li–S batteries. ACS Nano **15**, 13279–13288 (2021). https://doi.org/10.1021/acsnano.1c03011

201. L. Jiao, H. Jiang, Y. Lei, S. Wu, Q. Gao et al., "Dual mediator system" enables efficient and persistent regulation toward sulfur redox conversion in lithium–sulfur batteries. ACS Nano **16**, 14262–14273 (2022). https://doi.org/10.1021/acsnano.2c04402

202. C. Li, W. Ge, S. Qi, L. Zhu, R. Huang et al., Manipulating electrocatalytic polysulfide redox kinetics by 1d core–shell like composite for lithium–sulfur batteries. Adv. Energy Mater. **12**(16), 2103915 (2022). https://doi.org/10.1002/aenm.202103915

203. H. Li, R. Gao, B. Chen, C. Zhou, F. Shao et al., Vacancy-rich mosse with sulfiphilicity-lithiophilicity dual function for kinetics-enhanced and dendrite-free Li–S batteries. Nano Lett. **22**(12), 4999–5008 (2022). https://doi.org/10.1021/acs.nanolett.2c01779

204. H.-J. Li, K. Xi, W. Wang, S. Liu, G.-R. Li et al., Quantitatively regulating defects of 2D tungsten selenide to enhance catalytic ability for polysulfide conversion in a lithium sulfur battery. Energy Storage Mater. **45**, 1229–1237 (2022). https://doi.org/10.1016/j.ensm.2021.11.024

205. N. Wang, B. Chen, K. Qin, R. Zhang, Y. Tang et al., Octopus-inspired design of apical NiS_2 nanoparticles supported on hierarchical carbon composites as an efficient host for lithium sulfur batteries with high sulfur loading. ACS Appl. Mater. Interfaces **12**(15), 17528–17537 (2020). https://doi.org/10.1021/acsami.0c01640

206. H. Li, X. Wen, F. Shao, C. Zhou, Y. Zhang et al., Interface covalent bonding endowing high-sulfur-loading paper cathode with robustness for energy-dense, compact and foldable lithium–sulfur batteries. Chem. Eng. J. **412**, 128562 (2021). https://doi.org/10.1016/j.cej.2021.128562

207. H. Ci, J. Cai, H. Ma, Z. Shi, G. Cui et al., Defective VSe_2-graphene heterostructures enabling in situ electrocatalyst evolution for lithium–sulfur batteries. ACS Nano **14**(9), 11929–11938 (2020). https://doi.org/10.1021/acsnano.0c05030

208. Z. Ye, Y. Jiang, L. Li, F. Wu, R. Chen, A high-efficiency cose electrocatalyst with hierarchical porous polyhedron nanoarchitecture for accelerating polysulfides conversion in Li–S batteries. Adv. Mater. **32**(32), 2002168 (2020). https://doi.org/10.1002/adma.202002168

209. L. Sun, Y. Liu, J. Xie, L. Fan, J. Wu et al., Polar Co_9S_8 anchored on pyrrole-modified graphene with in situ growth of cnts as multifunctional self-supporting medium for efficient lithium–sulfur batteries. Chem. Eng. J. **451**, 138370 (2023). https://doi.org/10.1016/j.cej.2022.138370

210. Z. Cheng, Y. Chen, Y. Yang, L. Zhang, H. Pan et al., Metallic MoS_2 nanoflowers decorated graphene nanosheet catalytically boosts the volumetric capacity and cycle life of lithium–sulfur batteries. Adv. Energy Mater. **11**(12), 2003718 (2021). https://doi.org/10.1002/aenm.202003718

211. R. Xu, H. Tang, Y. Zhou, F. Wang, H. Wang et al., Enhanced catalysis of radical-to-polysulfide interconversion via increased sulfur vacancies in lithium–sulfur batteries. Chem. Sci. **13**(21), 6224–6232 (2022). https://doi.org/10.1039/d2sc01353c

212. Y. Xue, D. Luo, N. Yang, G. Ma, Z. Zhang et al., Engineering checkerboard-like heterostructured sulfur electrocatalyst towards high-performance lithium sulfur batteries. Chem. Eng. J. **440**, 135990 (2022). https://doi.org/10.1016/j.cej.2022.135990

213. T. Yan, J. Feng, P. Zeng, G. Zhao, L. Wang et al., Modulating e orbitals through ligand engineering to boost the electrocatalytic activity of nise for advanced lithium–sulfur batteries. J. Energy Chem. **74**, 317–323 (2022). https://doi.org/10.1016/j.jechem.2022.07.025

214. W. Sun, S. Liu, Y. Li, D. Wang, Q. Guo et al., Monodispersed FeS_2 electrocatalyst anchored to nitrogen-doped carbon host for lithium–sulfur batteries. Adv. Funct. Mater. **32**, 2205471 (2022). https://doi.org/10.1002/adfm.202205471

215. M. Li, D. Yang, J.J. Biendicho, X. Han, C. Zhang et al., Enhanced polysulfide conversion with highly conductive and electrocatalytic iodine-doped bismuth selenide nanosheets in lithium–sulfur batteries. Adv. Funct. Mater. **32**(26), 2200529 (2022). https://doi.org/10.1002/adfm.202200529

216. X.Y. Li, S. Feng, M. Zhao, C.X. Zhao, X. Chen et al., Surface gelation on disulfide electrocatalysts in lithium–sulfur batteries. Angew. Chem. Int. Ed. **61**(7), 202114671 (2022). https://doi.org/10.1002/anie.202114671

217. S. Chandrasekaran, L. Yao, L. Deng, C. Bowen, Y. Zhang et al., Recent advances in metal sulfides: from controlled fabrication to electrocatalytic, photocatalytic and photoelectrochemical water splitting and beyond. Chem. Soc. Rev. **48**(15), 4178–4280 (2019). https://doi.org/10.1039/c8cs00664d

218. S. Ogawa, T. Teranishi, Electrical reslstlvlty of narrow-band ferromagnet $Fe_{1-x}Co_xS_2$. Phys. Lett. A **42**, 147–148 (1972)

219. X. Zhang, Z. Lai, C. Tan, H. Zhang, Solution-processed two-dimensional MoS_2 nanosheets: preparation, hybridization, and applications. Angew. Chem. Int. Ed. **55**(31), 8816–8838 (2016). https://doi.org/10.1002/anie.201509933

220. G. Ye, Y. Gong, J. Lin, B. Li, Y. He et al., Defects engineered monolayer MoS_2 for improved hydrogen evolution reaction. Nano Lett. **16**(2), 1097–1103 (2016). https://doi.org/10.1021/acs.nanolett.5b04331

221. C. Tan, X. Cao, X.J. Wu, Q. He, J. Yang et al., Recent advances in ultrathin two-dimensional nanomaterials. Chem. Rev. **117**(9), 6225–6331 (2017). https://doi.org/10.1021/acs.chemrev.6b00558

222. X. Huang, Z. Zeng, H. Zhang, Metal dichalcogenide nanosheets: preparation, properties and applications. Chem. Soc. Rev. **42**(5), 1934–1946 (2013). https://doi.org/10.1039/c2cs35387c

223. M. Chhowalla, H.S. Shin, G. Eda, L.J. Li, K.P. Loh et al., The chemistry of two-dimensional layered transition metal dichalcogenide nanosheets. Nat. Chem. **5**(4), 263–275 (2013). https://doi.org/10.1038/nchem.1589

224. Q. Wu, Z. Yao, X. Zhou, J. Xu, F. Cao et al., Built-in catalysis in confined nanoreactors for high-loading Li–S batteries. ACS Nano **14**(3), 3365–3377 (2020). https://doi.org/10.1021/acsnano.9b09231

225. M. Wang, L. Fan, D. Tian, X. Wu, Y. Qiu et al., Rational design of hierarchical SnO_2/1T-MoS_2 nanoarray electrode for ultralong-life Li–S batteries. ACS Energy Lett. **3**(7), 1627–1633 (2018). https://doi.org/10.1021/acsenergylett.8b00856

226. H. Lin, L. Yang, X. Jiang, G. Li, T. Zhang et al., Electrocatalysis of polysulfide conversion by sulfur-deficient MoS_2 nanoflakes for lithium–sulfur batteries. Energy Environ. Sci. **10**(6), 1476–1486 (2017). https://doi.org/10.1039/c7ee01047h

227. Z.L. Xu, S. Lin, N. Onofrio, L. Zhou, F. Shi et al., Exceptional catalytic effects of black phosphorus quantum dots in shuttling-free lithium sulfur batteries. Nat. Commun. **9**(1), 4164 (2018). https://doi.org/10.1038/s41467-018-06629-9

228. W. Ge, L. Wang, C. Li, C. Wang, D. Wang et al., Conductive cobalt doped niobium nitride porous spheres as an efficient polysulfide convertor for advanced lithium–sulfur batteries.

J. Mater. Chem. A **8**(13), 6276–6282 (2020). https://doi.org/10.1039/d0ta00800a

229. F. Li, M. Zhang, W. Chen, X. Cai, H. Rao et al., Vanadium nitride quantum dots/holey graphene matrix boosting adsorption and conversion reaction kinetics for high-performance lithium–sulfur batteries. ACS Appl. Mater. Interfaces **13**(26), 30746–30755 (2021). https://doi.org/10.1021/acsami.1c08113

230. D. Xie, Y. Xu, Y. Wang, X. Pan, E. Hark et al., Poly(ionic liquid) nanovesicle-templated carbon nanocapsules functionalized with uniform iron nitride nanoparticles as catalytic sulfur host for Li–S batteries. ACS Nano **16**, 10554–10565 (2022). https://doi.org/10.1021/acsnano.2c01992

231. M. Zhao, H.J. Peng, Z.W. Zhang, B.Q. Li, X. Chen et al., Activating inert metallic compounds for high-rate lithium–sulfur batteries through in situ etching of extrinsic metal. Angew. Chem. Int. Ed. **58**(12), 3779–3783 (2019). https://doi.org/10.1002/anie.201812062

232. Z. Cui, C. Zu, W. Zhou, A. Manthiram, J.B. Goodenough, Mesoporous titanium nitride-enabled highly stable lithium–sulfur batteries. Adv. Mater. **28**(32), 6926–6931 (2016). https://doi.org/10.1002/adma.201601382

233. Z. Li, Q. He, X. Xu, Y. Zhao, X. Liu et al., A 3D nitrogen-doped graphene/TiN nanowires composite as a strong polysulfide anchor for lithium–sulfur batteries with enhanced rate performance and high areal capacity. Adv. Mater. **30**(45), 1804089 (2018). https://doi.org/10.1002/adma.201804089

234. H. Zhang, D. Tian, Z. Zhao, X. Liu, Y.-N. Hou et al., Cobalt nitride nanoparticles embedded in porous carbon nanosheet arrays propelling polysulfides conversion for highly stable lithium–sulfur batteries. Energy Storage Mater. **21**, 210–218 (2019). https://doi.org/10.1016/j.ensm.2018.12.005

235. M. Zhang, L. Wang, B. Wang, B. Zhang, X. Sun et al., Phosphorus-modified $Fe_4N@N$, P co-doped graphene as an efficient sulfur host for high-performance lithium–sulfur batteries. J. Mater. Chem. A **9**(10), 6538–6546 (2021). https://doi.org/10.1039/d0ta12361g

236. J. Qian, Y. Xing, Y. Yang, Y. Li, K. Yu et al., Enhanced electrochemical kinetics with highly dispersed conductive and electrocatalytic mediators for lithium–sulfur batteries. Adv. Mater. **33**(25), 2100810 (2021). https://doi.org/10.1002/adma.202100810

237. X. Li, Y. Zhang, S. Wang, Y. Liu, Y. Ding et al., Hierarchically porous C/Fe_3C membranes with fast ion-transporting channels and polysulfide-trapping networks for high-areal-capacity Li–S batteries. Nano Lett. **20**(1), 701–708 (2020). https://doi.org/10.1021/acs.nanolett.9b04551

238. S. Deng, X. Shi, Y. Zhao, C. Wang, J. Wu et al., Catalytic Mo_2C decorated N-doped honeycomb-like carbon network for high stable lithium–sulfur batteries. Chem. Eng. J. **433**, 133683 (2022). https://doi.org/10.1016/j.cej.2021.133683

239. S.-H. Moon, J.-H. Kim, J.-H. Shin, J.-S. Jang, S.-B. Kim et al., High absorption and fast polysulfides conversion of duel functional separator based on mesoporous-WC/rGO composite for lithium-sulfur batteries. J. Alloys Compd.

904, 164120 (2022). https://doi.org/10.1016/j.jallcom.2022.164120

240. W. Wu, X. Li, L. Liu, X. Zhu, Z. Guo et al., Uniform coverage of high-loading sulfur on cross-linked carbon nanofibers for high reaction kinetics in Li–S batteries with low electrolyte/sulfur ratio. J. Mater. Chem. A **10**(3), 1433–1441 (2022). https://doi.org/10.1039/d1ta09408d

241. P. Zeng, C. Yuan, J. An, X. Yang, C. Cheng et al., Achieving reversible precipitation-decomposition of reactive Li_2S towards high-areal-capacity lithium–sulfur batteries with a wide-temperature range. Energy Storage Mater. **44**, 425–432 (2022). https://doi.org/10.1016/j.ensm.2021.10.035

242. G. Liu, C. Yuan, P. Zeng, C. Cheng, T. Yan et al., Bidirectionally catalytic polysulfide conversion by high-conductive metal carbides for lithium–sulfur batteries. J. Energy Chem. **67**, 73–81 (2022). https://doi.org/10.1016/j.jechem.2021.09.035

243. B. Shen, Q. Liu, C. Ma, Y. Li, Z. Li et al., A facile synthesis of stable titanium carbide-decorated carbon nanofibers as electrocatalytic membrane for high-performance lithium–sulfur batteries. Ionics **28**(3), 1173–1182 (2022). https://doi.org/10.1007/s11581-021-04399-x

244. J. Zheng, C. Guan, H. Li, Y. Xie, S. Li et al., VC@NCNTs: bidirectional catalyst for fast charging lithium-sulfur batteries. Chem. Eng. J. **442**, 135940 (2022). https://doi.org/10.1016/j.cej.2022.135940

245. T. Wang, D. Luo, Y. Zhang, Z. Zhang, J. Wang et al., Hierarchically porous Ti_3C_2 MXene with tunable active edges and unsaturated coordination bonds for superior lithium–sulfur batteries. ACS Nano **15**(12), 19457–19467 (2021). https://doi.org/10.1021/acsnano.1c06213

246. S. Zhang, N. Zhong, X. Zhou, M. Zhang, X. Huang et al., Comprehensive design of the high-sulfur-loading Li–S battery based on mxene nanosheets. Nano Micro Lett. **12**(1), 112 (2020). https://doi.org/10.1007/s40820-020-00449-7

247. J. Xia, W. Chen, Y. Yang, X. Guan, T. Yang et al., In-situ growth of ultrathin sulfur microcrystal on MXene-based 3D matrice for flexible lithium–sulfur batteries. EcoMat **4**(3), e12183 (2022). https://doi.org/10.1002/eom2.12183

248. D. Guo, F. Ming, H. Su, Y. Wu, W. Wahyudi et al., Mxene based self-assembled cathode and antifouling separator for high-rate and dendrite-inhibited Li–S battery. Nano Energy **61**, 478–485 (2019). https://doi.org/10.1016/j.nanoen.2019.05.011

249. B. Qin, Y. Cai, X. Si, C. Li, J. Cao et al., Ultra-lightweight ion-sieving membranes for high-rate lithium sulfur batteries. Chem. Eng. J. **430**, 132698 (2022). https://doi.org/10.1016/j.cej.2021.132698

250. L. Zheng, C.E. Ren, M. Zhaoa, J. Yanga, J.M. Giammarco et al., Flexible and conductive mxene films and nanocomposites with high capacitance. Proc. Natl. Acad. Sci. **111**(47), 16676–16681 (2014). https://doi.org/10.1073/pnas.1414215111

251. Y. He, Y. Zhao, Y. Zhang, Z. He, G. Liu et al., Building flexibly porous conductive skeleton inlaid with surface oxygen-dominated mxene as an amphiphilic nanoreactor

for stable Li–S pouch batteries. Energy Storage Mater. **47**, 434–444 (2022). https://doi.org/10.1016/j.ensm.2022.02.006

252. D. Xiong, X. Li, Z. Bai, S. Lu, Recent advances in layered Ti₃C₂Tₓ MXene for electrochemical energy storage. Small **14**(17), 1703419 (2018). https://doi.org/10.1002/smll.201703419

253. J. Pang, R.G. Mendes, A. Bachmatiuk, L. Zhao, H.Q. Ta et al., Applications of 2D MXenes in energy conversion and storage systems. Chem. Soc. Rev. **48**(1), 72–133 (2019). https://doi.org/10.1039/c8cs00324f

254. M. Okubo, A. Sugahara, S. Kajiyama, A. Yamada, Mxene as a charge storage host. Acc. Chem. Res. **51**(3), 591–599 (2018). https://doi.org/10.1021/acs.accounts.7b00481

255. M. Naguib, M. Kurtoglu, V. Presser, J. Lu, J. Niu et al., Two-dimensional nanocrystals produced by exfoliation of Ti₃AlC₂. Adv. Mater. **23**(37), 4248–4253 (2011). https://doi.org/10.1002/adma.201102306

256. N.K. Chaudhari, H. Jin, B. Kim, D. San Baek, S.H. Joo et al., Mxene: an emerging two-dimensional material for future energy conversion and storage applications. J. Mater. Chem. A **5**(47), 24564–24579 (2017). https://doi.org/10.1039/c7ta09094c

257. S. Li, J. Lin, Y. Ding, P. Xu, X. Guo et al., Defects engineering of lightweight metal-organic frameworks-based electrocatalytic membrane for high-loading lithium–sulfur batteries. ACS Nano **15**, 13803–13813 (2021). https://doi.org/10.1021/acsnano.1c05585

258. Q. Zeng, X. Li, W. Gong, S. Guo, Y. Ouyang et al., Copolymerization of sulfur chains with vinyl functionalized metal-organic framework for accelerating redox kinetics in lithium–sulfur batteries. Adv. Energy Mater. **12**(21), 2104074 (2022). https://doi.org/10.1002/aenm.202104074

259. Y. Wang, Z. Deng, J. Huang, H. Li, Z. Li et al., 2D Zr-Fc metal-organic frameworks with highly efficient anchoring and catalytic conversion ability towards polysulfides for advanced li–s battery. Energy Storage Mater. **36**, 466–477 (2021). https://doi.org/10.1016/j.ensm.2021.01.025

260. H.C. Zhou, J.R. Long, O.M. Yaghi, Introduction to metal-organic frameworks. Chem. Rev. **112**(2), 673–674 (2012). https://doi.org/10.1021/cr300014x

261. H.C. Zhou, S. Kitagawa, Metal-organic frameworks (MOFs). Chem. Soc. Rev. **43**(16), 5415–5418 (2014). https://doi.org/10.1039/c4cs90059f

262. S. Wang, X. Wang, Imidazolium ionic liquids, imidazolylidene heterocyclic carbenes, and zeolitic imidazolate frameworks for CO_2 capture and photochemical reduction. Angew. Chem. Int. Ed. **55**(7), 2308–2320 (2016). https://doi.org/10.1002/anie.201507145

263. C.A. Trickett, A. Helal, B.A. Al-Maythalony, Z.H. Yamani, K.E. Cordova et al., The chemistry of metal-organic frameworks for CO_2 capture, regeneration and conversion. Nat. Rev. Mater. **2**(8), 17045 (2017). https://doi.org/10.1038/natrevmats.2017.45

264. A. Schoedel, Z. Ji, O.M. Yaghi, The role of metal-organic frameworks in a carbon-neutral energy cycle. Nat. Energy **1**(4), 16034 (2016). https://doi.org/10.1038/nenergy.2016.34

265. J.R. Long, O.M. Yaghi, The pervasive chemistry of metal-organic frameworks. Chem. Soc. Rev. **38**(5), 1213–1214 (2009). https://doi.org/10.1039/b903811f

266. M. Ding, R.W. Flaig, H.L. Jiang, O.M. Yaghi, Carbon capture and conversion using metal-organic frameworks and MOF-based materials. Chem. Soc. Rev. **48**(10), 2783–2828 (2019). https://doi.org/10.1039/c8cs00829a

267. W. Lu, Z. Wei, Z. Gu, T. Liu, J. Park et al., Tuning the structure and function of metal-organic frameworks via linker design. Chem. Soc. Rev. **43**, 5561 (2014). https://doi.org/10.1039/C4CS00003J

268. M. Eddaoudi, D.B. Moler, H. Li, B. Chen, T.M. Reineke, Modular chemistry: secondary building units as a basis for the design of highly porous and robust metal-organic carboxylate frameworks. Acc. Chem. Res. **34**, 318–330 (2001). https://doi.org/10.1021/ar000034b

269. J.S. Seo, D. Whang, H. Lee, S.I. Jun, J. Oh, Y.J. Jeon, K. Kim, A homochiral metal-organic porous material for enantioselective separation and catalysis. Nature **404**, 982–986 (2000). https://doi.org/10.1038/35010088

270. D. Luo, C. Li, Y. Zhang, Q. Ma, C. Ma et al., Design of quasi-MOF nanospheres as a dynamic electrocatalyst toward accelerated sulfur reduction reaction for high-performance lithium–sulfur batteries. Adv. Mater. **34**(2), 2105541 (2022). https://doi.org/10.1002/adma.202105541

271. M. Rana, H.A. Al-Fayaad, B. Luo, T. Lin, L. Ran et al., Oriented nanoporous MOFs to mitigate polysulfides migration in lithium-sulfur batteries. Nano Energy **75**, 105009 (2020). https://doi.org/10.1016/j.nanoen.2020.105009

272. S. Wang, F. Huang, Z. Zhang, W. Cai, Y. Jie et al., Conductive metal-organic frameworks promoting polysulfides transformation in lithium–sulfur batteries. J. Energy Chem. **63**, 336–343 (2021). https://doi.org/10.1016/j.jechem.2021.08.037

273. X. Wang, J. Sun, T. Li, Z. Song, D. Wu et al., Folic acid self-assembly synthesis of ultrathin N-doped carbon nanosheets with single-atom metal catalysts. Energy Storage Mater. **36**, 409–416 (2021). https://doi.org/10.1016/j.ensm.2021.01.024

274. R. Wang, R. Wu, X. Yan, D. Liu, P. Guo et al., Implanting single zn atoms coupled with metallic Co nanoparticles into porous carbon nanosheets grafted with carbon nanotubes for high-performance lithium–sulfur batteries. Adv. Funct. Mater. **32**(20), 2200424 (2022). https://doi.org/10.1002/adfm.202200424

275. R. Xiao, T. Yu, S. Yang, K. Chen, Z. Li et al., Electronic structure adjustment of lithium sulfide by a single-atom copper catalyst toward high-rate lithium–sulfur batteries. Energy Storage Mater. **51**, 890–899 (2022). https://doi.org/10.1016/j.ensm.2022.07.024

276. G. Liu, W. Wang, P. Zeng, C. Yuan, L. Wang et al., Strengthened d-p orbital hybridization through asymmetric coordination engineering of single-atom catalysts for durable

lithium–sulfur batteries. Nano Lett. **22**(15), 6366–6374 (2022). https://doi.org/10.1021/acs.nanolett.2c02183

277. Y. Liu, Z. Wei, B. Zhong, H. Wang, L. Xia et al., O-, N-coordinated single mn atoms accelerating polysulfides transformation in lithium–sulfur batteries. Energy Storage Mater. **35**, 12–18 (2021). https://doi.org/10.1016/j.ensm.2020.11.011

278. B. Wang, L. Wang, B. Zhang, S. Zeng, F. Tian et al., Niobium diboride nanoparticles accelerating polysulfide conversion and directing Li$_2$S nucleation enabled high areal capacity lithium–sulfur batteries. ACS Nano **16**(3), 4947–4960 (2022). https://doi.org/10.1021/acsnano.2c01179

279. B. Wang, L. Wang, B. Zhang, Z. Kong, S. Zeng et al., Ultrafine zirconium boride nanoparticles constructed bidirectional catalyst for ultrafast and long-lived lithium–sulfur batteries. Energy Storage Mater. **45**, 130–141 (2022). https://doi.org/10.1016/j.ensm.2021.11.039

280. Q. Pang, C.Y. Kwok, D. Kundu, X. Liang, L.F. Nazar, Lightweight metallic MgB$_2$ mediates polysulfide redox and promises high-energy-density lithium–sulfur batteries. Joule **3**(1), 136–148 (2019). https://doi.org/10.1016/j.Joule2018.09.024

281. X. Sun, D. Tian, X. Song, B. Jiang, C. Zhao et al., In situ conversion to construct fast ion transport and high catalytic cathode for high-sulfur loading with lean electrolyte lithium–sulfur battery. Nano Energy **95**, 106979 (2022). https://doi.org/10.1016/j.nanoen.2022.106979

282. L. Luo, S.-H. Chung, C.-H. Chang, A. Manthiram, A nickel-foam@carbon-shell with a pie-like architecture as an efficient polysulfide trap for high-energy Li–S batteries. J. Mater. Chem. A **5**(29), 15002–15007 (2017). https://doi.org/10.1039/c7ta05277d

283. C. Lu, Y. Chen, Y. Yang, X. Chen, Single-atom catalytic materials for lean-electrolyte ultrastable lithium–sulfur batteries. Nano Lett. **20**(7), 5522–5530 (2020). https://doi.org/10.1021/acs.nanolett.0c02167

284. Y. Zhang, J. Liu, J. Wang, Y. Zhao, D. Luo et al., Engineering oversaturated Fe-N$_5$ multifunctional catalytic sites for durable lithium–sulfur batteries. Angew. Chem. Int. Ed. **60**(51), 26622–26629 (2021). https://doi.org/10.1002/anie.202108882

285. X. Fan, S. Chen, W. Gong, X. Meng, Y. Jia et al., A conjugated porous polymer complexed with a single-atom cobalt catalyst as an electrocatalytic sulfur host for enhancing cathode reaction kinetics. Energy Storage Mater. **41**, 14–23 (2021). https://doi.org/10.1016/j.ensm.2021.05.043

286. T. Huang, Y. Sun, J. Wu, Z. Shi, Y. Ding et al., Altering local chemistry of single-atom coordination boosts bidirectional polysulfide conversion of Li–S batteries. Adv. Funct. Mater. **32**, 2203902 (2022). https://doi.org/10.1002/adfm.202203902

287. Z. Han, S. Zhao, J. Xiao, X. Zhong, J. Sheng et al., Engineering d-p orbital hybridization in single-atom metal-embedded three-dimensional electrodes for Li–S batteries. Adv. Mater. **33**(44), 2105947 (2021). https://doi.org/10.1002/adma.202105947

288. J. He, A. Bhargav, A. Manthiram, Molybdenum boride as an efficient catalyst for polysulfide redox to enable high-energy-density lithium-sulfur batteries. Adv. Mater. **32**(40), 2004741 (2020). https://doi.org/10.1002/adma.202004741

289. T. Wu, T. Yang, J. Zhang, X. Zheng, K. Liu et al., CoB and BN composites enabling integrated adsorption/catalysis to polysulfides for inhibiting shuttle-effect in Li–S batteries. J. Energy Chem. **59**, 220–228 (2021). https://doi.org/10.1016/j.jechem.2020.11.015

290. T. Feng, T. Zhao, N. Zhang, Y. Duan, L. Li et al., 2D amorphous Mo-doped CoB for bidirectional sulfur catalysis in lithium sulfur batteries. Adv. Funct. Mater. **32**(30), 2202766 (2022). https://doi.org/10.1002/adfm.202202766

291. B. Guan, Y. Zhang, L. Fan, X. Wu, M. Wang et al., Blocking polysulfide with Co$_2$B@CNT via "synergetic adsorptive effect" toward ultrahigh-rate capability and robust lithium-sulfur battery. ACS Nano **13**(6), 6742–6750 (2019). https://doi.org/10.1021/acsnano.9b01329

292. C. Li, X. Liu, L. Zhu, R. Huang, M. Zhao et al., Conductive and polar titanium boride as a sulfur host for advanced lithium–sulfur batteries. Chem. Mater. **30**(20), 6969–6977 (2018). https://doi.org/10.1021/acs.chemmater.8b01352